RUHR-UNIVERSITÄT BOCHUM

RUB

STM Based Studies of a System of Adsorbed Xe and DAF on Ag(100)

Masterarbeit

im
Studiengang
Master of Science
im Fach Chemie

an der Fakultät für Chemie und Biochemie
der Ruhr-Universität Bochum

von
Inga Christina Langguth

Bochum, August 2019

Abstract

In this work a sub-monolayer of Xe and the carbene-precursor molecule 9-diazofluorene (DAF) adsorbed on Ag(100) are investigated by low-temperature scanning tunneling microscopy (STM). The above mentioned adsorbates are investigated separately and in their contact region after consecutive coadsorption. In this work, we consider DAF on a Xe buffer on a metal surface to decouple the DAF from the metal substrate in order to allow undisturbed imaging of DAF. This interaction between Xe and DAF is similar to the conditions during matrix isolation experiments and, hence, allows insight into those experiments. For the first time, Xe(111) deposition on Ag(100) is reported and its adsorption structure is identified as hexagonal and incommensurate. Xe alignment to the substrate is evident and the surface lattice parameter is found to be stretched by 7% compared to bulk Xe. The adsorption structure of the DAF molecules is compared to previous studies by K. Lucht about DAF on Ag(111). In contrast to Ag(111), DAF monomer formation aligned to the closed packed rows of the Ag(100) is reported, which is attributed to the higher corrugation and geometry of the Ag-substrate. The adsorption sites as well as the tip induced cleavage product of DAF on Ag(100) are identified.

The rotational orientation of Xe islands after consecutive coadsorption of DAF is revealed to be dominated by the confinement of the stronger kinetically hindered DAF. It is concluded that Xe has a larger temperature window of mobility at cold temperatures than DAF, which is a major limitation of the potential applicability of Xe layer for DAF decoupling. Nevertheless, evidence for the successful adsorption of DAF on a Xe layer is presented and the resulting experimental outlooks are discussed along with difficulties in the handling of STM-measurements on a Xe based system.

Contents

1 Introduction

1.1 Motivation: Enhanced Carbene Studies

Carbenes are carbon compounds which have an electron sextet and thus constitute an electron deficient compound with two non-bonding electrons on the carbon atom [1]. Such carbon compounds turn out to be extremely unstable and highly reactive. This outstanding reactivity is the reason for which carbenes have become a central focus point of chemical research since the 1980s. These compounds – previously merely known as extremely short-lived intermediate species – revealed a potential usage as high-turnover catalysts in organic synthesis when being stabilized and functionalized [2, 3]. It is, hence, of utmost interest to study and understand the electronic properties of carbenes, in order to utilize them in targeted applications such as organic synthesis and catalysis.

For an unbiased insight to the electronic structure of molecules, it is important to note that different examination methods have different requirements on the chemical environments of the sample. The resulting difference in interaction with the studied compound can be a decisive factor influencing the experimental course.

A well-accessible example of an in-situ precursor for carbene generation is 9-Diazofluoren (DAF), since the carbene-species fluorenylidene can be generated straightforwardly under laser radiation [4]. STM-studies of DAF reveal fundamentally different reaction products after analogous laser induced bond cleavage than IR studies within an argon matrix [4, 5] or compared to reactions carried out in solution [6, 7]. For the metal adsorbed species, no typical carbene reactivity is observed [5].

Differences in the intermolecular distance between the precursor molecules, compared to theoretical calculations, are already observed on the metal surface before the generation of the carbenes. Thus, a significant influence of the metal surface on the initial situation and thus also on the course of the reaction becomes apparent.

The interaction between the carbene-precursor and the substrate used in the STM measurement has a dominating influence on the molecular spacing as this is directed by energetically favored adsorption sites. The particular requirements of different kind of studies constitute different experimental conditions. This condition may cause differences in the subsequent reaction pathways. Different initial conditions such as different absorption structures may influence the behavior of the precursor already even before carbene generation.

Nevertheless, the adsorption on a solid and conductive (typically metallic) substrate in STM measurements is an inherent condition required by the experimental technique ([8–10]; see. *Sec.* 2.1). Because STM studies of organic molecules require adsorption on a metal substrate, the electronic structure of the molecules is significantly disturbed by the interaction with the substrate electrons. Still, accessing locally resolved data points, as feasible through STM, provides spatial information that cannot be obtained by any spectroscopic method, which makes STM a highly favorable analysis technique. In order to explore the characteristic electronic properties of a single, unperturbed molecule by STM, it is necessary to electronically decouple the molecule from the carrier substrate to lower the adsorbate-substrate-interaction. This may pose a major improvement to the investigation of carbenes, as STM is particularly suited to study individual molecules with local probing of a system's density of states. Creating and evaluating a system of reduced adsorbate interaction is aimed for in the following study.

1.2 Rare Gas Layers: Objectives in Surface Decoupling and Comparative Studies

STM is a very favorable tool for investigating electronic structures on atomic/molecular length scales since it is capable to locally probe a system's density of states [10]. Probing molecular orbitals is of key interest for determining and understanding carbene characteristics.

A basic and often used concept for lowering interaction with the required metal substrate is the formation of an ultra-thin non-conducting film in between the metal surface and the adsorbate molecules which yet enables the tunneling effect to occur [11]. This strategy has already revealed the magnificent capability of mapping actual molecular orbitals in the absence of the substrate influence [11–13]. During the first decade of this century, many experiments have been performed evaluating the substrate decoupling by ultra-thin salt layers [14].

Since carbene species are usually stabilized under rare gas matrices [15,16], it seems reasonable to apply rare gas for insulating layers. Equally important, ideally, the chemical environments thus produced are comparable to the conditions in matrix isolation spectroscopy. Buffer layers of Xe on metal substrates have proven to be applicable for surface decoupled metal nano particle growth [17]. It is not known presently whether DAF can be stabilized on top of a Xe layer in an equal manner. A preferential penetration through the layer to the metal surface is equally conceivable. The latter observation would also lead to a highly interesting system, allowing comparative studies to matrix conditions.

X-ray photoelectron spectroscopy studies reveal differing yields of the laser induced cleavage products N_2 and CO of tetrachloroquinonediazide, also a diazo-based carbene precursor, in the two cases of adsorption on Cu(111) and on Xe-multilayer($\approx$ 900 Langmuir) adsorbed on Cu(111). Beyond the catalytic substrate effect of Cu, one possible role of restricted mobility of the carbene within the matrix cage is discussed in [15].

This provides access to two highly interesting points of study in relation to the present system:

- Evaluating the extent to which a carbene species can be mapped in a decoupled manner by STM.
- An analysis of possible influences between the noble gas and the molecule (electrostatic as well as motion limiting factors), comparable to the conditions during matrix experiments.

Although these matters could not be fully illuminated within this work, we show promising evidence that this may be possible using the preparation method described in *Sec.* 2.4.2, 2.4.3 for future experiments.

In this work, a Xe-layer was successfully deposited on an Ag(100)-surface and investigated by STM before and after coadsorption of DAF: evidence is found that DAF-molecules can be deposited on this Xe-layer.

2 Methodology

2.1 Applied Techniques

All measurements of these studies are performed by *Scanning Tunneling Microscopy* (STM).

STM is a scanning probe technique for imaging the electron density of conductive surfaces on an atomic/molecular length scale in real space. It is based on the quantum mechanical tunneling effect between a conducting probe (ideally a tip with a one atom apex) and a conductive sample. A specific tunneling bias V_T is applied between tip and sample. The resulting tunneling current I_T is exponentially dependent on the length of the tunneling barrier d, i.e. the gap between sample and tip, and is calculated according to *Eq.* 1:

$$I_T = k_1 \cdot U_T \cdot e^{-k_2 \cdot \sqrt{\Phi} \cdot d} \tag{1}$$

where k_1 and k_2 are constants and Φ is the average work function of the metals.

In constant current mode, such as applied in these experiments, the current is kept at a constant set-point via a feedback loop that adjusts the tip's height to the required value to maintain the corresponding set-current during the scan. A spatially resolved topographic map of local electron density can hence be generated from the control signal of the feedback loop, when the sample is scanned by the tip in a scanning fashion [8–10].

2.2 Examined Materials

2.2.1 Ag(100)

The substrate of all present experiments is an Ag(100) single crystal supplied by MaTecK.

A Ag crystal is composed of face-centered cubic unit (fcc) cells with a lattice constant a of 409 pm [18]. Accordingly, the spacing distance of adjacent surface atoms d_{Ag} on the (100)-plane is $d_{\mathrm{Ag}} = 289\,\mathrm{pm}$.

The unit cell with designation of its basis vectors a_1, a_2, a_3 is shown in *Fig.* 1a). The (100) plane is highlighted in green. The atomic distances a and d_{Ag} are indicated in the top view image of this plane *Fig.* 1b). The resulting quadratic surface pattern is extended in *Fig.* 1c). The primitive unit cell of the fcc(100) surface, spanned by the primitive unit vectors $[1\,1\,0]$ and $[1\,\bar{1}\,0]$, is indicated in light green.

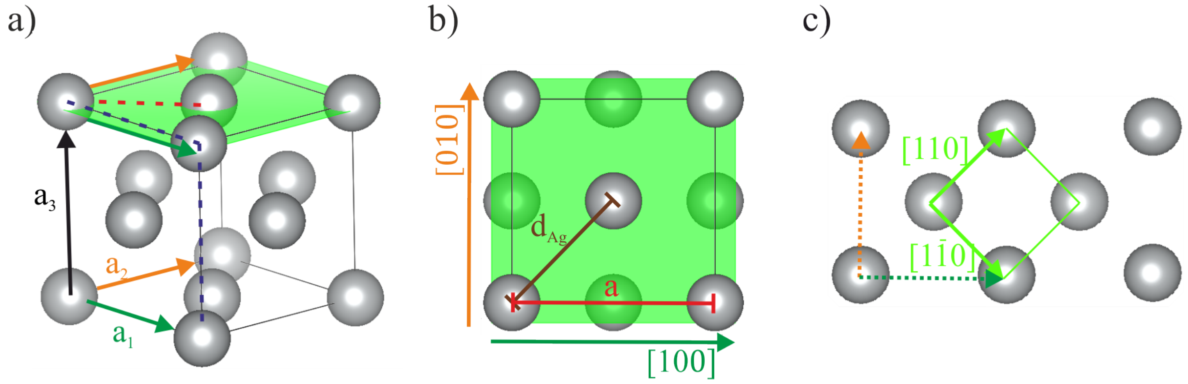

Figure 1: Ag unit cell, Ag atoms in gray, (100) plane highlighted in green; a) 3D view, basis vectors: a_1, a_2, a_3; b) Top view on (100) surface with bulk lattice parameter a, surface lattice parameter d_{Ag}; c) fcc(100) primitive unit cell spanned by the primitive unit vectors in light green

This work aims to investigate the examined molecules with as little influence of substrate surface as possible. Therefore, an Ag-substrate is used, similar to the studies by K. Lucht [5]. Ag is characterized by a rather weak interaction with adsorbates. Due to the absence of surface reconstructions Ag(100) offers a relatively low corrugated surface of a small surface unit cell. Accordingly, silver offers a low and homogeneous surface reactivity, which is making it more suitable for these studies than the even more noble but reconstructed gold.

The substrate has the advantageous property of promoting physisorption of the molecules instead of chemisorption. Due to the absence of surface reconstructions, Ag offers the best conditions of all available inert metal species for a comprehensible overview in the complex situation of the coadsorbance of multiple species.

In comparison to Ag(111), Ag(100) has a slightly higher corrugation. However, this offers a comparison of the adsorption characteristics between DAF on Ag(111), investigated before, and Ag(100). This comparison provides insight to the remaining interactions of the two different investigated systems.

Different lattice symmetries of the metal substrate and the ad-layer may furthermore facilitate a local distinction between Xe-covered and Xe-free areas. A different orientation may be expected for adsorbates on the layer and on bare metal areas. The conceivable enhanced distinctness of molecules adsorbed on quadratic and hexagonal substrate regions may provide a convenient advantage over the Ag(111) based system.

2.2.2 Xe(111)

The Xe film, investigated in here, is grown on Ag(100) from gas phase condensation of Xe (Westfalengas, purity: 4.0). At low pressures, pure condensed phase Xe is composed of face-centered cubic unit cells [19]. The temperature dependent lattice parameter b is found to be 620 pm at 75 K [20], which is the Xe deposition temperature applied here. Xe typically crystallizes on metal surfaces in a hexagonal close packed (hcp) fashion. For the case of a monolayer the hcp plane equals the fcc(111) plane of known bulk lattice parameter. On the fcc(111) surface the spacing distance of adjacent Xe atoms d_{Xe} is $b/\sqrt{2} = 438\,\mathrm{pm}$ [21] [22]. The corresponding step height between two planes is $b/\sqrt{3} = 356\,\mathrm{pm}$. The unit cell with designation of its basis vectors and the lattice parameter b is shown in *Fig.* 2a). The (111)-plane is highlighted in green in the top view image *Fig.* 2b) and the atomic distance d_{Xe} is indicated in blue. The resulting hexagonal surface pattern is extended in *Fig.* 2c).

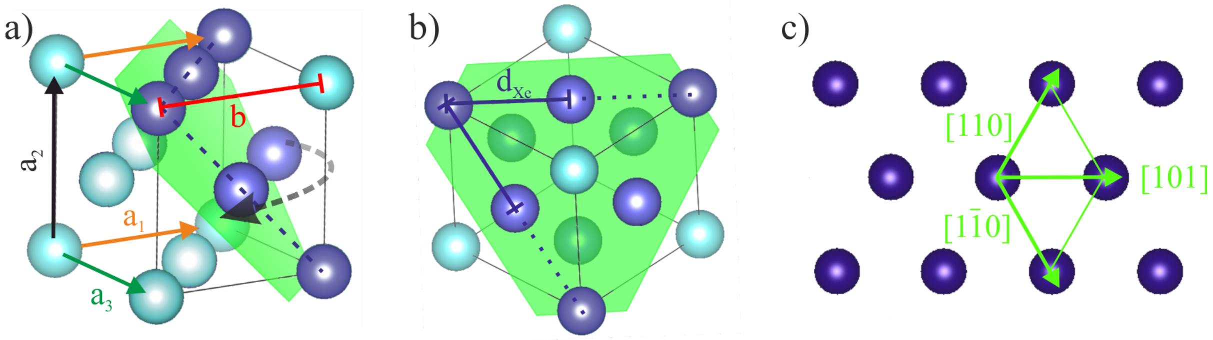

Figure 2: Xe unit cell, (111) plane highlighted in green, Xe atoms in (111) plane highlighted in dark blue, other Xe atoms in light blue; a) 3D view, lattice parameter b, basis vectors: a_1, a_2, a_3; b) Top view on (111) surface (green plane in a) turned around the dotted arrow), next neighbor Xe distance d_{Xe}; c) Hexagonal unit cell with closed packed directions in green

The primitive unit cell, as framed in light green, shows a rhombus shape. The closed packed directions are indicated by the three green arrows. All further references to crystal directions on the Xe surface will be based on the designations introduced in here.

Due to the high lattice mismatch between metal and rare gas lattice spacings, the superstructure of rare gases is known to have geometries that differ from the condensed phase case. The lattice constants are often found larger compared to the bulk and largely depending on the external conditions. In the comparable case of Xe on Ag(111), Chesters et al. [21] characterized the Xe monolayer as incommensurate triangular lattice, which is aligned to the substrate. The lattice parameter is found to be increased by 3% compared to the bulk. The Xe-Xe distance shows decrease with increasing lateral stress as a function of coverage and pressure [23], [22].

The versatility of rare gas superstructures have been intensely studied at the end of the 20th century and several different symmetries have been observed on various substrates. Commensurate or higher-order commensurate structures are found as well as incommen-

surate hcp structures with surface alignment [24] [23]. As an effect of mismatching lattice symmetries to metal substrates, complex rare gas superstructures such as c(12×2) Xe on Cu(110) were discovered [25].
On Pd, Cu and Ag substrates the Xe superstructure is found to be hcp, hcp ($\sqrt{3}\times\sqrt{3}\,\mathrm{R}30°$) or centered rectangular. The superstructure of Xe on Ag(100) is not yet known. Since the quadratic Ag(100) lattice does not allow a commensurate superstructure with the expected hexagonal structure, Xe on Ag(100) might allow investigations of incommensurable overlaps with the substrate. These overlaps may favor or hinder surface decoupling due to possible complex Moiré patterns of the surface potential.

2.2.3 9-Diazofluoren

The organic molecule 9-diazofluorene (DAF) investigated in here is a carbene precursor consisting of a fluorene skeleton with a diazo group at the C9 site, as seen in *Fig.* 3a). It is known to be capable of forming the carbene species fluorenylidene under irreversible photolytic N_2 elimination when being irradiated with a UV laser at a wavelength $\lambda = 365\,\mathrm{nm}$ [4, 5].
Previous STM studies show an absence of typical carbene reactivity, once DAF is irradiated in the adsorbed case on Ag(111) [5]. A new species, assigned to a surface bound carbene species is reported. No significant amount of the chemically linked dimer, 9,9'-bifluorene, is found, contrary to experiments in matrices or in solution [6, 7]. Likewise, no reaction with water to the alcohol, such as observed in matrix conditions [4], is seen. The characteristic behavior of the surface bound carbene thus differs significantly from the non-adsorbed case. A targeted reaction can neither be achieved by illumination nor by manipulation with the STM tip.
The DAF-molecule has shown to form dimers in favor of hydrogen bond (H-bond) formation. However, the determined H-bond length varies through the adsorption on Ag from the theoretically calculated one. Contrary to DFT based evaluations for the gas phase case of $(304 \pm 3)\,\mathrm{pm}$, H-bond length is determined to be $(270 \pm 10)\,\mathrm{pm}$ [5]. Thus, it becomes apparent that the interaction between the carbene-precursor and the substrate used in the STM measurement has a dictating influence on the molecular spacing, directed by energetically favored adsorption sites.
Fig. 3a) shows a representation of DAF in the DFT-optimizd ball-rod model. Accordingly, the regions of highest electron density are the aromatic phenyl rings as well as the electro negative diazo-group. The given diameters trough the long molecule axis from C to C and H to H of 0.69 nm and 0.91 nm are used later on as a characteristic molecule property to identify species seen in the STM in comparison. STM-images of the uncleaved and cleaved species, in both cases as dimer alignment, deposited at $(85 \pm 3)\,\mathrm{K}$ on Ag(111) are

shown in *Fig.* 3b) and c) according to [5] for comparison.

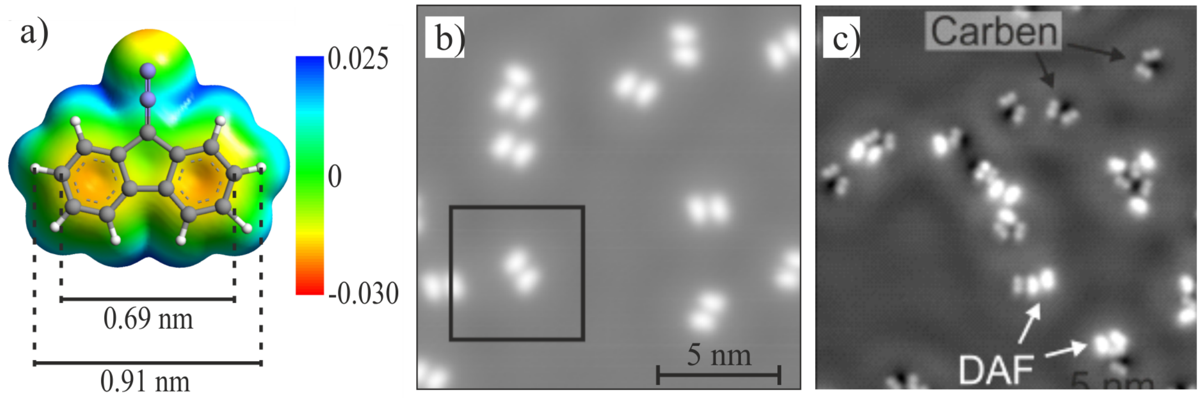

Figure 3: Summarized key characteristics of DAF: a) Ball-rod model and DFT-optimized ESP map of gas-phase DAF with intra-molecular spacings and charge density in e/B^3 according to the color scale; b) DAF Dimers after deposition at 85 K on Ag(111), dimer marked by box (double oval protrusion); c) Surface-bound carbene species after laser induced bond cleavage ($\lambda = 365\,\mathrm{nm}$) of DAF species presented in (b), seen as depression; tunneling parameters for (b) and (c): $I_\mathrm{t} = 8\,\mathrm{pA}$, $V_\mathrm{t} = 100\,\mathrm{mV}$ for both images, according to and with friendly permission of [5]

In here, DAF is adsorbed at different deposition temperatures ((45 ± 3) K, (53 ± 3) K, (63 ± 3) K) on Ag(100) after a deposition of a sub-monolayer Xe film. The temperature is chosen to be 30 K lower compared to the previous study in order to avoid Xe-evaporation and to restrict the Xe mobility. An avoidance of DAF-penetration is sought by that approach.

DAF is investigated with a special focus on interspecies interaction. It is characterized using the DFT-calculated molecular models by the Sander group [5] as shown in *Fig.* 3a) and compared to the studies on Ag(111). The DAF was synthesized and purified by Iris Trosien [4] (Chair of Organic Chemistry II, Prof. Wolfram Sander, Ruhr University Bochum).

2.3 Experimental Setup

All measurements are performed with a low temperature STM (LT-STM) by CreaTec Fischer & Co. GmbH, designed according to the technical specification of the research group *PC-I, RUB*. All preparations are carried out in the associated UHV-system.

This set-up is sketched according to the previous outline by K. Lucht [26] in *Fig.* 4.

The four main compartments of the apparatus as well as the specific, non-routine equipment for the described experimental procedure are highlighted by color and bold font.

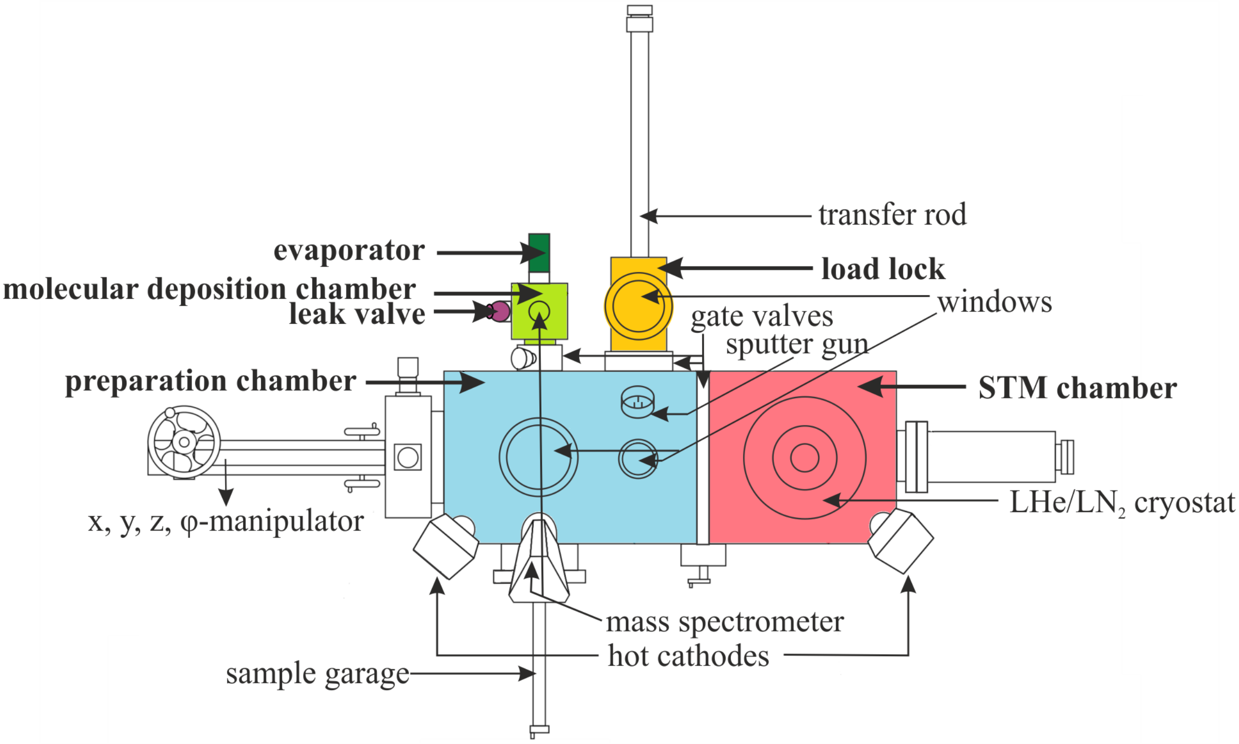

Figure 4: Top view scheme of the UHV system with labeling of the most important components: *Preparation chamber* (blue), *Load lock* (orange), *Molecular deposition chamber* (light green), *STM/Measurement chamber* (red), *Leak valve* for Xe inlet (purple), *Evaporator* for DAF deposition (dark green); according to & with kind permission of [26]

The apparatus consists of four chambers which are separated by gate valves. Each chamber is assigned to a particular task in the experimental course. This avoids contaminations in order to reach the best possible vacuum conditions for all steps. A sample is introduced to the UHV-system via the *Load Lock* chamber. It is afterwards cleaned and modified inside the *Preparation Chamber* (see *Sec.* 2.3.2). Designated adsorbate molecules or atoms are introduced to the UHV-system via the *Molecular Deposition Chamber* (see *Sec.* 2.3.3). The STM itself is located inside the *STM Chamber* where the measurements are performed.

2.3.1 STM Chamber

The STM Chamber connects to a double walled cylindrical cryostat above. The inner compartment of the cryostat encloses up to 4 l of liquid Helium (LHe) in order to cool the sample down to a temperature of at best 5 K. The outer cryostat compartment encloses up to 14 l liquid nitrogen (LN_2) in order to thermally shield the LHe from room temperature. Both cryostats need to be refilled every 72 h. Two shields, respectively connected to one of the cryostat compartments, extend into the bottom main part of the chamber, surrounding the STM. They cool it by heat dissipation and shield it from the outside. In cooling position, the STM is in direct thermal contact with a cold finger on the bottom of the cryostat. In measurement position, the STM hangs freely from springs connected to the top of the cryostat. The detailed set-up and operating principle of the beetle-type STM was previously described by K. Lucht [26]. The pressure in the STM chamber is below 2×10^{-10} mbar, which is accomplished by an ion getter pump in combination with the cryo effect of the cold cryostat shields. The pressure is tracked by a hot cathode gauge.

2.3.2 Preparation Chamber

The STM chamber horizontally connects to the preparation chamber, such that all contaminating preparation steps can be performed outside the STM chamber. The pressure in that chamber is below 2×10^{-9} mbar, which is accomplished by an ion getter pump and a titanium sublimation pump (TSP). The preparation chamber provides a sputter gun for sample cleaning, as well as a sample garage, a quadrupole mass spectrometer (QMS) and a hot cathode gauge for pressure measurement. All preparation steps as described in *Sec.* 2.4 are carried out in that chamber.

The sample transfer is navigated between chambers on a x,y,z,φ-manipulator. Once a sample holder is clamped onto the manipulator, the respective cable connections to the heating wires and thermocouples on the sample holder are closed. The sample temperature can thus be read off and controlled via the manipulator wiring. On the sample holder, the sample is located on top of the contact heating, which is used for resistive heating of the sample during the preparation (see. *Sec.* 2.4). The manipulator furthermore provides an internal continuous flow cryostat which can be either run with LHe or LN_2 which allows a sample cooling up to 23 K. The Preparation Chamber is linked to the Molecule Deposition Chamber as well as the Load Lock.

2.3.3 Molecule Deposition Chamber

All other substances than the sample itself, used for the preparation, are led in to the Preparation Chamber via the Molecule Deposition Chamber. Gaseous substances, such as Xe in the case of these studies, can be introduced to the Molecule Deposition Chamber via a leak valve, as outlined in purple in *Fig.* 4. Up to two pressurized gas bottles can be connected to the leak valve via *Swagelok* gas lines.

Solid substances, such as DAF in the case of this studies, can be introduced to the Molecule Deposition Chamber via an evaporator (see *Sec.* 2.4.3) as outlined in dark green in *Fig.* 4.

The purity of a dosed substance in the Molecule Deposition Chamber is analyzed by a QMS. The pressure is below 5×10^{-9} mbar which is accomplished by a *turbo molecular pump* (TMP). The pressure in the Molecule Deposition Chamber is tracked by a cold cathode gauge.

2.3.4 Load Lock

The Load Lock connects to the Preparation Chamber parallel to the Molecule Deposition Chamber. A new sample can be transferred from the Load Lock into the Preparation Chamber by the transfer rod after the Load Lock is being pumped. A pressure of 5×10^{-9} mbar is accomplished by using a TMP with a pre-vacuum system containing a mini TMP and a diaphragm pump.

2.4 Preparation

2.4.1 Preparation of the Ag(100) single crystal

The Ag(100)-single crystal is cleaned of impurities by three cycles of consecutive sputtering and annealing.
Sputtering is performed by stationary introduction of *neon* (Ne (Westfalen, purity: 4.0)) to the UHV through the sputter gun's correlated leak valve. Surface impurities are ablated from the sample by Ne-ion bombardment by means of the sputter gun.
Annealing is performed via the resistive sample heating on the sample holder. The heat promotes diffusion to counter surface roughnesses, as well as the release of implemented Ne-atoms to give raise to planar terraces.
The cleaning cycle durations are shortened over the course of the preparation. This allows the largest possible cleaning effect at the beginning, but avoids succeeding diffusion of contaminants from subsurface layers in the end. The characteristic parameters of all Ag(100) purification steps and cycles are listed in *Tab.* 1.

Table 1: Parameters of Ag(100) preparation. Preparation step duration t, sample temperature T_S, kinetic energy of Ne-ions $E_{kin,Ne}$, Ne-pressure p_{Ne}, sputter current I_s, resistive heating current I_h, heating bias U_h

Param.	Sputtering			Param.	Annealing		
cycle	1	2	3	cycle	1	2	3
t/min	45	25	3	t/min	25	5	2
$E_{kin,Ne}$/eV	1	1	0.5	T_S/K	900	900	820
p_{Ne}/mbar	5×10^{-5}	5×10^{-5}	5×10^{-5}	I_h/A	2.6	2.6	2.3
I_s/μA	0.7	0.7	0.3	U_h/V	6.7	6.7	5.3
T_S/K	298	298	298				

2.4.2 Xe Deposition on Ag(100)

The target sample temperature regime for Xe deposition is 70 K – 75 K, aiming for monolayer formation. The target desorption temperature T_{end} of 70 K is estimated from previous temperature programmed desorption(TPD)-studies in which the desorption temperature of the Xe-monolayer was determined to be 81 K and the multilayer desorption found below 60 K[1]. The deposition temperature was furthermore confined within the determined temperature interval according to TPD-studies of the comparable system of Xe on Ag(111) from the literature [27], which reports a Xe-monolayer desorption temperature of 75 K and multilayer desorption above 65 K.

The introduction of Xe into the UHV is carried out under flow trough conditions via a leak valve installed on the Molecular Deposition Chamber. For this, the gate valve between Molecular Deposition Chamber and its associated TMP is closed by two thirds, the gate valve between the Molecular Deposition Chamber and the Preparation Chamber is opened completely and the pressure within the Preparation Chamber is adjusted to 2×10^{-8} mbar by Xe inlet through the leak valve.

The procedure is outlined in *Fig.* 5 and key parameters are listed in *Tab.* 2.

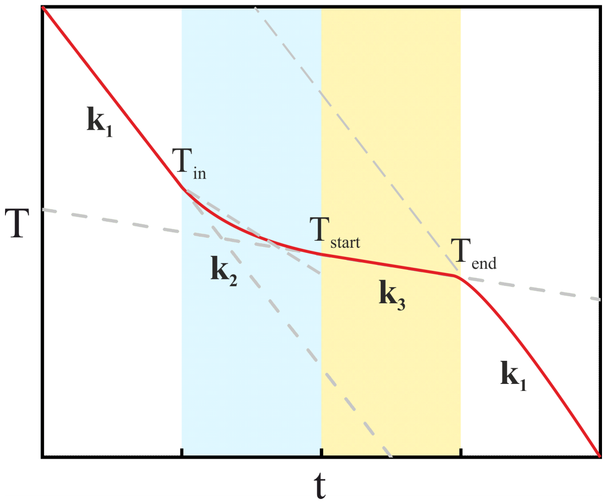

Figure 5: Xe deposition: schematic subdivision of cooling regimes in the temperature T versus time t plot: Sample temperatures T_{in}, T_{start}, T_{end} at the onset of the Xe inlet, at the deposition onset and the end of the Xe inlet; sample cooling rates k_1 from RT to T_{in}, k_2 from T_{in} to T_{start}, k_3 from T_{start} to T_{end}

Table 2: Parameters of Xe deposition: Xe-pressure in Preparation Chamber p_{Xe}; sample temperatures T_{in}, T_{start}, T_{end} at the onset of the Xe inlet, at the deposition onset and the end of the Xe inlet; sample cooling rates k_1 from RT to T_{in}, k_2 from T_{in} to T_{start}, k_3 from T_{start} to T_{end}; respective time intervals t_1, t_2, t_3

p_{Xe}/mbar	2×10^{-8}		
T_{in}/K	120		
T_{start}/K	75		
T_{end}/K	70		
	1	2	3
k/(K/s)	0.049	0.015[a]	0.010
ΔT	178	45	5
Δt	60	80	5 – 8

[a] Ideally aimed for to be much smaller; low rate is the result of difficulties in controlling the cooling and counteracting mechanism. To be shortened in the future.

---

[1] due to a malfunction in temperature recording, only the key points of the ML desorption peak can be given: peak onset $T = 81$ K, maximum: $T = 110$ K, end: $T = 110$ K

The sample is cooled down in four regimes with LHe cooling. The manipulator is counterheated for precise temperature regulation and stabilization. The cooling from room temperature RT to the Xe inlet temperature T_{in} is carried out quickly with maximum LHe flow rate k_1 in order to minimize the adsorption of contaminants. The cooling rate is slowly decreased in the regime between T_{in} and the deposition onset temperature T_{start} in order to reach the target cooling rate k_3, which gives an average cooling rate k_2 in the intermediate range. The cooling rate k_3 is chosen to give a deposition time of 5 min between T_{start} and T_{end} and corresponds to an expected exposure of 6 Langmuir. After reaching the target temperature T_{end}, the Xe inlet is stopped immediately by closing the gate valve to the Molecular Deposition Chamber and the Xe is pumped out of the Preparation Chamber by opening the gate valve to the Load Lock. The cooling speed is maximized to cool the sample down to 30 K in order to transfer it to the STM.

2.4.3 DAF Deposition on Ag(100)

The evaporation of the DAF-molecules for the solid material's transition into the UHV is accomplished within a molecular evaporator (FOCUS OMICRON EFM3T).

This evaporator consists of a copper main body. The substance to be evaporated can be introduced in its interior within a chemically inert quartz crucible. The crucible opening is directed to the UHV chamber. A rotatable shutter can be opened to enable the evaporation. The shutter cannot be sealed vacuum-tight. The temperature of the crucible is controlled by thermocouples and can be increased by resistive heating as well as cooled by water flow cooling.

Prior to its deposition on Ag(100), DAF is heated slowly under argon atmosphere from its storage temperature of 253 K to room temperature, in order to avoid water condensation during the transfer into the evaporator. The transfer into the crucible is performed quickly under air exposure, in the absence of light. After immediate installation of the evaporator at the Molecular Deposition Chamber, all air is removed by UHV pumping while the crucible shutter is closed. The evaporator is baked out overnight at 393 K, while the DAF-temperature inside is constantly kept at 288 K.

The vapor pressure of DAF is sufficiently high that no further heating is required to allow sublimation under UHV conditions. The DAF-deposition is carried out once the evaporator is re-cooled to room temperature such that the DAF-pressure within the Molecular Deposition Chamber stays constant, as follows: The pristine Ag(100) sample is cooled to 53 K or 45 K) by LHe-cooling on the manipulator in the Preparation Chamber, in order to avoid Xe-vaporization but still allow maximum molecular movement. The gate valve between the Molecular Deposition Chamber and the Preparation Chamber is opened. The Ag(100) sample is positioned in front of the Molecular Deposition Chamber, facing

its center and hence the evaporator outlet. The shutter of the evaporator is opened for a deposition time of 60 s and closed afterwards. The sample is moved away from the gate valve before it is closed to avoid contamination by mechanical desorption. The sample is rapidly cooled down to 30 K and transferred into the STM.
The experimental parameters of the DAF-deposition are listed in *Tab.* 3.

Table 3: Parameters of DAF-deposition. Crucible temperature T_C, sample temperature T_S, deposition time t_D, DAF-pressure in closed Molecular Deposition Chamber $p_\mathrm{MOL,\,DAF}$, pressure in Preparation Chamber $p_\mathrm{Prep,DAF}$ when Molecular Deposition Chamber is opened

T_C/K	T_S/K	t_D/s	$p_\mathrm{MOL,DAF}$/mbar	$p_\mathrm{Prep,DAF}$
288	45,53,63	60	2×10^{-8}–1×10^{-7}	1.6×10^{-9}–8.8×10^{-10}

2.5 Software

All analyzed STM images are treated the same way unless further specified: CreaTec imaging and processing software “Pstmafm_ver31_2016082” is used for basic data processing of the images, such as the execution of plane corrections (in all cases) and the low pass filtering (if indicated) as well as for recording line scans.
The WSxM software [28] is furthermore used for more specific treatments such as Fourier analysis, data extraction of chosen image areas (Polygon function) in order to process them e.g. for height histogram generation. The flooding function of WSxM is used to generate substrate-free image sections of islands. These islands are analyzed in area size and fractal dimension studies. These latter analyses are performed using the ImageJ plugin FracLac.
The data analysis and visualization program “Origin Pro2018” and the graphics editor “CorelDRAW 2017” are used to analyze the data.

3 Results

3.1 Ag(100)-Substrate and Piezo-Constants

Prior to this work, it was accomplished to improve the thermal insulation of the LT-STM-system by the removal of a thermal bridge in the STM. As a result, the achievable minimum temperature could be reduced from 8 K to 5 K. It is therefore required to ensure that the piezo constants of the scan performing piezos are still valid or to recalibrate them, if necessary.

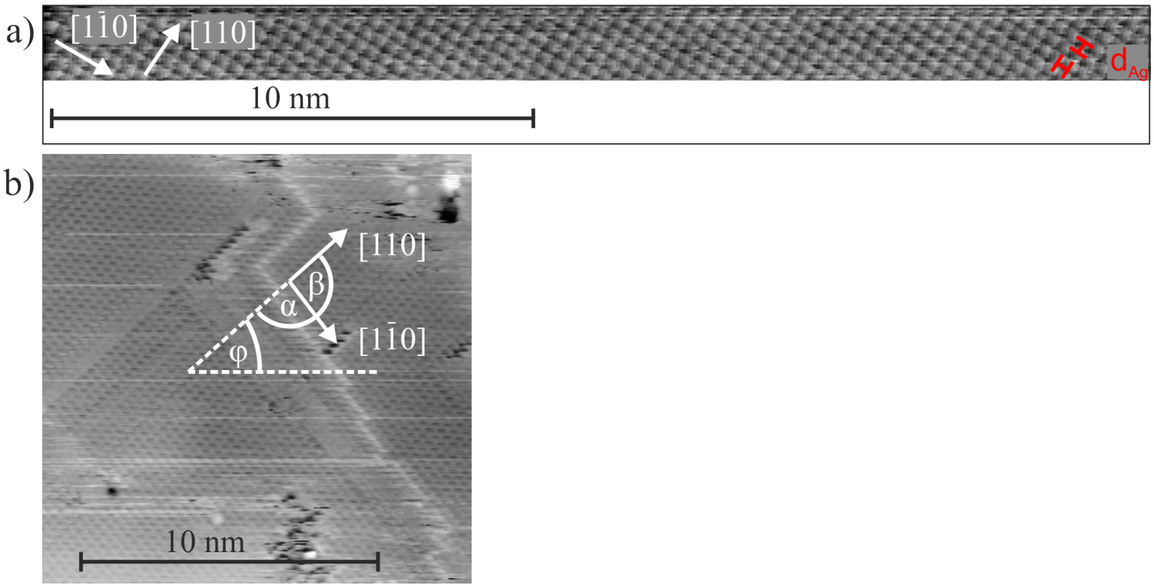

Figure 6: STM images from different measurement periods; a) Atomic resolution of Ag(100), used for orientation determination of the Ag-lattice as reference during Xe alignment determination; tunneling parameters: $I_t = 77\,\mathrm{pA}$, $V_t = 0.9\,\mathrm{mV}$, white arrows: primitive unit vectors; b) Pseudo atomic resolution of Ag(100), rotated relatively to (a), evidence for lattice orientation during DAF studies, tunneling parameters: $I_t = 16\,\mathrm{pA}$, $V_t = 7\,\mathrm{mV}$; white arrows: primitive unit vectors

This examination is performed on the Ag(100) surface. The orientation of the Ag(100) lattice is determined as reference for further adsorbate alignment studies at the same time. The average inclination angle ϕ of the Ag[1 1 0] vectors relative to the image y-axis and the angles α and β between the primitive unit vectors are determined from several atomic resolution images. The respective angles are marked in *Fig.* 6a). The average inter-atomic distances d_{Ag} (comp. *Fig.* 6b)) along both primitive vectors are determined at the same time. This procedure, as analogously applied to deposited Xe is further outlined in more detail in *Sec.* 3.2. In comparison to images from different sample preparations, a rotation of the Ag(100) lattice relative to the image y-axis is observed. Thus, first the Ag(100)

lattice is analyzed based on measurements taken during the measurement period of pure Xe layer studies. At the end of this chapter the differing Ag(100) orientation for DAF measurements is discussed.
The quantified geometric characteristics of the lattice, using the x- and y- piezo constants of 3.068 pm V^{-1}, valid for 8 K are listed in *Tab.* 4.

Table 4: Characterization of atomic distances d_{Ag} of Ag(100) scanned along the crystal direction $[h\,k\,l]$ with a number of line scans m over a total number of atoms n; inclination angle ϕ of the Ag[1 1 0] direction relative to the image y-axis; angle between the primitive unit vectors α and β, their standard error of the mean σ_{E}, compared literature values indicated by (lit) and the corresponding relative deviation Δ(lit), most plausible interpretation of measurement values as referenced by the label ref in *Tab.* 4

	d_{Ag}		$\sphericalangle$			
$[h\,k\,l]$	[1 1 0]	$[1\,\bar{1}\,0]$		ϕ	α	β
d/pm	292	315	$\sphericalangle$	31°	92°	88°
σ_{E}/pm	14	7	σ_{E}	1°	2°	2°
m	115	85	m	115	85	85
n	554	569	n	554	554	554
d(lit)/pm	289	289	$\sphericalangle$(lit)	–	90°	90°
Δ(lit)	+1.0%	+9.0%	Δ(lit)	–	+2.2%	-2.2%
ref.	–	–		33°	90°	90°

The statistical error σ_{E} is the standard error of the mean over the number of measurements. For the angle measurement by STM, however, a systematic intrinsic inaccuracy of about 5° is assumed, due to piezo creep. As this error is larger than the statistical error, the latter one is not taken into account in the following. The determined values for d_{Ag} differ between (292 ± 14) pm and (315 ± 7) pm along both primitive vectors. The difference in the lattice parameters indicates a commonly present influence of creep during these image recordings, since it is unreasonable that the temperature adjustment affects the x- and y- piezos in different manners. The measured lattice angle corresponds to the literature value within the scope of the error. However a distortion is observed since α is consistently overestimated and β underestimated in this work.
Both primitive surface lattice constants d_{Ag} are bigger than the known literature value of 289 pm. A decrease of the piezo constants in the range of 1–9% is hence required to make the measured lattice parameters match their literature values. However, the need of an adjustment over 9% seems odd considering a temperature change of less than 3 K.
Due to the insufficient reliability of this calibration the conventional piezo-constants are kept in oder to avoid a falsifying adjustment, since the required decrease cannot be deter-

mined more precisely. It cannot be evaluated what proportion of the occurring distortions is caused by the creep and which one by the error of the constants.
The most plausible vector orientation, thus, is constructed based on the single image with the lowest deviation from a right angle. The average inclination angle of both primitive unit vectors is measured and the one with lower deviation is considered the more reliable. A perpendicular path to this unit vector is constructed to generate the idealized second primitive vector. The resulting orthogonal cross is used as reference system for the Ag primitive unit directions. The characteristic angles of this reference system are listed in *Tab.* 4 with the label “ref”.
The inclination angle gained from this idealizing approach is $i = 33°$, which corresponds to the depiction of all Ag-axes in following polar diagrams and is used further for relative angle determination.
The STM image that is the foundation of this reference grid is shown in *Fig.* 6a). *Fig.* 6b) shows pseudo atomic resolution of the Ag(100) lattice as it is obtained during the measurements of DAF coadsorption to Xe. The orientation is congruent to the later determined DAF molecular orientation as well as the pushing trace of DAF manipulation. For geometrical reasons, further discussed in *Sec.* 3.4.2, it is concluded that the orientation of the pseudo atomic structure maps the orientation of the real Ag(100) lattice.

3.2 Local Xe-layer Characterization on Ag(100)

The deposited Xe layer is discussed in two sections. This section is focused on the local crystallographic characterization of Xe on Ag(100) in relation to the underlying substrate lattice. A larger range classification of the Xe layer concerning its coverage is discussed in *Sec.* 3.7. A local hexagonal super-structure is determined after the Xe deposition, as shown in *Fig.* 7a). Beyond these regions, the quadratic surface structure of the Ag(100) is recorded on the same sample as shown in *Fig.* 7b). According to *Sec.* 3.2.1, the hexagonal structure is identified as Xe(111).

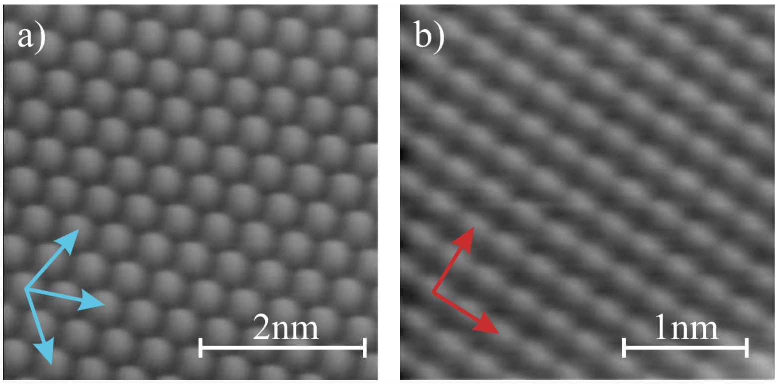

Figure 7: Atomic resolution image of a) Xe(111) on Ag(100) and b) Ag(100); Arrows in the left corners indicate the orientation of the closed packed directions, tunneling parameters: (a) $I_\mathrm{t} = 31\,\mathrm{pA}$, $V_\mathrm{t} = 3\,\mathrm{mV}$, (b) $I_\mathrm{t} = 31\,\mathrm{pA}$, $V_\mathrm{t} = 2\,\mathrm{mV}$

3.2.1 Surface Lattice Constant of Xe Adsorbed on Ag(100)

The mean atom distances along the three closed packed vectors of the hexagonal lattice are independently determined by the height profiles along the atom rows of the respective orientation. The outermost atom distance of a row is divided by $(n-1)$, where n is the number of peaks in the row.
The determined mean closed packed Xe atom distances are listed in *Tab.* 5 calculated from a number of line scans m over a total number of atoms n.

Table 5: Characterization of Xe atom distances d_{Xe} of the Xe superstructure on Ag(100) scanned along the crystal direction $[h\,k\,l]$ with a number of line scans m over a total number of atoms n with the standard deviation σ and the relative deviation from ideal hexagonal proportions Δd in relation to the smallest value for d_{Xe}

measure	Xe		
$[h\,k\,l]$	[1 1 0]	[1 0 1]	$[1\,\bar{1}\,0]$
d_{Xe}/pm	458	482	476
σ/pm	3	3	4
m	729	727	842
n	951	959	1051
Δd	+0%	+5.4%	+4.0%

The surface lattice constants averaged over all three closed packed directions between the hexagonally arranged protrusions is then determined to be (473 ± 5) pm. Known surface constants of Xe superstructures on other metals are d_{Xe}=450 pm for hcp Xe on Cu(100) and Ag(111) and d_{Xe}=448 pm for hcp Xe on Pd(100) [21]. These literature values are stretched by about 3% compared to the bulk value d_{Xe}=438 pm. In the present case the surface lattice parameter is stretched by about 7% compared to the bulk value. The determined lattice constant of (473 ± 5) pm for Xe(111) on Ag(100) is comparatively larger than the known cases of other metal substrates, but in the same order of magnitude. Considering that the known distances between the Ag atoms are overestimated between 1.0% and 9.0%, as shown in *Sec.* 3.1, it is probable that the measured atomic distances of the Xe layer must be corrected by factors of this magnitude.

3.2.2 Local Xe-Layer Height Determination

Fig. 8a) shows an atomic resolution image of a Xe island with hexagonal lattice geometry on Ag(100). The substrate is also imaged atomically at the top and the bottom parts of the image.

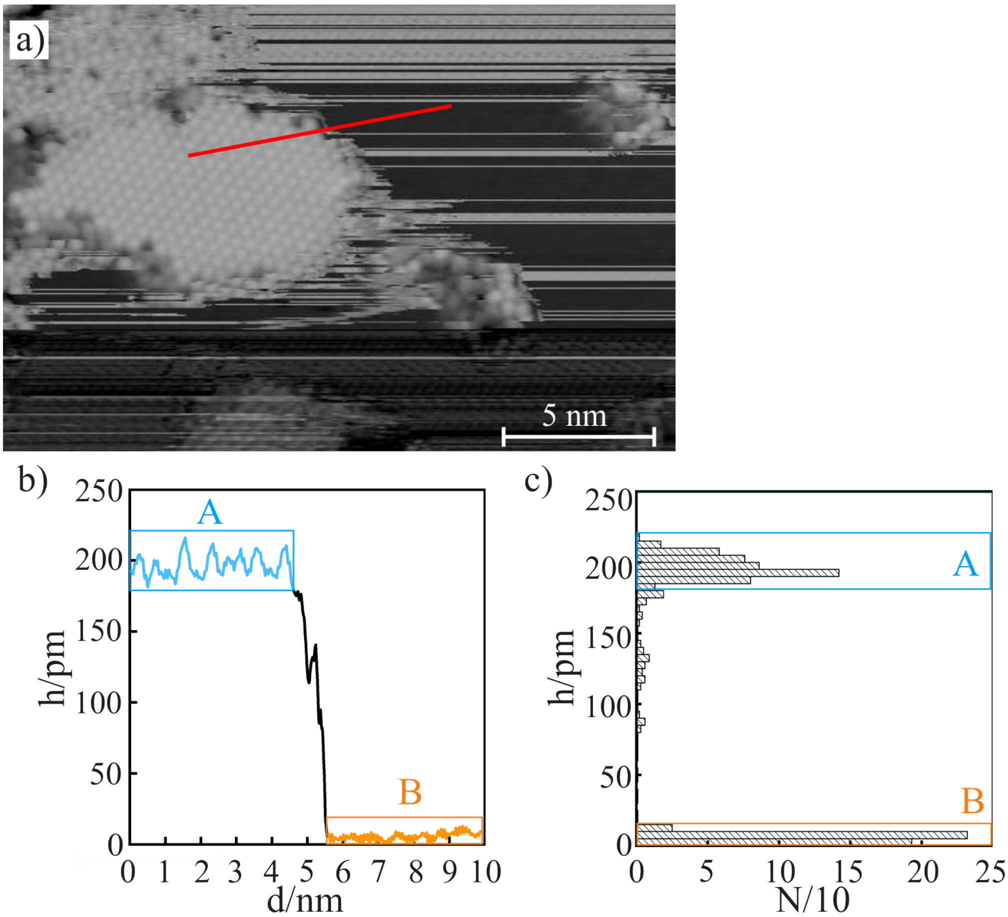

Figure 8: a) Atomic resolution of Xe island on Ag(100), red line: line scan path of (b); tunneling parameters: $I_\mathrm{t} = 20\,\mathrm{pA}$, $V_\mathrm{t} = 0.9\,\mathrm{mV}$; b) Apparent height h profile along the red line path with distance d; c) corresponding height histogram of (b) with the number of counts N

The image of the substrate varies in rectangular sections running along the scan direction. This indicates an unstable tip that occasionally picks up or drops a particle, which changes the way Ag is imaged as the tip interaction changes.

The height of the island is determined in relation to the smooth, homogeneous areas of the substrate. A line scan across the island edge is drawn along the red line in *Fig.* 8a). The height profile and the corresponding height histogram are shown in *Fig.* 8b) and c). The island height is calculated as the difference between the mean values of the selected height intervals A and B, assigned to the island and the substrate, respectively. By these means, the average island height is determined to be $(191 \pm 7)\,\mathrm{pm}$.

Since there are hardly any areas that allow the drawing of perpendicular line scans through the island edge due to the changes in the substrate image, the dataset is limited to the presented measurement and may hence be distorted by statistical errors. The theoretical step height of the Xe bulk as introduced in *Sec.* 2.2.2 is 356 pm. Since no further steps are observed at the island edges, it is concluded that a monolayer Xe island is imaged here.

3.2.3 Superstructure Characterization

This sections is focused on analyzing the alignment of Xe(111) to Ag(100) to investigate the Xe superstructure. The angles between all closed packed lattice rows of Xe are analyzed separately and their relative orientation to the Ag closed packed rows are determined. On that account the slopes of the respective atomic rows are determined for angle calculation. The slope is calculated among two coordinate points of each line scan path drawn for distance determination in the x-y-plane of the STM images.

For *Fig.* 7a) and *Fig.* 8, an equal orientation of the Xe(111) closed packed rows is observed. This is illustrated by the polar diagram in *Fig.* 9 of these two regions (all closed packed rows shown).

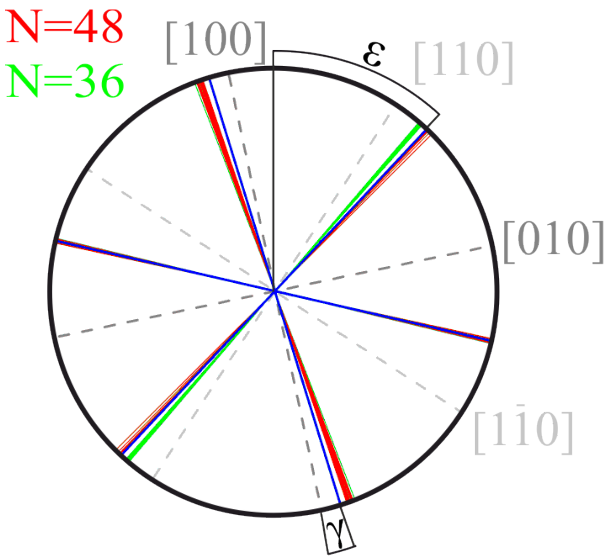

Figure 9: Polar diagram of orientiation of the Xe closed packed rows, measured in the image region of *Fig.* 8 (red) & *Fig.* 7 (green) superimposed to the Ag lattice (gray), idealized interpretation: angles adjusted to $\theta = \omega = \phi = 60°$ along the averaged direction of lowest standard deviation (blue)

Table 6: Average angles of the atomically mapped closed packed rows of Xe on Ag(100) according to *Fig.* 9 with standard deviation σ

	ϵ	θ	ω	ϕ	γ
Exact values obtained					
∢	42°	57°	62°	61°	8°
σ	1°	1°	2°	2°	2°
Most probable interpretation					
	ϵ	θ	ω	ϕ	γ
∢	43°	60°	60°	60°	5°

The different angles determined are: the angles θ, ω and ϕ between the closed packed rows (clockwise starting from the image y-axis), the inclination angle ϵ between the steepest raising closed packed vector and the image y-axis as well as the smallest angle γ between any closed packed Xe row and Ag lattices vectors of high symmetry (primitive and conventional unit vectors). These angles are displayed in *Tab.* 6.

The considered crystal directions are aligned closely parallel. However, the small angle deviation of $(2 \pm 1)^\circ$ is to be noted in the inclination angle of the Xe[1 1 0] direction, and the average spanning angles of the hexagon deviate from the ideal 60° angle up to a maximum difference of 3°. Within the scope of angular accuracy of the STM of ±5° these angle differences can be neglected. An equilateral hexagonal structure is hence a plausible possibility.

The most plausible vector orientation, thus, is constructed by extrapolating an ideal hexagon aligned to the averaged vector of the slope of the lowest standard deviation. The inclination angle is determined to be $\epsilon = (43 \pm 1)^\circ$ in this case, listed for comparison in the bottom part of *Tab.* 6 and the referring orientations of the rows are plotted in blue in *Fig.* 9. The angle γ is accordingly determined to be $\gamma = (5 \pm 2)^\circ$. Regarding the previously mentioned angular accuracy of the STM of ±5° an alignment of the Xe to the Ag [0 1 0] direction is conceivable. Further measurements are required for validation.

However, small deviations in the relative angle or the ratio between the atomic distances of the two grids quickly add up over a long range and lead to increasing shifts. Therefore the determination of the exact super-structure is impossible with the given uncertainties. This analysis is based on different images for each respective species. Relative information about Ag and Xe may easily be altered by varying distortions, such as creep, affecting the different images in different ways. Therefore, another method is consulted which more accurately retains the relative orientations of the lattices:

Both atomic species are recorded in the same image, as introduced in *Sec.* 3.2.2. Thus, they are equally subject to any conceivable type of recording distortion. Relative informations such as the angles between the substrate and adsorbate lattice are therefore analyzed based on this image as shown in *Fig.* 10.

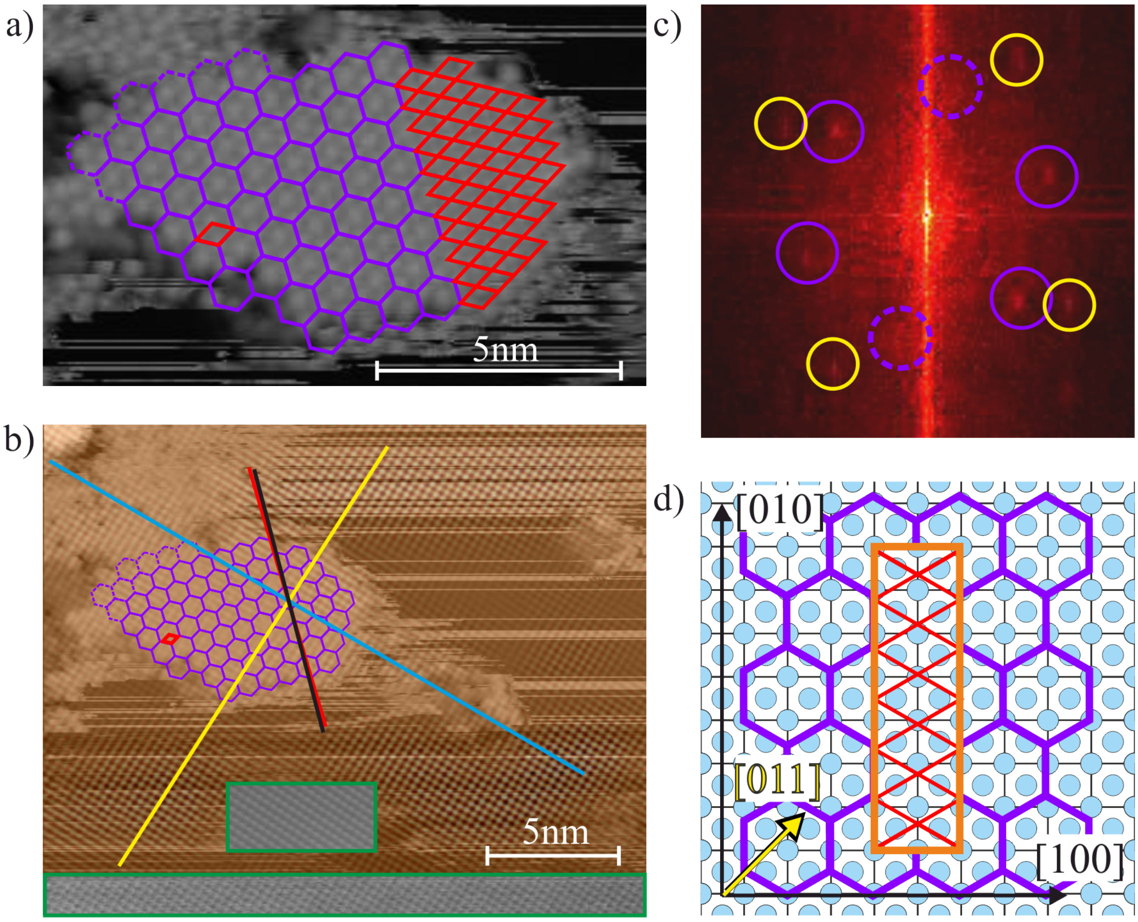

Figure 10: Xe island on Ag(100) a) atomic resolution STM image. Surface unit cell marked by red rhombus in left island part. Periodicity of the crystalline lattice displayed by red grid overlay on right island side. Purple hexagonal grid: bigger super cell overlay (atomic positions on vertexes and centers of hexagons) to reference periodic atomic positions with better visibility on larger scale zoom out view in (b); b) Overlay of original STM image in black and and white with reverse FT pattern in brown generated under consideration of the yellow circled signals in (c), tunneling parameters: $I_\mathrm{t} = 20\,\mathrm{pA}$, $V_\mathrm{t} = 0.9\,\mathrm{mV}$, blue and yellow line: extension of FT pattern, black line: drawn along Xe$[1\,\bar{1}\,0]$ direction, red line: constructed in 45° angle to blue line, true to scale atomic resolution images of Ag(100) in green boxes for comparison; c) FT spectrum of the total image area depicted in (b), including the Xe island and the substrate; d) Super structure model of Xe on Ag(100), unit cell in orange

An ideal hexagonal grid is placed over the island in *Fig.* 10a) (red grid). This long range grid fitting comes with the advantage that both the angle and the size of the unit cells are fitted to the average grid structure to represent the most accurate mean geometry possible.

Fig. 10b) shows the reverse *Fourier transformed* (FT) image of *Fig.* 10a). The respective FT-spectrum is shown in *Fig.* 10c). The FT spectrum is filtered by cutting out the yellow circled signals, which are assigned to the Ag(100) lattice due to their quadratic unit cell, neglecting the other regions in the FT spectrum in order to generate *Fig.* 10b). by reverse FT. However, the resulting quadratic pattern has twisting angles of 93° and 87° between its closed paced rows.

The deviation of the unit cell in Fourier space from the ideal square origins from minor image distortions in the original image. The inner, purple circled pattern can be assigned to the hexagonal Xe(111) structure. This assumes that the two missing expected signals, indicated by dashed lines, are superimposed by the intensities of the vertical axis caused by the high amount of horizontal image disturbances. The reverse FT pattern is superimposed in *Fig.* 10b) as half transparent, brown top-layer on the original image in black and white in the background. The purple hexagons represent the hexagonal grid as introduced in *Fig.* 10a) outlined by the red rhombuses, but with a larger super cell drawn on top of the atomic positions for better overview. The reverse FT grid lines of Ag(100) are extrapolated as yellow and blue lines that represent the directions $[1\,1\,0]$ and $[1\,\bar{1}\,0]$. The gray image sections framed in green in in *Fig.* 10b) are different and independent images of atomically resolution of Ag(100) in order to allow comparison and plausibility evaluation. These references agree satisfactorily to the pattern within the scope of the uncertainties discussed in *Sec.* 3.1. The red line is guided along the $[1\,\bar{1}\,0]$ direction of the Xe. The black line is added in an angle of 45° to the yellow line, representing the Ag$[1\,0\,0]$ direction vector.

The red and the black lines are rotated by 2° to each other. Accordingly, the Xe closed packed row seems to be aligned to the Ag$[0\,1\,0]$, within the scope of the assumed angle uncertainty of 5°. This assumption agrees with other experiments that find a Xe monolayer incommensurate but aligned with the substrate, such as observed for the similar case of Xe deposition on Ag(111) at 77 K [21,22].

The alignment to the Ag$[0\,1\,0]$ direction would furthermore suggest a conceivable model of periodicity as shown in *Fig.* 10d). The corresponding unit cell of the super structure is drawn in orange.

This super-structure is derived in analogy to the adsorption structure of Xe on Pd(100) determined by LEED-experiments [29]. Within this super-structure model the opposite sides of the hexagons (short diagonal distance) hold a distance of two lattice parameters a of the underlying substrate. In case of the Ag the distance of two lattice parameters equals:

$$d_{2a(\mathrm{Ag})} = 2 \cdot 409\,\mathrm{pm} = 818\,\mathrm{pm} \tag{2}$$

This is in good agreement with the short diagonal distance x of a Xe hexagon, calculated from the measured average Xe-Xe distance of $d_{\mathrm{Xe}} = (473 \pm 5)\,\mathrm{pm}$ under the assumption of an 60° angle:

$$x = d_{\mathrm{Xe}} \cdot \sqrt{3} = (819 \pm 9)\,\mathrm{pm} \tag{3}$$

This superstructure unit cell is, hence, a concept based on geometrical considerations, drawn in analogy to observations from literature, but plausible within the scope of the uncertainties of the measured lengths and angles.

Due to the different lattices constants, a stretch of d_{Xe} by 5%, is required to transfer this superstructure from Pd to Ag. Since the lattice parameters of Ag and Pd vary only by 5%, the transferability of the adsorption behavior of Xe on Pd to Ag seems reasonable given the constant adsorption behavior of Xe. The assumption of this geometry agrees with the general observation that the Xe-Xe distance adapts quite flexibly to that of the substrate without changing its geometry. Among the series of metal (100)-face rare gas layers presently known (fcc (Xe on Pd [29], Xe on Cu [30]) and bcc (Ar on Nb [31]), all show a hcp structure and an alignment of a closed packed direction vector along a preferred substrate axis. This axis is the $[1\,0\,0] \equiv [0\,1\,0]$ one in the case of Pd and Nb and the $[0\,1\,1]$ axis in case of copper. Therefore, it is plausible to consider the proposed structure as candidates for the adsorption structure. However, it cannot be proven that this is the only possible structure to fulfill all geometric criteria of the measured properties within the relatively big uncertainty regime. Any other geometry in the given error frame of ±5° would also be conceivable.

The FT based methodology shows a clear alignment of the super-structure to the Ag$[0\,1\,0]$ while the simple super-imposition of atomic resolution images of both crystal lattices exhibits a larger angle difference. In case of the averaged measured geometry a deviation of 5° is observed in comparison to the result of the FT approach. Within the range of uncertainties both approaches agree with the proposed Xe alignment on the Ag surface. Since regions from the same image face the same distortion for both lattices Xe as well as Ag, the FT approach is assumed to display the alignment between the two structures more precisely. The FT approach indicates an alignment of the super-structure to Ag$[0\,1\,0]$.

3.2.4 Xe Growth on Ag(100) Steps

For areas near the step edges an extensive Xe layer is observed. *Fig.* 11a) shows several steps after deposition of pure Xe.

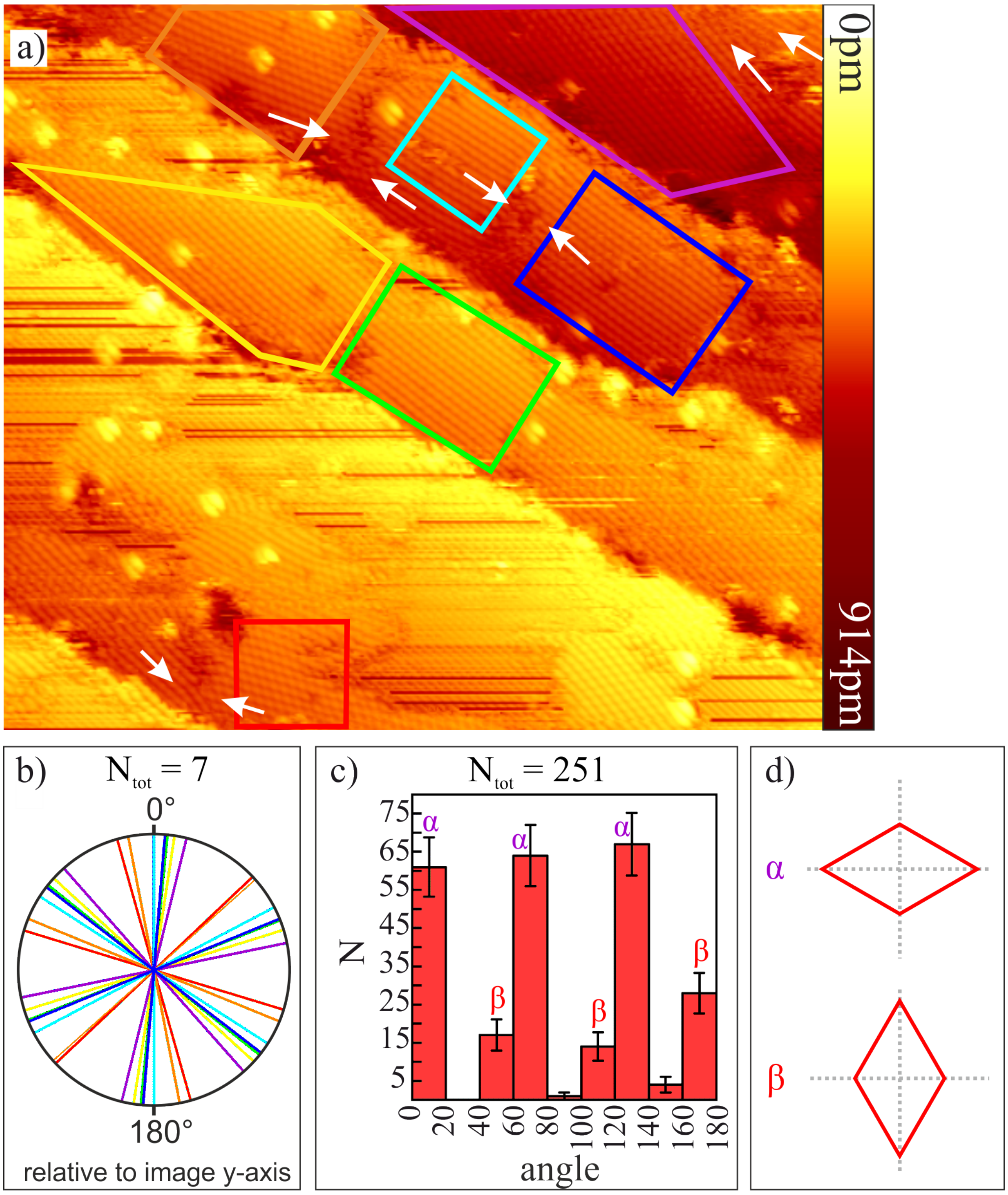

Figure 11: Xe on Ag(100) steps; a) atomic resolution image, colored box indicate Xe domains, white arrows point out domain boundaries, additional protrusions: double tip, tunneling parameters: $I_t = 72\,\mathrm{pA}$, $V_t = 25\,\mathrm{mV}$, frames of domains in the color-coding as used in plot (b); b) Polar diagram of the mean orientation per closed packed row of the islands from (a) in the respective color-coding; c) Histogram of the angle distributions of the closed packed rows relative to STM image y-axis; d) Potential orientation of hexagon in a quadratic lattice

The step height of 200 pm matches the step height of Ag(100). The on top protrusions are caused by a double tip effect. Xe on the terraces is imaged as hexagonal lattice. The STM image reveals the presence of domains. Within the domains Xe is aligned in a hexagonal fashion in varying orientations. These distinct domains are framed in different colors and are analyzed separately. The transitions between different oriented domains are discontinuous junctions due to the occurrence of vacancies, which interrupt the crystal lattice. The occurrence of domains might be promoted by conceivable lattice tension due to the largely stretched Xe lattice parameter (as identified in *Sec.* 3.2.1). Domain boundaries are indicated by two facing white arrows indicating the orientation of the opposed Xe closed packed rows.

Fig. 11b) shows the polar diagram of the Xe lattice represented by the averaged orientation of the three closed packed rows per domain. The individually measured closed packed row orientations are represented in the angle distribution histogram in *Fig.* 11c). The angle is measured clockwise with respect to the image y-axis. *Fig.* 11d) shows two potential orientations of a hexagon in a quadratic lattice. The closed packed rows of both orientations (sides of the respective unit cells) are rotated by 30° with respect to each other. In *Fig.* 11b), the angle between orientations marked in red and purple is 30°. This is interpreted as an alignment of the Xe to the Ag lattice in one of the two symmetrically inequivalent orientations α and β. This is further supported by the histogram in *Fig.* 11c) that shows repetitive peaks for α and β orientation for the analysis over all individual closed packed row orientations. However, *Fig.* 11b) also shows that orientations between α and β are possible (yellow, cyan and blue closed packed row). The occurrence of gradual rotational symmetries without clear restrictions between α and β may be attributed to the rotation dominating influence of pre-adsorbates as described for Xe layer growth on Ag(111) [32]. The transferability of this concept to the present system can be drawn under the assumption of sample contaminations at step edges causing the imaged vacancies. This hypothesis is discussed affirmatively with a clearer resolution of the coadsorbates' contact area for the case of DAF coadsorption in *Sec.* 3.6.

3.3 Layer Characterization of Xe on Ag(100)

For the described deposition parameters, islands of Xe are observed on Ag(100). In this section the islands are classified by analyzing the heights, shapes, areas and the island density. Their authenticity is discussed with regards to conceivable measurement interferences.

3.3.1 Height Distribution

Overview images of the Xe islands deposited at 70 K – 75 K and annealed[2] to 53 K on different sample regions are shown together with their height profiles along the arrow directions and with the corresponding height distribution histograms in *Fig.* 12.

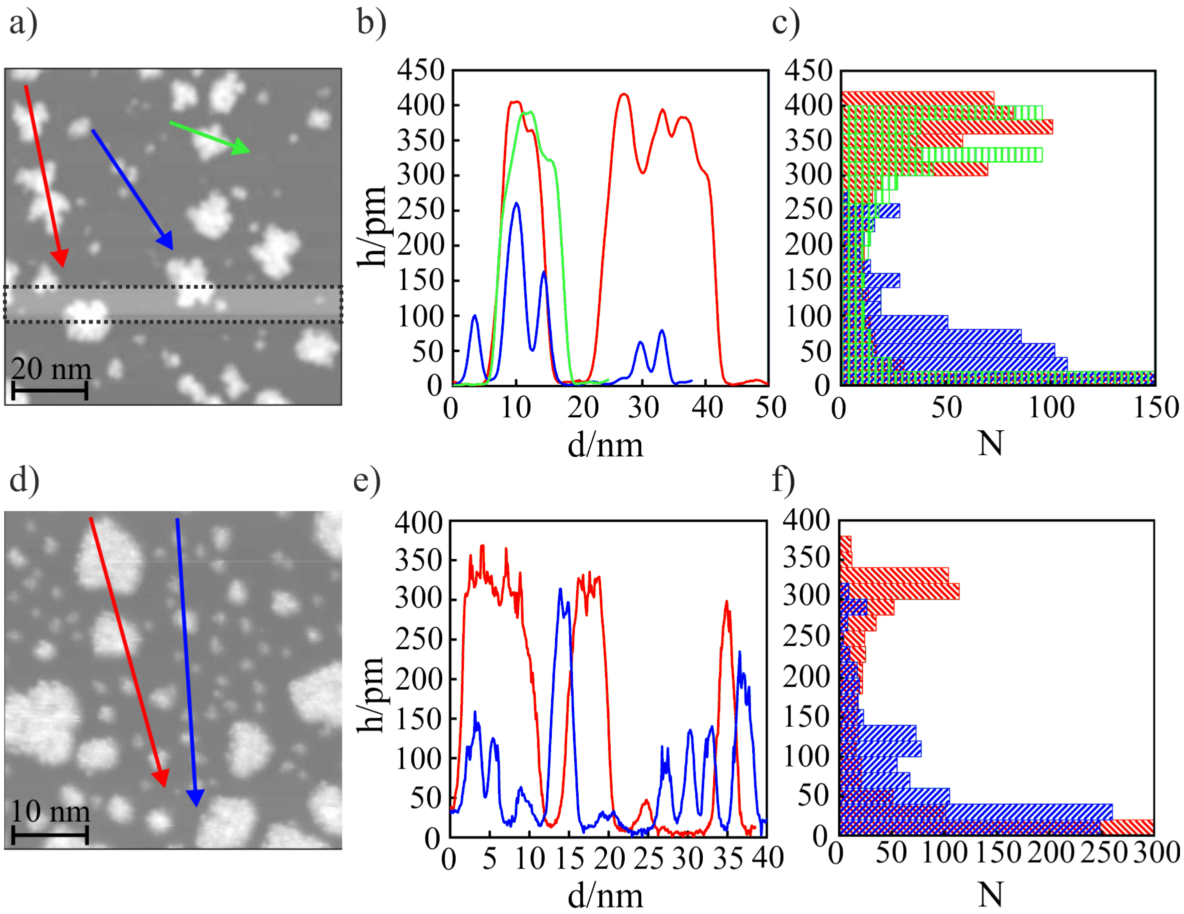

Figure 12: a) STM image of Xe-islands on Ag(100), dotted frame: horizontal section wise changing image, tunneling parameters: $I_t = 11\,\mathrm{pA}$, $V_t = 459\,\mathrm{mV}$; b) Height profiles along the arrows of the respective colors in the STM image; c) Histograms corresponding to the height profiles of (b); d) c.f. (a), tunneling parameters: $I_t = 11\,\mathrm{pA}$, $V_t = 154\,\mathrm{mV}$; e) f) c.f. (b), (c)

The overview images reveal an incomplete Xe island coverage of the sample on terraces. The islands show an irregular morphology. The island morphology is characterized in first place by the histograms of their apparent height distribution. From the STM images it is seen that the islands can be divided into two classes: smaller islands of non-uniform heights, such as displayed by the blue height profiles, and islands of larger lateral extend with irregular shaped fringes, such as corresponding to all other height profiles in *Fig.* 12. The apparent heights of the extensive islands are further analyzed for different islands

---

[2] Annealing process corresponds to miscarried DAF deposition, further discussed in *Sec.* 3.7.4

within the same image. Most of the island images, however, show constantly occurring sample interactions with the tip, which leads to horizontal interference lines or section-wise image changes, such as highlighted by the dotted line in *Fig.* 12a). To evaluate the apparent height of the extensive islands for a larger number of islands, the height profiles are drawn in parallel to the scanning direction through the island centers, inasmuch as there is no local disturbance. As examples, three height histograms generated cumulatively over all height profiles per image are shown for three different images in *Fig.* 13.

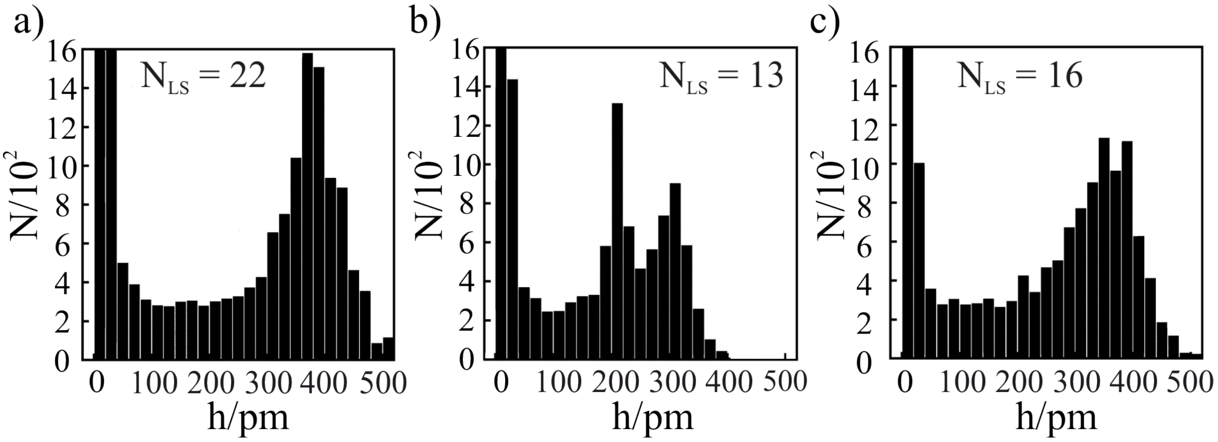

Figure 13: Height histograms of Xe islands adsorbed on Ag for three different STM images, cumulated plots of N_{LS} line scans over N_{LS} island per image; tunneling parameters of respective images: a) $I_{\mathrm{t}} = 36\,\mathrm{pA}$, $V_{\mathrm{t}} = 507\,\mathrm{mV}$; b) $I_{\mathrm{t}} = 30\,\mathrm{pA}$, $V_{\mathrm{t}} = 500\,\mathrm{mV}$; c) $I_{\mathrm{t}} = 14\,\mathrm{pA}$, $V_{\mathrm{t}} = 459\,\mathrm{mV}$

The apparent height distributions of different images differ strongly from each other as the number of peaks and corresponding heights vary. The maximum apparent heights observed in different images varies between 400 pm and 500 pm. Apparent heights up to twice the height of the monolayer of about $(191 \pm 7)\,\mathrm{pm}$ as determined in *Sec.* 3.2.2 (but to be regarded under the changed tunneling parameters in the height profiles analyzed) are frequently observed. The quantitative apparent height values obtained in histograms of different images with different tunneling parameters are not comparable. However the shape of the distributions is generally a comparable property but is found to deviate for each image for the present system. This indicates an amorphous island structure. Potential reasons for the amorphous structure are discussed in *Sec.* 3.7.4.

3.3.2 Fractal Dimensions, Island Sizes and Coverage Density

In order to assess the similarity of the islands, their fractal dimensions D_{F} are analyzed. Fractal dimensions are a measure of the complexity of a shape. For measurements of two dimensional areas, they range from 1D to 2D. 2D corresponds to a completely filled area such as an ideal square. 1D corresponds to a line with no area embedded. The fractal dimension thus reflect how compact or fragmentary a shape is. [33]

The fractal dimension analysis is carried out as follows: The WSxM-function "flooding" is used to differentiate image areas within or outside an island according to a binary scheme of the exclusion criteria "minimum apparent height" and "minimum island size". The "minimum apparent height" is chosen 150 pm as it is sufficiently below the monolayer height. The "minimum island size" is chosen as 0.05 nm^2 as this excludes several disturbances but is smaller than the island size of the atomically resolved island in *Fig.* 8, to make sure no real islands are excluded. The two-colored output graphics are processed to the plug-in FracLac of the scientific analysis software ImageJ [34]. The program screens for separate and distinct island areas by by analysis of the binary colored image and assigns them an identification number. For this the "Analyze Particles"-function is used with no further "minimum island size" chosen and the activated parameter "exclude on edges" function, in order to ignore islands cut by image boundaries. At the same time the area of every island is measured. On that account, the number of pixels assigned to an island is set in relation to the pixel number of the entire STM image with known area. The island density is determined based on the island count per area. Each of these areas is subsequently analyzed according to the box-counting method [33] to determine their fractal dimension. The box-counting method is especially suited for this analysis as it is the most reliable method of fractal dimension determination at nanoscale [35].An example procedure for determining the fractal dimension is shown step by step in *Fig.* 14.

In order to determine the fractal dimension, the island shape is initially approximated by drawing a grid of

(5×5)-pixel boxes, covering the island up to its boundaries. The center position of this boxes is generated randomly and varied for analysis repetitions. If a square contains, to any arbitrary degree, parts of the image area of the color assigned to the island, it is completely associated to the island. Subsequently, the number of squares $N(\varepsilon)$ inside the analyzed shaped area is iteratively decreased while their edge length is increased linearly according to a set constant ("Default Sampling Size", here 4 pixel).

The area assigned to the shape, hence, increases with the box size, since the excess areas of the boxes grow, while the number of boxes decreases. The increase of the box edge length results in a quadratic decrease of the box number. For this reason a general hyperbolic correlation exists between number of boxes associated with the examined form $N(\varepsilon)$ and the box length ε.

In comparison to an ideal hyperbole, as describing a compact area, for high complexity shapes a major increase of $N(\varepsilon)$ occurs once ε leads to box-sizes, which are too big to conform to the fine gaps within the structure. This results in a characteristic alteration in the slope of the hyperbole in the region of high $N(\varepsilon)$, depending on the fine gap structure of the shape. More conveniently, the logarithm of the number of boxes associated with the examined form $\log(N(\varepsilon))$ is plotted against the logarithm of the box size $\log\varepsilon$. The fractal dimension is read off as the slope of the linear region of the plot. In the case presented here, the procedure is repeated 12 times in each case and the average of the results per island is considered.

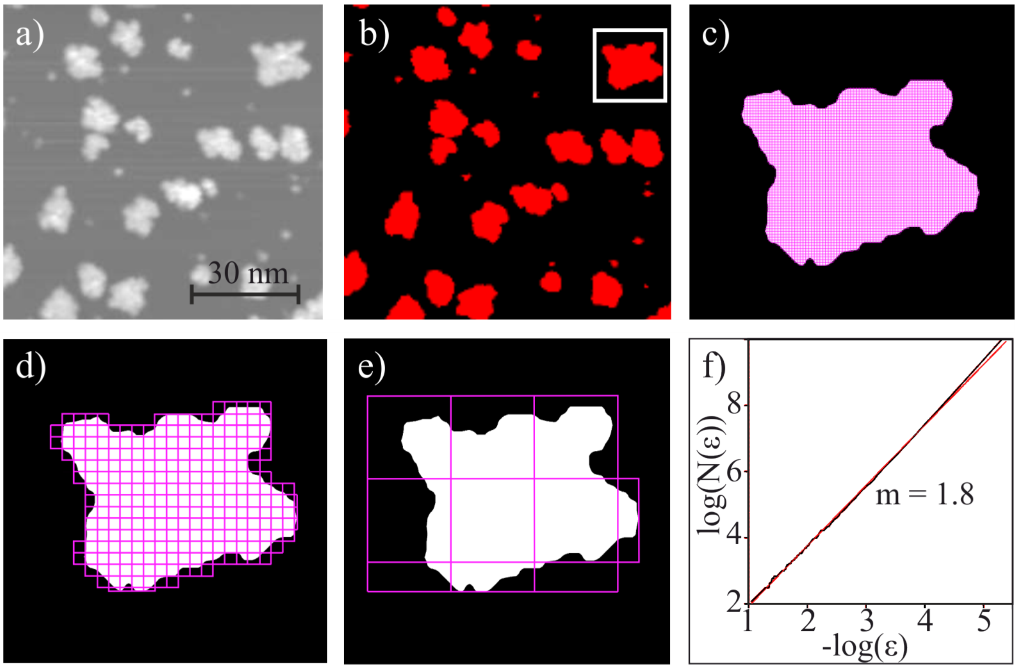

Figure 14: Schematic outline of the fractal dimension analysis for an Xe-islands on Ag(100) of the fractal dimension D_F of 1.8; a) STM-Image, tunneling parameters: $I_t = 30\,\mathrm{pA}$, $V_t = 500\,\mathrm{mV}$; b) binary color map of flooded islands; c)-e) application of the box counting method by iterative box edge increase; f) logarithmic plot of number of boxes associated with the examined form $N(\varepsilon)$ and the box length, the slope m is D_F, black plot: raw data, red plot: linear fit

The island areas A_{island}, the local coverages $\theta = (\sum A_{island})/A_{\mathrm{tot}}$ and the island densities $\rho = N_i/A_{\mathrm{tot}}$ are studied at the same time for the same images. A_{tot} is the total image area and N_i the number of islands per image. The island density corresponds to the number of identified islands per total area of the image. The average coverage is determined to be $\theta = (20 \pm 4)\,\%$. The mean island density is determined to be $\rho = (8 \pm 3) \times 10^{-3}\mathrm{nm}^{-2}$. The Xe-islands are observed in a wide size range from $<3\,\mathrm{nm}^2$ to $275\,\mathrm{nm}^2$. The histograms of the fractal dimension and the area size distribution are shown separately in *Fig.* 15a) and b), respectively, together with their correlation plot c).

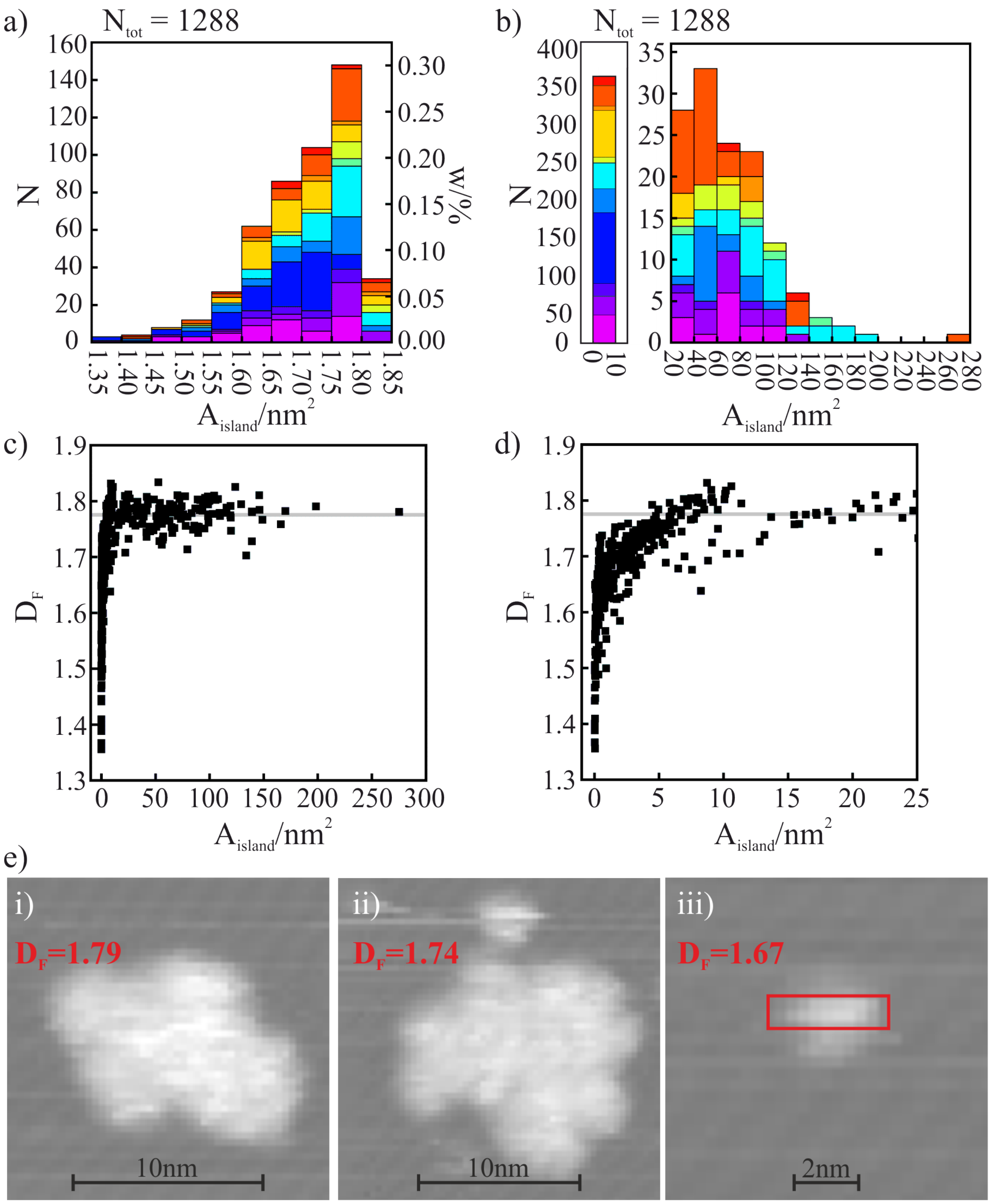

Figure 15: Characterization of N_{tot} Xe-islands on Ag(100); a) Fractal dimension D_{F} distribution; b) Area A size distribution; c) Correlation between D_{F} and A with mean fractal dimension of big islands (>10 nm²) marked as a grey line; d) Zoomed view of (c); e) Islands of different sizes; red box: main protrusion image section of rectangular shape resulting from the pixel shape

For island of 10 nm^2 and bigger the fractal dimension does not depend on the island size (compare the grey line in *Fig.* 15c) and d)) with a mean fractal dimension of $D_\mathrm{F} = 1.76 \pm 0.03$. However, the fractal dimension distribution of smaller islands scatters very strongly in the range from $D_\mathrm{F} = 1.353$ to $D_\mathrm{F} = 1.772$. The fact that larger islands show a constant behavior indicates that the island formation follows the same mechanism. The small islands, however, do not fit this frame.

In *Fig.* 15e) three cut image sections from the same overview image (*Fig.* 14a)) are given showing a series of islands with decreasing fractal dimensions D_F. i) and ii) show larger islands. In comparison of i) and ii) a correlation between lower values of D_F and a more fractal appearance of the islands can be seen. *Fig.* 15e) iii) displays an island which is approximately one fifth of the size of the previous ones. This island is noticeably pixelated. The center part of the island is the highest area region and framed in red.

By cutting off the islands boundary areas of lower height, such as executed by the flooding function for heights lower than the threshold “minimum apparent height” of 150 pm the outer fringes of islands are not considered in the fractal analysis. The considered part of the island in *Fig.* 15e) iii) is therefore approximately line shaped. On the overview images of the same scan area, smaller islands have a higher area fraction per pixel ratio. Therefore, the determined shape of a smaller islands is stronger affected to changes by the binary filter in the height regime of the cutoff value. The high area fraction per pixel ratio explains the huge scattering of the fractal dimensions of the small island, since their analyzed shape is mainly created by the pixel selection of the binary filter. Almost line-shaped islands have particularly small fractal dimensions. The fact that small islands are often interpreted as a line (such as *Fig.* 15e) iii) running along the scan direction suggests that the small islands additionally interact with the tip and mirror the scanning process. The small islands are hence regarded authentic neither in their unfiltered shape (due to tip interactions) nor in their fractal dimension (due to an increasing shape determining influence of the image pixels with smaller shape size). The rather uniform distribution of islands of bigger extend is regarded as authentic, since the perimeter per area ratio is much smaller and the shape dictating impact of single pixels is reduced. Further explanation of tip interaction giving raise to approximately line shaped appearances along the scanning direction is given in *Sec.* 3.7.4.

3.4 DAF Adsorption Structures

DAF is observed in different adsorption structures. It can be distinguished between different structures depending on the adsoption temperature but also depending on different regions on the same sample. The DAF deposited on pristine Ag(100) at 45 K adsorbs in clusters (see *Fig.* 16).

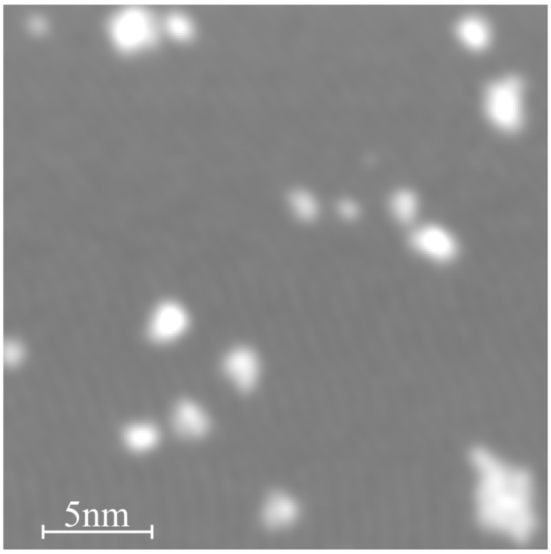

Figure 16: DAF on Ag(100) deposited at 45 K; tunneling parameters: $I_\mathrm{t} = 8\,\mathrm{pA}$, $V_\mathrm{t} = 100\,\mathrm{mV}$

The clusters show a coverage below 15% of the total area and have sizes from $0.3\,\mathrm{nm}^2$ to $21.5\,\mathrm{nm}^2$. They do not show long-range order. From this, it is concluded that DAF is mobile enough to agglomerate at 45 K. Since these molecular islands are of low structural order, the islands are likely to be kinetically limited structures. In reference to DAF adsorption studies on Ag(111) [5], it is supposed that they only transform into ordered structures by annealing the sample at higher temperatures. Therefore, another preparation is carried out at an increased deposition temperature of 53 K.

At a deposition temperature of 53 K, single molecules are observed alongside with smaller agglomerates. Within this chapter, the different DAF species are discussed individually. The first section of this chapter focuses on the single molecules and the second chapter on the agglomerates. The tip induced cleavage product of individual molecules is observed as surface bound carbene, as discussed in the third chapter. Beyond clusters, DAF molecules are found as monomers as well as dimers. The two species occur on different, clearly distinguishably sample regions. The dimers are discussed in the fourth section.

3.4.1 DAF Monomers on Ag(100)

Elliptically shaped protrusions, which seem slightly double-dumbbell shaped in some instances, are observed after the DAF deposition at 53 K subsequent to the Xe deposition. A STM image of this species is shown in *Fig.* 17a). An example protrusion is marked by the red box and is labeled as DAF_1. The index refers to the observation that this species is represented by a single protrusion.

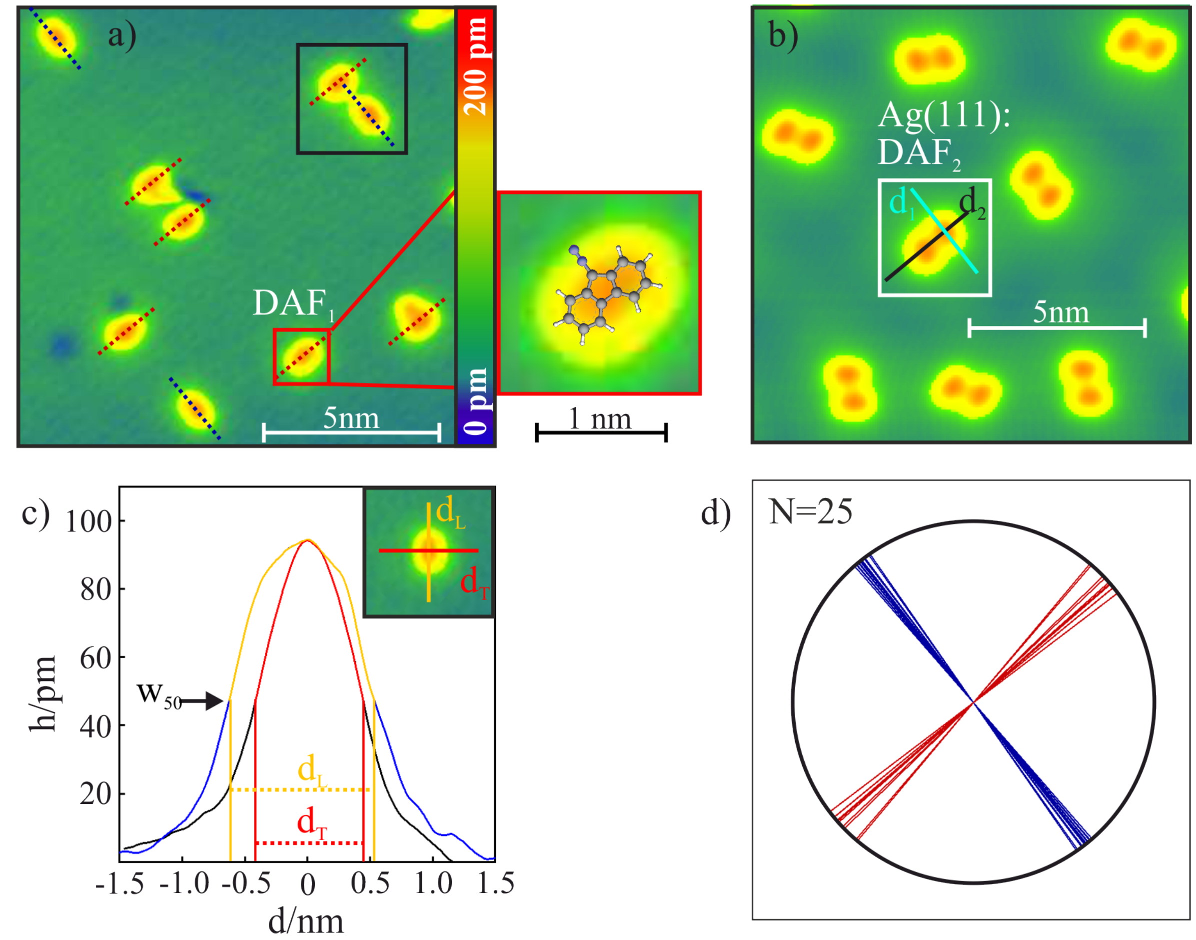

Figure 17: Adsorption structure of DAF on Ag; a) STM image of DAF on Ag(100); $T_{\mathrm{dep}} = 53\,\mathrm{K}$, orientation indicated by dotted lines in colors according to (d), true to scale superposition of the monomer DAF DFT model on protrusion in red box on the right; b) DAF dimers with assignment of axes; all STM images in pseudo-color, tunneling parameters: a) I_{t}=66 pA, V_{t}=507 mV; b) I_{t}=8 pA, V_{t}=100 mV; c) Height profiles of DAF_1 along axes outlined in the left top image; w_{50} marked; d) Polar diagram of the orientation of the longitudinal axes of DAF_1.

The ellipses are found on bare sample regions such as free Ag(100) terraces and in interspaces between Xe islands. The observations of single ellipses differ from the observations of DAF on Ag(111). On Ag(111) double protrusions were observed and assigned to DAF dimers [5]. Dimer molecules from these previous studies by K. Lucht are depicted in *Fig.* 17b) for comparison. An example dimer is labeled as DAF_2. The index refers to the number of two parallel ellipses that constitute the STM image of a dimer. The observation that DAF on Ag(100), unlike on Ag(111), is represented by a single protrusion instead of a double protrusion suggests a monomer assignment of the present species. The identification of the present species is further examined by comparison of its spatial dimensions to the DFT model as well as to the dimensions of the dimer on Ag(100). The spatial dimensions are determined from height profiles along the longitudinal axis d_L (outlined as orange line) and the transversal axis d_T (outlined as red line) of the ellipse as shown in *Fig.* 17c).

For a consistent exclusion of tip convolution effects, only the top half of the height of a line scan is considered for width calculations. The resulting width is referred to as 50% width (w_{50}) in the following. The w_{50} of the present species is compared to the known DAF dimer on Ag(111) [5]. Both species are studied analogously according to the measurement approach described. The measures of both DAF species on different Ag surfaces are determined and listed for comparison in *Tab.* 7. The direct width relation of the different DAF-species on both Ag substrates, however, given in this chapter must be regarded critically, since different tunneling parameters were applied for both studies. Just a rough comparison of the shapes and sizes of both species can be given. DAF on Ag(100) is measured at higher tunneling voltages than DAF on Ag(111). Since a relative increase in the apparent height is therefore expected for Ag(100) [5,36,37], no heights can be compared. For the distortions in the ratios of the widths, it is assumed that the width of DAF on Ag(100) is overestimated compared to DAF on Ag(111).

Table 7: Spatial measures of DAF on Ag(100) compared to Ag(111) in *pm*

diameter of species substrate	$d_\mathrm{L}(\mathrm{DAF}_1)$ Ag(100)	$d_1(\mathrm{DAF}_2)$ Ag(111)	$d_\mathrm{T}(\mathrm{DAF}_1)$ Ag(100)	$d_2(\mathrm{DAF}_2)$ Ag(111)
w_{50}	1200 ± 114	1238 ± 24[†]	874 ± 46	1891 ± 84[†]

The w_{50}-diameter along the longitudinal axis of the ellipse of DAF on Ag(100) is determined to be $d_L = (1200 \pm 114)\,\mathrm{pm}$. This is larger than the outermost H-distance of the fluorene-skeleton in the DFT-model of 910 pm (c.f. *Sec.* 2.2.3) but much smaller than the w_{50} of the dimer through both protrusions of $d_2(\mathrm{DAF}_2) = (1891 \pm 84)\,\mathrm{pm}$. The

---

[†] Evaluated in this work from the data measured by K. Lucht

w_{50}-diameter along the traversal axis of $\mathrm{DAF_T}$ of $d_L = (874 \pm 46)\,\mathrm{pm}$ is slightly smaller than half of $d_2(\mathrm{DAF_2})$. The monomer fraction of the dimers has a 50%-width along the perpendicular axis to d_2 through a single ellipse center of $d_1(\mathrm{DAF_2}) = (1238 \pm 24)\,\mathrm{pm}$. The width of a single molecule within the dimer is hence similar to the width of the ellipse measured on Ag(100) and the length of the dimer d_2 is about twice as long as the transversal diameter of the ellipse. The species recorded on Ag(100) are thus assigned to monomers.

The monomer DFT model is superimposed to the magnification of the ellipse within the white frame in *Fig.* 17a) in the sub-figure aside. The average maximum height of $\mathrm{DAF_1}$ (corresponding to the tunneling parameters of *Fig.* 17a)) is determined to be $(94 \pm 4)\,\mathrm{pm}$. *Fig.* 17d) shows the polar diagram of the monomer orientations. The monomers are uniformly oriented in an orthogonal fashion. The occurrence of a strict monomer alignment to the substrate surface can be ascribed to the higher corrugation of the Ag(100) sample compared to Ag(111). The energy gain by the occupation of the ideal adsorption structure is concluded to predominate the one of possible H-bond formations on the present sample. Separate monomers (e.g. molecule in the red box of *Fig.* 17a)) show the same orientation as molecules directly adjacent to other molecules of the same species (e.g. molecules in the black box of *Fig.* 17a)). Hence, the rotational orientation of individual molecules is not affected by interactions with other molecules of the same kind.

These observations contrast those on Ag(111), where DAF is found to form dimers due to hydrogen bonds (H-bonds) at a deposition temperature of $(85 \pm 3)\,\mathrm{K}$. Another differing characteristic present is noticed compared to the case on Ag(111): this difference is that no tip-induced rotation is seen with the chosen tunnel parameters of *Fig.* 17a) ($I_\mathrm{t} = 66\,\mathrm{pA}$, $V_\mathrm{t} = 507\,\mathrm{mV}$). For comparable imaging parameters, monomers on Ag(111) such as removed from the dimers through targeted manipulations are easily excited by the tip to rotate. Such rotations set in already at mild parameters such as $I_\mathrm{t} = 8\,\mathrm{pA}$, $V_\mathrm{t} = 50\,\mathrm{mV}$ [5]. The absence of such a rotation is interpreted as another evidence of a much stronger substrate-adsorbate-interaction in the case of Ag(100).

The orthogonal fashion of molecular orientation presented here leads to the conclusion that the DAF is aligned to high symmetry directions of the Ag(100). This is the only plausible alignment, since the molecular orientation as seen in the polar diagram (*Fig.* 17d)) matches the related fourfold symmetry. Any other conceivable alignment must have an additional mirror plane along the high symmetry directions and would hence double the number of signals in the polar diagram. However, the determined DAF orientations in *Fig.* 17d) is not congruent with the previously determined orientation of the Ag unit vectors. The angle between the two mean DAF orientations and the primitive Ag(100) unit vectors (as determined in *Sec.* 3.1 based on *Fig.* 6a)) is about 20°. It is therefore concluded here that the Ag(100) crystal experienced an rotation on the sample holder in the time interval between the study of exclusive Xe adsorption and the present study of DAF coadsorption. The sample fixation on the sample holder turns out to be unstable and the previously presented Ag lattice orientation cannot be transferred to the currently presented measurement series. The true substrate orientation is revealed by the molecular orientations. This conclusion is affirmed by the congruent orientation of the pseudo atomic image as shown in *Sec.* 3.1 *Fig.* 6b). DAF adsorption sites are studied in the following section for further affirmation.

3.4.2 DAF Agglomerates and Adsorption Sites Analysis

DAF monomers introduced in the previous chapter are observed alongside with agglomerates. DAF agglomerate islands are shown in *Fig.* 18.

The number of molecules within the agglomerates varies between 2 and 20 molecules. The average DAF coverage is (0.06 ± 0.02)molecules/nm^2. As the coverage is determined from the analysis of several images in which a cluster is either observed or not observed, the resulting error is relatively high.

It can be concluded that at the deposition temperature of 53 K, DAF has enough kinetic energy for cluster formation. At this temperature, however, monomers start separating from clusters, moving freely. The agglomerates are studies this chapter.

These agglomerates show no long-range ordered structures. Single DAF molecules are recognized as elliptical subunits in the agglomerate. The near-order structure of these agglomerates is dominated by molecular alignment to the substrate as observed in the monomer case, indicated by dotted lines. An average of $(55 \pm 5)\%$ of the ellipses within the agglomerates are oriented along the preferential perpendicular directions presented for the monomers in *Fig.* 17. The dotted red and blue lines in the STM images of *Fig.* 18 mark the molecular orientations, drawn analogously to those from *Fig.* 17.

Frequently, mutually perpendicular molecules are observed. Due to the molecular symmetry, no double H-bonds (as known from Ag(111)) can be formed in this arrangement. Nevertheless, the direct vicinity to other molecules does not dictate any change in orientation.

The influence of the substrate on the molecular orientation in the agglomerate plays the dominant role. The orientation of molecules close to neighbors is not changed by any interaction and corresponds to the monomer orientation. In order to clearly identify the molecular alignment to the substrate and evaluate accessible adsorption sites for DAF on Ag(100), a series of images is recorded to compare the agglomerate before and after a scan with mobilizing tunneling parameters. *Fig.* 18a) shows the onset configuration of an agglomerate. The drawn triangle serves only for orientation purposes. Subsequent to

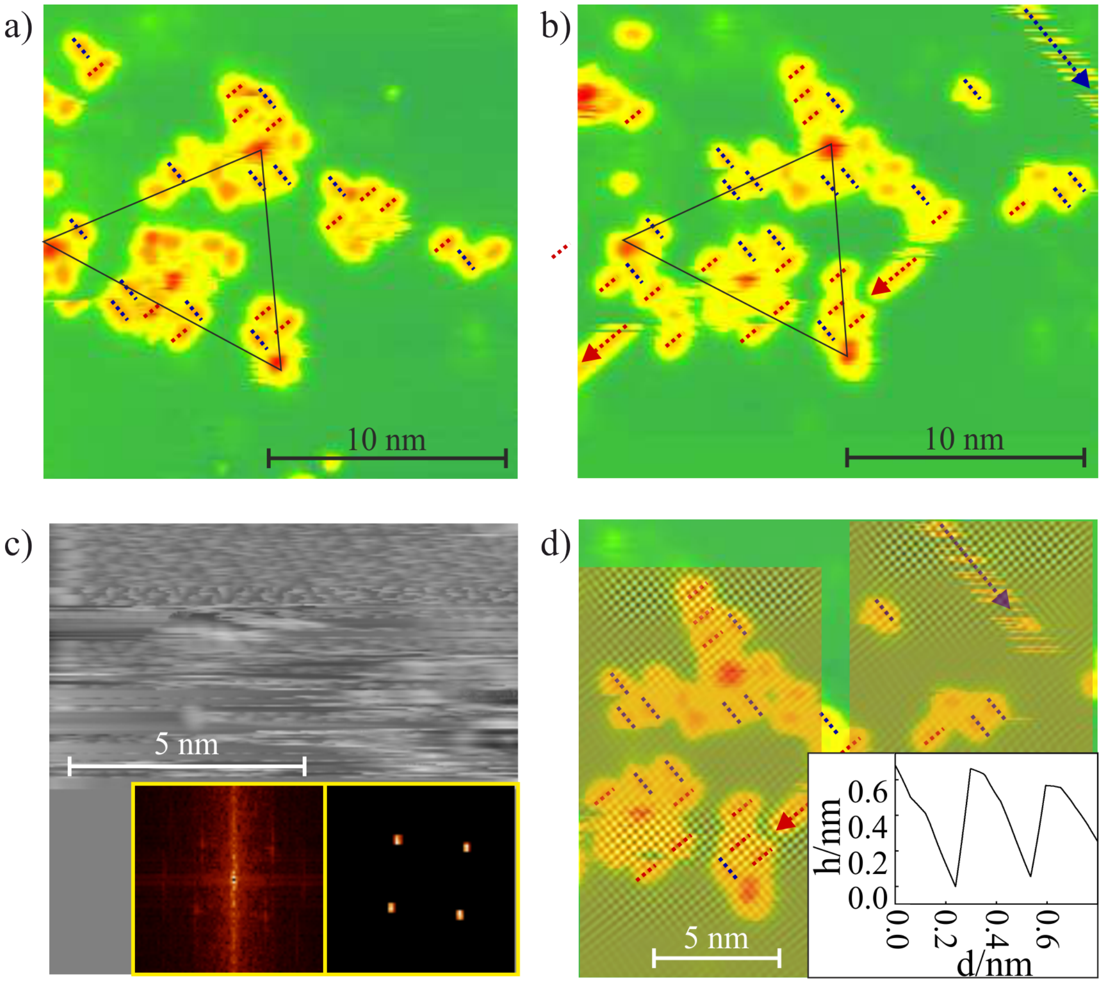

Figure 18: DAF agglomerate on Ag(100), $T_{\text{dep}} = 53\,\text{K}$; STM-images: a) Initial molecular positions, orientation indicated by dotted lines in colors according to *Fig.* 17, triangles: reference points; b) Molecular positions after manipulation, arrows: molecule displacement direction; c) Image during sliding manipulation, insertions: FT-Spectrum and filtered signals; d) True to scale superposition of the region shown in (b) with grid gained from reverse FT of (c), insertion: Height profile of a pushing trace parallel to the blue arrow direction, but measured in another image; (a), (b), (d) in pseudo-color, tunneling parameters: a) I_{t}=8.1 pA, V_{t}=−1 V; b) and d) I_{t}=8.5 pA, V_{t}=−1 mV; c) I_{t}=0.61 nA, V_{t}=−51 mV.

this image, an image with highly system-interfering parameters of a low tip-sample distance (I_{t}=0.61 nA, V_{t}=−51 mV) is taken at the same location as shown in *Fig.* 18c). The tip displaces a molecule along the available adsorption sites. Thus, an image of pseudo atomic resolution is obtained. A reverse FT is applied to the resulting quadratic pattern such as described in *Sec.* 3.2.3. The spectrum and the filtered signals are inserted below the STM image of *Fig.* 18c). The obtained pattern by reverse FT is quadratic and has a related point distance of (313 ± 6) pm, which lies within the scope of error of the Ag-atom distance of the images discussed in *Sec.* 3.1. The grid, hence, corresponds to the periodicity of the Ag(100) surface and has a parallel orientation to the DAF molecules. This is illustrated in *Fig.* 18d) by the superposition of the FT grid to the imaged DAF molecules from *Fig.* 18b). This figure shows the same region recorded with parameters close to the initial ones. Vertical displacement traces of molecules (for a more detailed descriptions of conceivable mechanisms see *Sec.* 3.7.1) are indicated by dotted arrows. The reverse FT grid, as shown in *Fig.* 18d), is congruent to the marked monomer orientations as well as to the majority of molecules within the agglomerate. It is furthermore congruent to the vertical displacement traces of molecules along the paths of the arrows.

The FT-grid provides information about the orientation and the periodicity of the available adsorption sites. It is proved that DAF molecules occupy adsorption sites along the primitive unit vectors of the Ag(100) direction with the periodicity of the primitive lattice parameter d_{Ag}. This is confirmed by the height profile from a pushing trace as depicted in the inserted box in *Fig.* 17d), which also agrees to the periodicity of Ag(100) and is oriented parallel to the molecules. The orientation of the DAF molecules along the primitive lattice vectors of Ag(100) can thus be detected by various methods despite the lack of a reference lattice. An exact assignment of the adsorption sites to on-top or hollow sites, however, cannot be drawn from the overlay of different images such as a-d) due to effects like creep and drift. The positioning of the superimposed grid on the adsorbates is chosen arbitrarily. On this sample region the local substrate of the DAF molecules is unmistakably identified as Ag(100), due to the periodicity and the quadratic symmetry. An underlying Xe layer is not conceivable for this sample region.

Despite the strong tunneling voltages ($\approx -1.2\,\mathrm{V}$) applied in *Fig.* 17a) and b) and the highly interacting low tunneling resistance of *Fig.* 17c), only a minor rearrangement of the molecules is observed. After the rearrangement, within the imaged area the fraction of molecules that are aligned to the surface increases locally from about 69% to 75%. Re-orientation of disordered molecules into an ordered state is observed in the middle of the triangle, whereas a fraction of molecules at the top triangle edge loses their order.

This indicates once more a much stronger fixation of the DAF on the substrate than in the case of Ag(111). On Ag(111), dimer separation into single molecules is found to set in at comparable tunneling currents (I_{t}=8 pA) but lower voltages (UI_{t}=500 mV). The resulting rotations of single molecules such as on Ag(111) cannot be observed in the areas examined in this chapter.

3.4.3 Tip Induced DAF Cleavage

Fig. 19a) shows a sample region close to a previous tip-forming location. In this area another species is found.

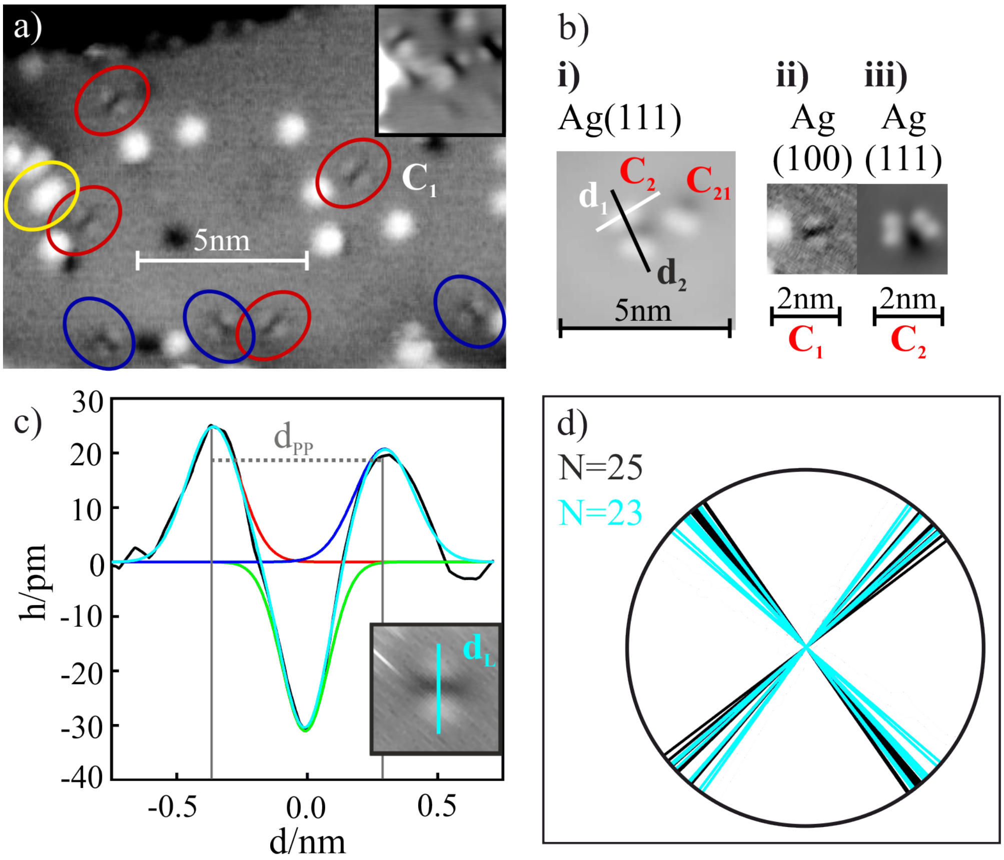

Figure 19: DAF cleavage products on Ag with (a), (c), (d): Tip induced, on Ag(100), $T_{\mathrm{dep}} = 53\,\mathrm{K}$; b) Comparison to known carbene species on Ag(111); a) STM-image: derivatives obtained after tip forming marked by circles, alignment indication in color coding to analog *Fig.* 17(a), yellow circle: DAF monomer, double low pass function applied; inserted box: image of cleaved DAF monomers in a lateral distance of $\approx 1\,\mathrm{nm}$ b) Different surface bound DAF derivatives: i) tip induced cleavage product on Ag(111), $T_{\mathrm{dep}} = 85\,\mathrm{K}$; ii) tip induced cleavage product (C_1 from (a)) on Ag(100); iii) laser induced cleavage product on Ag(111); All images in (a) & (b) in same lateral scale, tunneling parameters: (a) $I_{\mathrm{t}} = 8.3\,\mathrm{pA}$, $V_{\mathrm{t}} = 126\,\mathrm{mV}$, box: $I_{\mathrm{t}} = 8.5\,\mathrm{pA}$, $V_{\mathrm{t}} = -1\,\mathrm{V}$; (b): (i) & (ii) $I_{\mathrm{t}} = 8.5\,\mathrm{pA}$, $V_{\mathrm{t}} = 100\,\mathrm{mV}$; (iii) $I_{\mathrm{t}} = 8.0\,\mathrm{nA}$, $V_{\mathrm{t}} = 100\,\mathrm{mV}$; c) Height profiles with Gauss fit along d_{L} outlined in the right bottom image (height profile: black, cumulated fit: cyan, partial fits: other, grey: peak to peak distance d_{PP}); d) Polar diagram of the carbene orientation of the longitudinal axis with reference to Ag crystal directions in cyan, monomer orientation as reference in the background in black

This species, marked by the elliptical frames in *Fig.* 19c), has a butterfly-like shape of a narrow depression between two small, opposed elevations. For better distinction, the species is labeled C_1. The corresponding height profile of the line scan along the longitudinal axis d_L across the elevations is shown *Fig.* 19c). The average peak to peak distance of outermost peaks from the applied Gaussian fits is (678 ± 76) pm and the mean maximum apparent height is (20 ± 4) pm. This apparent height is largely reduced compared to the height determined for DAF_1 of (94 ± 4) pm. The depression has an approximate minimum apparent depth of (-26 ± 5) pm relative to the surface. The 50%-width along the longitudinal axis of the butterfly shaped species is determined to be $d_\mathrm{L} = (968 \pm 49)$ pm. This is slightly larger than the outermost H-atom distance of the fluorene-skeleton of the DFT-model of 910 pm (see. *Sec.* 2.2.3) and smaller than the longitudinal diameter of the DAF_1 monomer of $d_\mathrm{L}(\mathrm{DAF}_1) = (1200 \pm 114)$ pm.

The presented species strongly resembles the appearances known from the products of laser-induced, as well as tip-induced, cleavage of DAF on Ag(111) as recorded by K. Lucht. The appearance of a new depression strongly suggest the formation of a surface-bound carbene species, which leads to local electron depletion of the metal. For the identification of the present species, its measures are compared to those from the carbenes on Ag(111). An image sequence of all DAF-carbene species observed in both studies is given in *Fig.* 19b) and labeled for reference. Note that the used tunneling parameters are comparable but not identical.

On Ag(111), cleaved DAF is found as single carbenes. These carbenes are observed either in opposed pairing, corresponding to the configuration of the H-bond reactant dimers (see C_2) or separately (see $C_{2,1}$) [5]. Both configurations are seen in *Fig.* 19b-i). Due to the facing symmetry of the paired DAF molecules within the dimer, the corresponding paired carbenes C_2 are in a butterfly-like shape. The C_2 resembles the symmetry of the present species C_1 in *Fig.* 19b-ii) on Ag(100) on first sight. This applies explicitly not for the separate monomer carbene on Ag(111) $C_{2,1}$, which has no two-fold symmetry. However, both elevations of C_2 are more elongated than those of C_1 and noticeably V-shaped tilted apart. C_1 is furthermore distinguishable from the dimer configuration since the average peak to peak distance of $d_\mathrm{L}(C_1) = (678 \pm 76)$ pm as depicted in *Fig.* 19c) is smaller than 1 nm. This was discovered to be the approach limiting distance for targeted manipulative pairing of monomer carbenes on Ag(111) in [5]. The longitudinal w_{50} diameter of C_1 ($d_\mathrm{L}(C_1) = (968 \pm 49)$pm) resembles the diameter of a single protrusion within C_2 of $d_1(C_2) = (935 \pm 73)$pm. Dimensional measures of all species discussed here are listed for better comparability in *Tab.* 8.

C_1 is, hence, similar to a single protrusion, i.e. one half of C_2. This suggest a monomer assignment. The image of single carbene molecules on Ag(111), furthermore, shows a subdivision into two double-dumbbell shaped protrusions according to *Fig.* 19b-iii), if recorded with an enhanced tip. These opposed double-dumbbell shaped protrusions are concluded to correspond to the two protrusions of C_1 on Ag(100).

The polar diagram of the orientations of C_1 on Ag(100) is shown in *Fig.* 19d). The cyan lines which represent the orientation of the butterfly-like species are superimposed to the black lines of the previously determined monomer orientations. The orientations of present species are orthogonal and match the alignment of the monomers along the closed packed Ag directions.

The species mapped here is hence assigned to the tip-induced cleavage products of DAF monomers. These surface bound carbenes are generated due to the non-characterized current pulse of the tip forming. The species is observed several times together with DAF monomers.

Regarding the STM image of $C_{2,1}$, the twofold symmetry of the present species is unexpected for a monomer. C_1 differs from $C_{2,1}$ in the fundamental aspect that the depression is located in the midst of both elevations. A single carbene $C_{2,1}$ on Ag(111) is pictured as a double dumbbell with an adjacent, parallel depression. Assuming that the double-dumbbell elevation represents an image of up-tilted phenyl rings, an offset of the depression may indicate a different bond angle towards the surface. Theoretical calculations consider the metal carbene angle to be dependent on the carbene-spin state, given in [5]. This raises further questions about the difference in the bonding situation on Ag(100) compared to Ag(111), which exceed the scope of this work, but provides an interesting perspective for following studies.

The surface bound carbenes are found at very close distances, seen in the inserted box in the top of *Fig.* 19a) (d =1 nm to 1.5 nm) under the absence of any reaction among them. Like on Ag(111), the bond to the surface seems to be preferred over bond formation to species of the same kind.

Table 8: Spatial measures of tip-induced cleavage product of DAF on Ag(100) compared to Ag(111) in pm^{-1}

species substrate	$d_{\mathrm{L}}(C_1)$ Ag(100)	$d_1(C_2)$ Ag(111)	$d_{\mathrm{L}}(\mathrm{DAF}_1)$ Ag(100)	$d_2(C_2)$ Ag(111)
w_{50}	968 ± 49	$935 \pm 73^{\dagger}$	1200 ± 114	–
peak-distance	641 ± 18	–	–	> 1000 [5]

3.4.4 DAF Dimers

On a different sample region of the same preparation of the DAF deposition (subsequent to Xe at 53 K, which is the foundation of all previous parts of this chapter) a completely

---

† Evaluated in this work from the data measured by K. Lucht

different adsorption structure of DAF is found. *Fig.* 20a) shows the occurrence of elliptical double protrusions (marked by white circles) located at a lower terrace next to a step (bottom right).

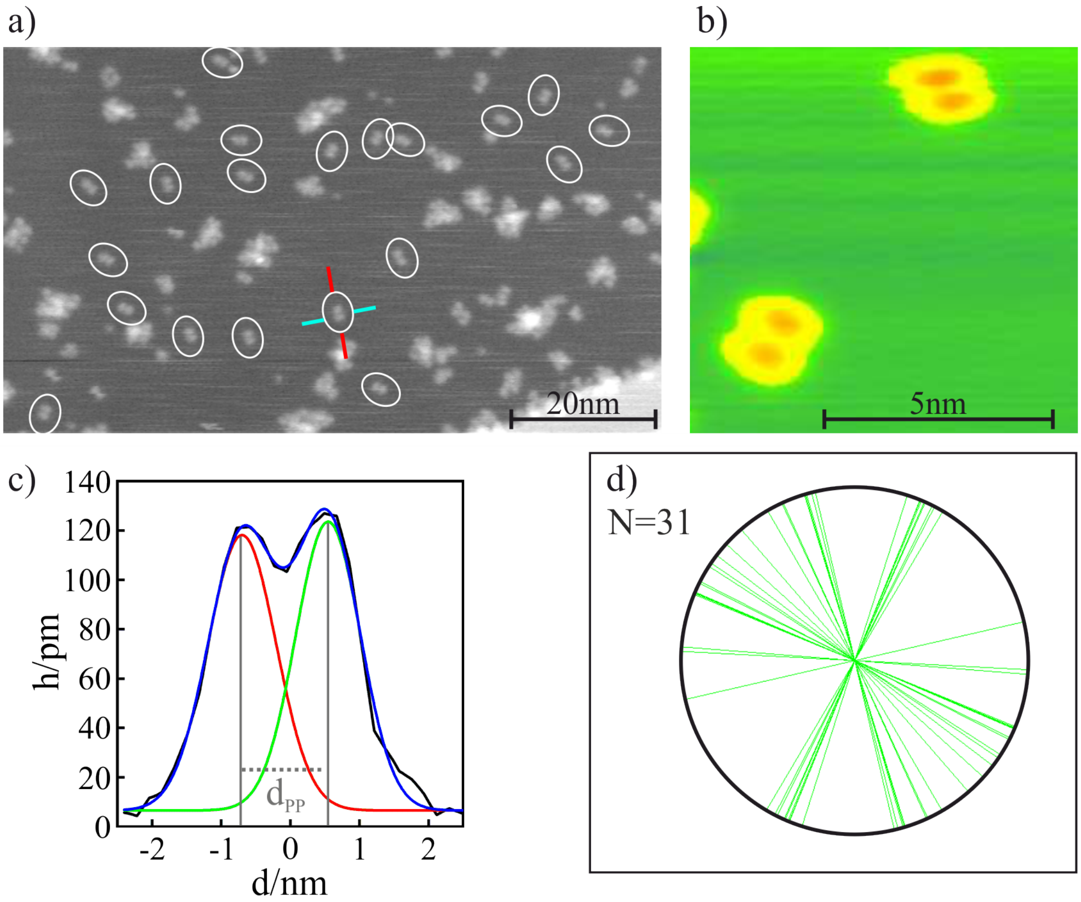

Figure 20: DAF dimers consecutively deposited on Ag(100) after Xe at 53 K; a) Overview STM-image: double ellipses circled in white, axis marked: d_2 in red, d_1 in cyan, tunneling parameters: $I_t = 8.1\,\text{pA}$, $V_t = 131\,\text{mV}$; b) close up STM-image: double ellipses, tunneling parameters: $I_t = 150\,\text{pA}$, $V_t = 259\,\text{mV}$; c) Height profile along d_2 (red and green: Gaussian fits, grey: peak to peak distance d_{PP}); d) Polar diagram: alignment of the line across both centers of the double protrusion

These double protrusions are located in the vicinity of irregularly shaped agglomerate islands of the same apparent height of about 120 pm. Some of these islands show further elevations up to about 300 pm in their center, which cannot clearly be assigned to tip interactions or real elevations and are not further discussed here.

The discussed protrusions consist of a pair of ellipses that face each other with a slight offset relative to their center. *Fig.* 20b) shows a close-up image of the double ellipses. The height profile along the longitudinal axis across the centers of both ellipses (d_2, indicated by red line in a) is shown in *Fig.* 20c). The average peak to peak distance from the Gauss fit of these double protrusions is determined to be (1110 ± 81) pm as depicted in *Fig.* 20c). Since the double ellipse shape strongly resembles the dimers observed on Ag(111) their 50% widths are compared. The w_{50} diameter of the longitudinal axis across both ellipses on Ag(100) is $d_2 = (2119 \pm 178)\,\mathrm{pm}$. This is slightly bigger but comparable to the w_{50} diameter of the long axis of a DAF dimer on Ag(111) of $d_2 = (1891 \pm 84)\,\mathrm{pm}$. The 50% width along the perpendicular axis to the long axis (through the long axis of a single ellipse indicated in cyan) is determined to be $d_1(1447 \pm 92)\,\mathrm{pm}$ for the double ellipses on Ag(100). This is also comparable to the 50% width along the perpendicular axis of the DAF dimer on Ag(111) of $d_1 = (1238 \pm 24)\,\mathrm{pm}$. The image on Ag(100) is therefore slightly bigger than the one on Ag(111) but the proportions are maintained. It is to be noted that the width determination is based on images measured with nearly similar but not identical tunneling parameters, which may cause a slight systematic overestimation of the species on Ag(100) in comparison to the species imaged on Ag(111) (tunneling parameters: Ag(100): $I_\mathrm{t} = 8.1\,\mathrm{pA}$, $UI_\mathrm{t} = 131\,\mathrm{mV}$; Ag(111): $I_\mathrm{t} = 8.0\,\mathrm{pA}$, $UI_\mathrm{t} = 100\,\mathrm{mV}$). Due to the similarity to the dimer on Ag(111) and the measures that fit the DFT molecule model twice, these double protrusions are referred to as dimer hereafter.

Table 9: Spatial measures of DAF-dimer adsorbed consecutively after Xe on Ag(100) and DAF dimers on Ag(111) in pm^{-1}

species substrate	$d_2(\mathrm{DAF}_2)$ Ag(100)	$d_1(\mathrm{DAF}_2)$ Ag(100)	$d_T(\mathrm{DAF}_1)$ Ag(100)	$d_2(\mathrm{DAF}_2)$ Ag(111)	$d_1(\mathrm{DAF}_2)$ Ag(111)
w_{50}	2119 ± 178	1447 ± 92	874 ± 46	$1891 \pm 84^\dagger$	$1238 \pm 24^\dagger$
peak-distance	1110 ± 81	–	–	–	–

The polar diagram of the alignment of the dimers can be seen in *Fig.* 20d).

Unlike the monomer, the orientation distribution of the dimer adsorption structure in the polar diagram is not of a four-fold symmetry. The dimers shows a partial bundling of orientations, but with strong scattering. Due to the low data set available, no precise and reliable alignment assignment to the substrate can be given at this point.

The dimers seen in *Fig.* 20b) reveal a slight shift of the center of the ellipses. However, a greater number of images of improved resolution is needed in order to evaluate the precise dimer symmetry. The case of relatively shifted center positions, would result in chirality by definition, which is a know phenomenon for DAF dimers [5]. Distinguishable enantiomer orientations may partially explain the increased scattering in the dimer case but it cannot explain the non-uniform orientations beyond bundles.

The non-uniformity is a fundamental difference from the monomer case. Since the Ag[1 0 0]

[†] Evaluated in this work from the data measured by K. Lucht

and Ag[0 1 0] axes have equal symmetric properties and are therefore congruent, the rotational behavior of the dimers does not fit the Ag(100) lattice symmetry. These observations seem more plausible under the assumption that DAF is adsorbed on the Xe film in the dimer case. A discrimination between two different substrates may explain the two different pairings and orientation symmetries.

This assumption implies that, in the case of Xe, the dimerization energy outweighs the monomer's energy gain by occupying the preferred adsorption site.

It is also noticeable that the substrate surface is continuously represented as rough pattern of horizontal lines. The occurrence of such lines is attributed according to *Sec.* 3.7 to the easy manipulability of Xe.

Hence, the contrasting behavior of DAF on the present sample region, characterized in *Fig.* 20a)–c), to the region discussed previously, delivers indications that the DAF may be measured on top of a Xe layer here. This assumption is regarded as very vague and is discussed further in *Sec.* 3.7.5. The observation that the dimers can be imaged in a stable way at tunneling currents of up to 150 pA while applying tunneling voltages of 260 mV (i.e. energies of 260 meV) may indicate that the individual protrusions are bound by chemical bonds rather than H-bonds. This assumption is also discussed in *Sec.* 3.7.5.

3.5 Coadsorption of DAF and Xe on Ag(100) at 63K

The subsequent deposition of DAF at 63 K onto prior deposited Xe results in clustered islands of varying shape and size and non-uniform height distribution. These islands are presumably composed out of a mixture of both species, since no separate species can be identified. An image of these islands is seen in *Fig.* 21a).

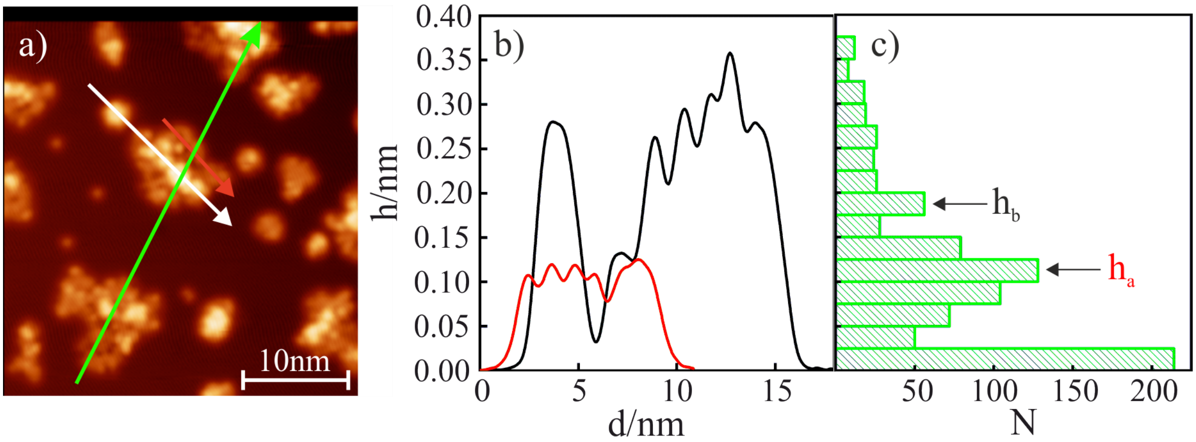

Figure 21: Islands obtained after DAF deposition at 63 K on Xe on Ag(100); a) STM image, tunneling parameters: $I_t = 7.3\,\text{pA}$, $V_t = 111\,\text{mV}$; b) Height profile along red and white arrow in (a) plotted in red and black; c) Height histogram of line scan along green arrow in (a) with the same height scale as (b)

The height profiles along the paths of the respective color in *Fig.* 21a) are seen in *Fig.* 21b). The height profiles show a rough course and no uniform island surface height can be identified. However, the islands seem to be composed of a consistent main bottom level which corresponds to the height h_{a} of about 100 pm as pointed out in the histogram and is represented by the red line scan. Another preferred height level is represented by the second peak indicated in the histogram as h_{b} at 175 pm. Above this height h_{b} varying heights are measured up to a maximum of 370 pm. The inhomogeneity may be attributed to an amorphous structure or unstable interactions with the STM tip.

The subdivision of height regimes of these islands is investigated applying the flooding function of WsXM. The image shown in *Fig.* 21a) is covered with islands (greater than the chosen minimum height of 80 pm) by 27.5%. Considering the whole island area a fraction of 35.2% is determined to have a larger height than h_{b} of 175 pm. It is concluded that the rather high DAF deposition temperature promotes Xe as well as DAF motion, resulting in the formation of non-ordered inter species agglomerates.

Presumably, the increased occurrence of the apparent heights h_{a} and h_{b} are explained by the respective apparent height of the individual species.

No local assignment to Xe or DAF can be drawn here. Further experiments are carried out at lower DAF deposition temperature in order to reduce the mobility of both species.

3.6 Coadsorption of DAF and Xe on Ag(100) at 53K

The subsequent deposition of DAF at 53 K onto prior deposited Xe results in Xe islands with additional protrusions on top of the island (see *Fig.* 22). This kind of Xe island is observed close to step edges.

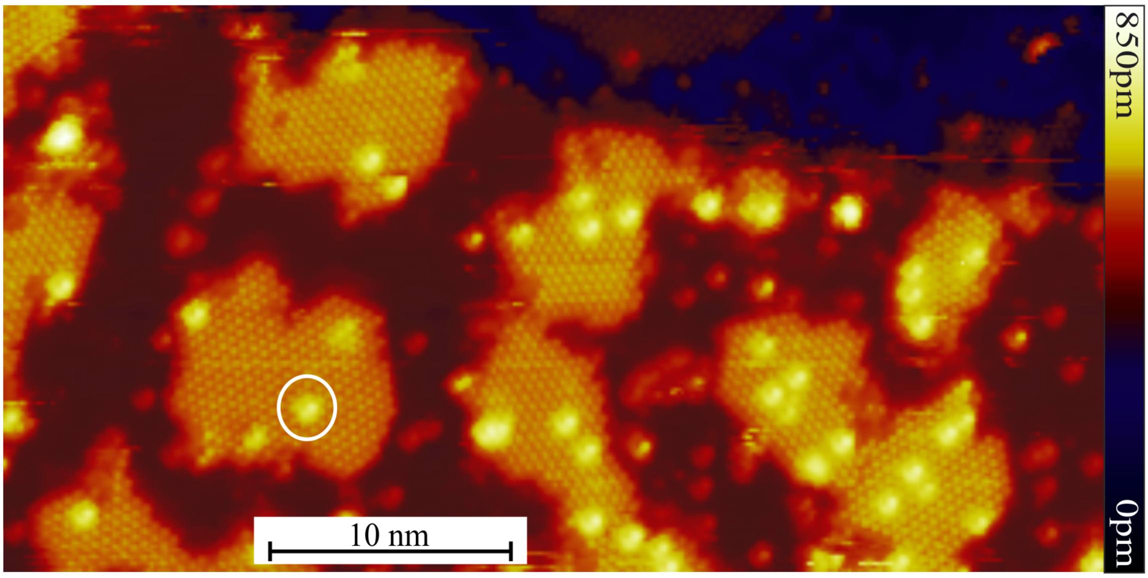

Figure 22: STM image of Xe island on Ag(100) next to a step edge (upper terrace: red, lower terrace: blue) with additional protrusion on top of the islands (example protrusion marked by white circle); the image is recorded with a double tip; tunneling parameters: $I_\mathrm{t} = 61\,\mathrm{pA}$, $V_\mathrm{t} = 516\,\mathrm{mV}$

In the first part of this chapter, the alignment of the Xe closed packed rows to the Ag(100) surface is examined. Subsequently, the influence of adsorbed DAF molecules on the orientation of the islands is studied. In the second part, the protrusion observed on top of the Xe islands are discussed under consideration of potentially adsorbed DAF on the Xe layer.

3.6.1 Rotational Pinning of Xe Islands by DAF on Ag(100)

Fig. 23a) shows the Xe islands from *Fig.* 22. The colored hexagons are superimposed for better overview of relative orientations. The grid represents the hexagonal Xe lattice such that atoms are located on vertexes and in the center of each hexagon.

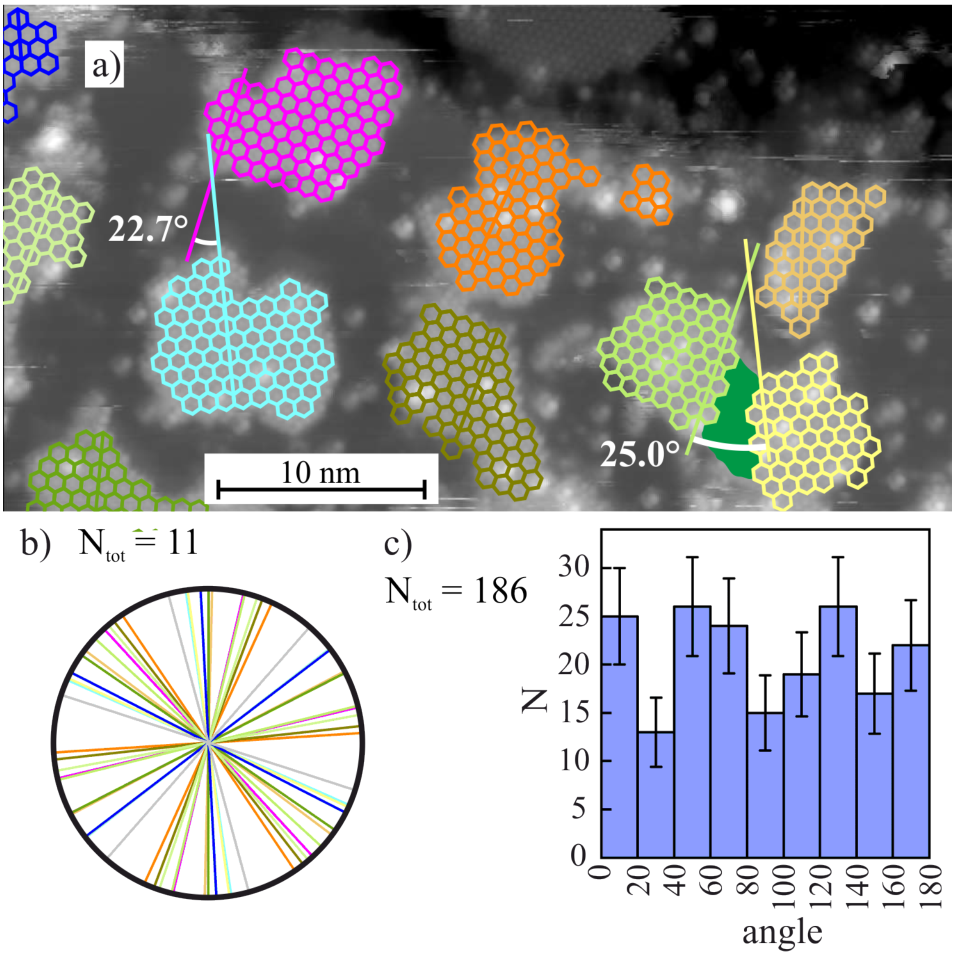

Figure 23: Rotational alignment of Xe islands after DAF-deposition on Ag(100) at an upper terrace next to a step; a) STM image according to *Fig.* 22 with hexagonal grid overlay (atomic positions on vertexes and centers of hexagons, compare *Fig.* 23), straight lines display the Xe closed packed rows of different domains, angles between domains are highlighted in white, the green area represents the boundary region between two domains (zoomed view in *Fig.* 25), tunneling parameters: $I_t = 61\,\mathrm{pA}$, $V_t = 516\,\mathrm{mV}$; b) Polar diagram of the mean orientation per closed packed row of the islands from (a) in the respective color-coding; c) Histogram of the angle distributions of the closed packed rows relative to STM image y-axis

The displayed islands have varying and non-repetitive orientations. The mean orientations for all three closed packed directions of the Xe per island are shown in the polar diagram *Fig.* 11b). The angle distribution histogram of absolute orientations is shown in *Fig.* 11c) with respect to the image y-axis. The histogram shows a wide array of gradual rotational symmetries, suggesting no clear orientation restrictions.

The angles between islands of different orientations are not compatible to any (six-fold or twelve-fold) rotation that could be expected for a hexagonal lattice due to its rotational symmetry. As an example, the angle between the steepest closed packed rows of the pink and cyan islands is displayed. This angle is determined to be 23°, using the angle measurement function of CorelDRAW. Xe islands with varying rotational orientations independent of the substrate were reported in low energy electron diffraction (LEED) studies for Ag(111) [32]. This effect was attributed to pre-adsorbates, which preferably adsorb on step edges, restricting the Xe orientation and position on growth.

This idea can be transferred to the present system. Most likely, the main species dominating the orientation in here is no pre-adsorbate but the DAF, which was added subsequent to the Xe. This is plausible considering the annealing of the sample during DAF deposition at temperatures at which both species Xe and DAF are expected to be mobile. A limited but nonetheless present DAF mobility at the adsorption temperature was already concluded from the observations of monomer alignment to the substrate as well as from agglomerate formation (see *Sec.* 3.4.2). In case of Xe, mobility allowing to reach nucleation cores such as step edges or other fixed adsorbates is expected down to very low temperatures. STM studies by Horch et al. reveal Xe mobility on Pt(111) down to 20 K [38]. Comparable mobility is expected for the present case on Ag(100), as Xe has generally low interactions with metal surfaces [24]. Accordingly, it is supposed that the adsorption structure of Xe is changed during the annealing process linked to the DAF deposition. Due to the mobility regain of Xe, the adsorbed DAF molecules on the pristine Ag surface regions may dictate and change the Xe adsorption geometry. This hypothesis is further supported by comparison to the Xe adsorption geometry without DAF coadsorption (see *Fig.* 11c)) for which several preferable directions in the angle distribution are observed. However, this is not observed for the case of coadsorption of Xe and DAF as presented in *Fig.* 23c). For a deeper insight into this effect, the interface between both species is investigated.

On that account, the sample region seen in *Fig.* 24a) is analyzed. This sample region is located close to the previously discussed region of *Fig.* 23a), but separated by several steps. The Xe islands of both images have the same apparent height of (202 ± 3) pm, indicating a Xe monolayer. Transferability among both images concerning species assignments and conclusions about the rotational behavior of the islands is thus plausible due to the close lateral proximity and the given similarity of both images.

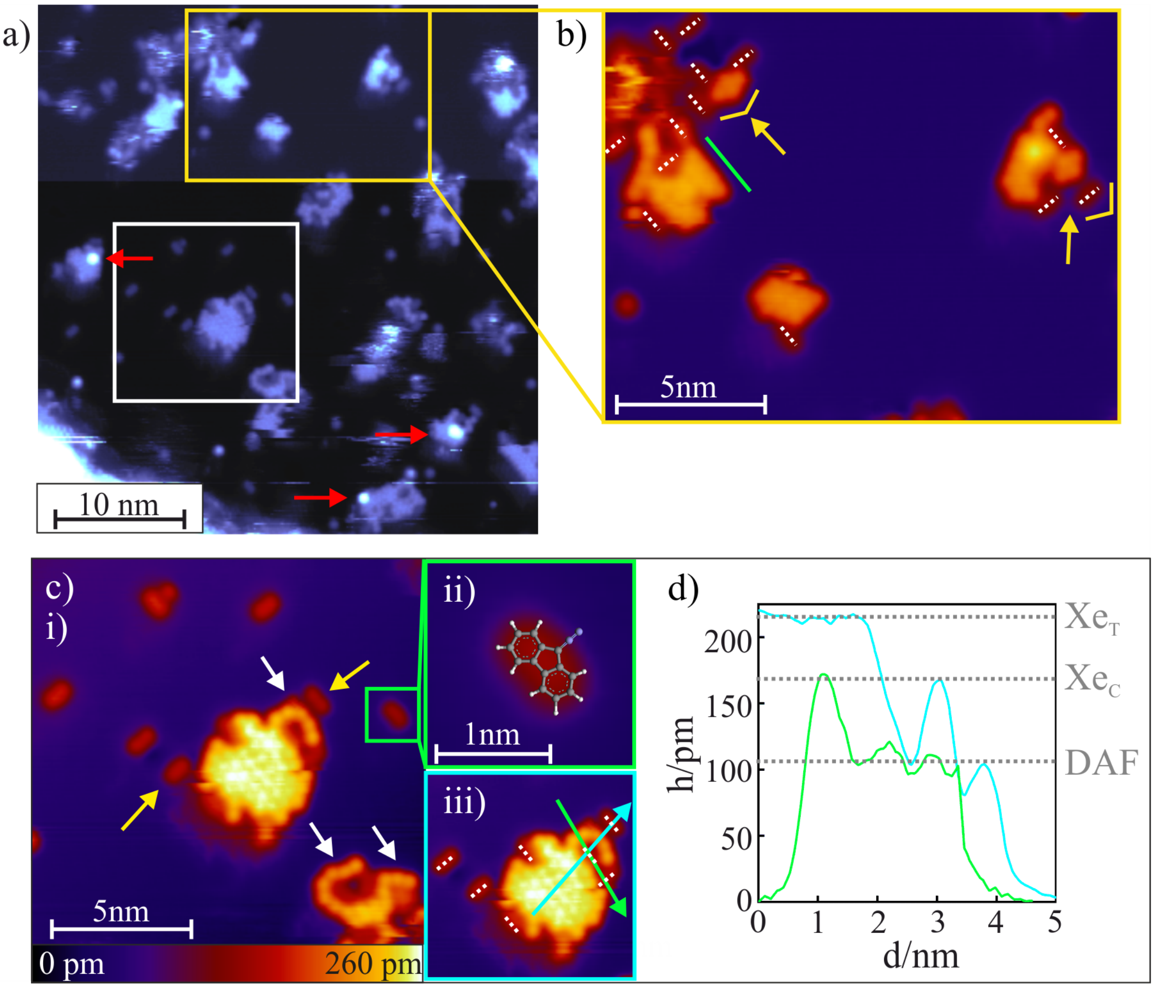

Figure 24: Xe islands with subsequently coadsorbed DAF on Ag(100) on lower terrace next to a step edge (bottom left corner of (a)): a) Overview STM image, red arrows: protrusions on Xe (further discussed in *Sec.* 3.6.2), (b) & (c) magnifications of framed areas in (a), all images on false color scale, tunneling parameters: $I_t = 61\,\mathrm{pA}$, $V_t = 516\,\mathrm{mV}$; b) Area of top yellow box in (a), DAF monomer marked by dotted white lines in the molecular orientation as determined in *Sec.* 3.4.1, straight lines: outline of Xe island edge orientations: green: along preferred DAF orientation axis, yellow: different orientation fitting geometry of the gap between DAF molecules, rhombi of four atomic Xe islands between DAF molecules indicated by yellow arrows; c) Area of bottom white box area from (a); i): Original image of DAF molecules encapsulated in the island area, DAF molecules adjacent to Xe island indicated by yellow arrows, atomic chains (tentacles) indicated by white arrows; ii): Magnification of green box: superposition of molecule from STM image with DFT model of DAF; iii) DAF monomers marked by dotted lines (c.f. (b)), arrows: line scan paths of (d); d) Height profile along directions of arrows of respective color from (c-iii), assignment of species corresponding to the height levels according to label: top of Xe layer (Xe$_T$), atomic Xe chain (tentacle, Xe$_C$), DAF level (DAF)

Fig. 24a) shows an overview of several small Xe islands. The orthogonally oriented adsorbates, observed in the interspaces between the Xe islands, are identified as DAF-monomers according to *Sec.* 3.4.1. For the chosen tunneling parameters the DAF molecules have a lower apparent height than the Xe islands of $h_{\mathrm{DAF}} = (102 \pm 9)\,\mathrm{pm}$. The species are well distinguishable in STM images, due to their distinct apparent heights resulting in distinct pseudo colors (DAF: red, Xe: yellow) in *Fig.* 24b)-c). Both figures display magnified regions of *Fig.* 24a). *Fig.* 24b) shows the contact region of Xe to an DAF agglomerate and *Fig.* 24c) shows the contact region of Xe to separate DAF molecules. The true-to-scale DFT model of DAF is superimposed to the protrusion in the green box in *Fig.* 24c-ii). Two molecules are observed close to the island edge within *Fig.* 24c-i). These molecules are pointed out by yellow arrows. The DAF molecular alignment to the Ag(100) lattice is not influenced by their vicinity to the island.

On closer inspection, the island looks slightly tentacle-like. There are several features at the edge of the Xe island with reduced height in comparison to the island level. Some of these lower features are enclosed by the tentacles of atomic chains. These features have about the same size and orientation as the DAF monomers found on the bare metal surface. This observation suggests that DAF is partly integrated into the Xe island. This is furthermore confirmed by the height profiles of the island and the encapsulations along the paths as marked in *Fig.* 24c-iii) and plotted in *Fig.* 24d). Apparently, the encapsulations have the same apparent height as the monomers next to the outer island edge and are hence identified as DAF.

The DAF monomers in the Xe contact regions are found aligned to the substrate with their original orientation. DAF molecules that fit the preferred orientations presented in *Sec.* 3.4.1 are marked by dotted lines in *Fig.* 24b) & c-iii). Due to their random pairing and orthogonal alignment to the closed packed Ag directions, the local sets of DAF molecules have a certain short-range but no long-range order. The local sets of DAF molecules differ by number of individual molecules, relative translation and relative orientation. For that reason, differently shaped cavities and openings are formed. These openings can serve as nucleation pockets for Xe during the cooling process. Accordingly, the growth orientation of Xe islands nucleated in different openings of DAF agglomerates or between separate molecules differs.

The orientation of the straight lines in *Fig.* 24b) mirrors the orientation of the Xe island edges. In the case of the green line, the orientation is comparable to the orientation of the DAF molecules. In the case of yellow lines, the Xe edge orientation differs from those of the molecules. This is observed in the regions marked by yellow arrows. In these cases, a rhombus of four Xe atoms is found confined by three differently arranged DAF molecules, respectively. This confinement leads to a deviating relative orientation, which can be further expanded over the crystal lattice in case of Xe condensation. It is therefore concluded that the adsorption geometry of the DAF dictates the orientation of the Xe islands. The Xe islands are pinned to fixed coadsorbates.

Fig. 25 depicts a transition region between two differently aligned domains from a neighboring region (magnification of area marked in dark green in *Fig.* 23a)).

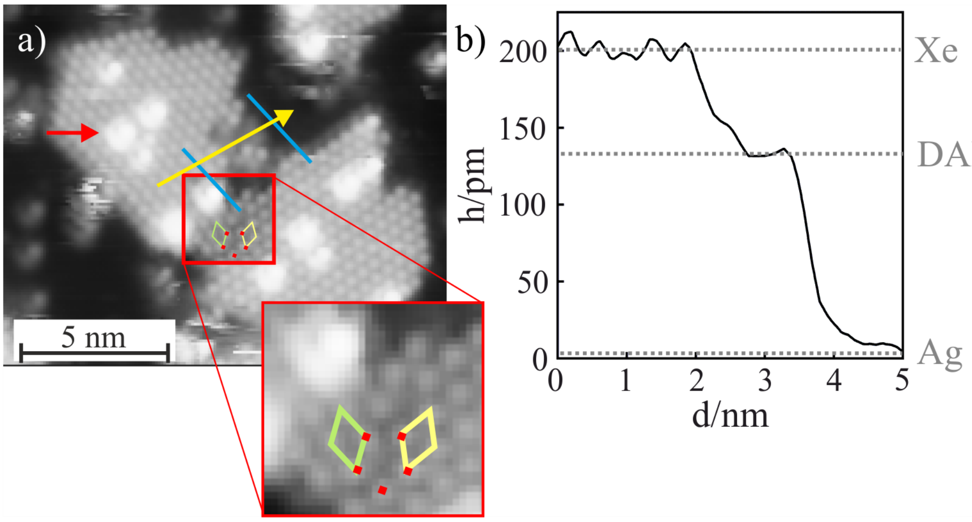

Figure 25: Boundary region between two Xe domains with different orientation of primitive unit cells, molecular inclusions in the gap between different domains marked in the area between the blue lines; a) STM image, orientation of unit cells magnified in red box, red arrow: example protrusions on top of the Xe layer, yellow arrow: line scan path of (b), tunneling parameters: $I_t = 61\,\text{pA}$, $V_t = 516\,\text{mV}$; b) Height profile in direction of the yellow arrow from (a), grey lines: different height levels corresponding to the species Xe, DAF and Ag

In the region marked between the blue lines, domains are separated by encapsulations of a lower apparent height. The height profile of the line scan in the direction of the yellow arrow from *Fig.* 25a) is shown in *Fig.* 25b). Three apparent height levels are observed. The top two levels have the same apparent height difference as the Xe and DAF level in *Fig.* 24d). Therefore, the lower protrusion level is assigned to DAF. The encapsulation of DAF presumably explains the different orientation angles of both Xe domains.

In the area magnified in the red box, the lattices gradually rotate and show a continuous transition into each other. In this quasi crystalline transition area the primitive unit cell from one crystal lattice (green rhombus) is connected via a pentagon to the primitive unit cell of the other one (yellow rhombus). The Xe lattice thus shows a certain flexibility to break the hexagonal symmetry to connect differently oriented domains, thereby avoiding vacancies in favor of interaction optimization. The adsorption sites do not strictly fit the substrates periodicity. Equally, it is to be noticed that according to *Fig.* 24 neither the Xe is found to enclose all of the DAF edges available nor does DAF enclose complete Xe islands. There is no indication that the contact line is maximized. Homogeneous regions of Xe islands and DAF agglomerates are observed; at contact lines of these regions no prominent mixing becomes apparent. The structures are kinetically hindered. Therefore,

it cannot be determined whether mixing is thermodynamically favored.
The main interaction dominating the alignment of DAF is the one with Ag(100), since the presence of Xe hardly seems to affect its adsorption geometry at all. Hence, the crystallization of Xe is regarded to be primarily caused by spatial restriction of its movement but not attractive interactions. In this work, STM studies reveal the Xe island orientation affected by local confinement due to the coadsorbate DAF. DAF molecules serve as nucleation pockets and cores dictating the growth of Xe islands. This agrees with LEED studies suggesting coadsorbates causing Xe pinning on Ag(111) as described in [32]. An indication for a second kind of DAF adsorption structure on top the Xe is the occurrence of additional protrusions on the islands. A protrusion of this kind is indicated by red arrows in *Fig.* 25a). These protrusions will be discussed in the following section.

3.6.2 Evidences for DAF Adsoption on the Xe-layer

Fig. 26 depicts protrusions on top of the Xe layer.

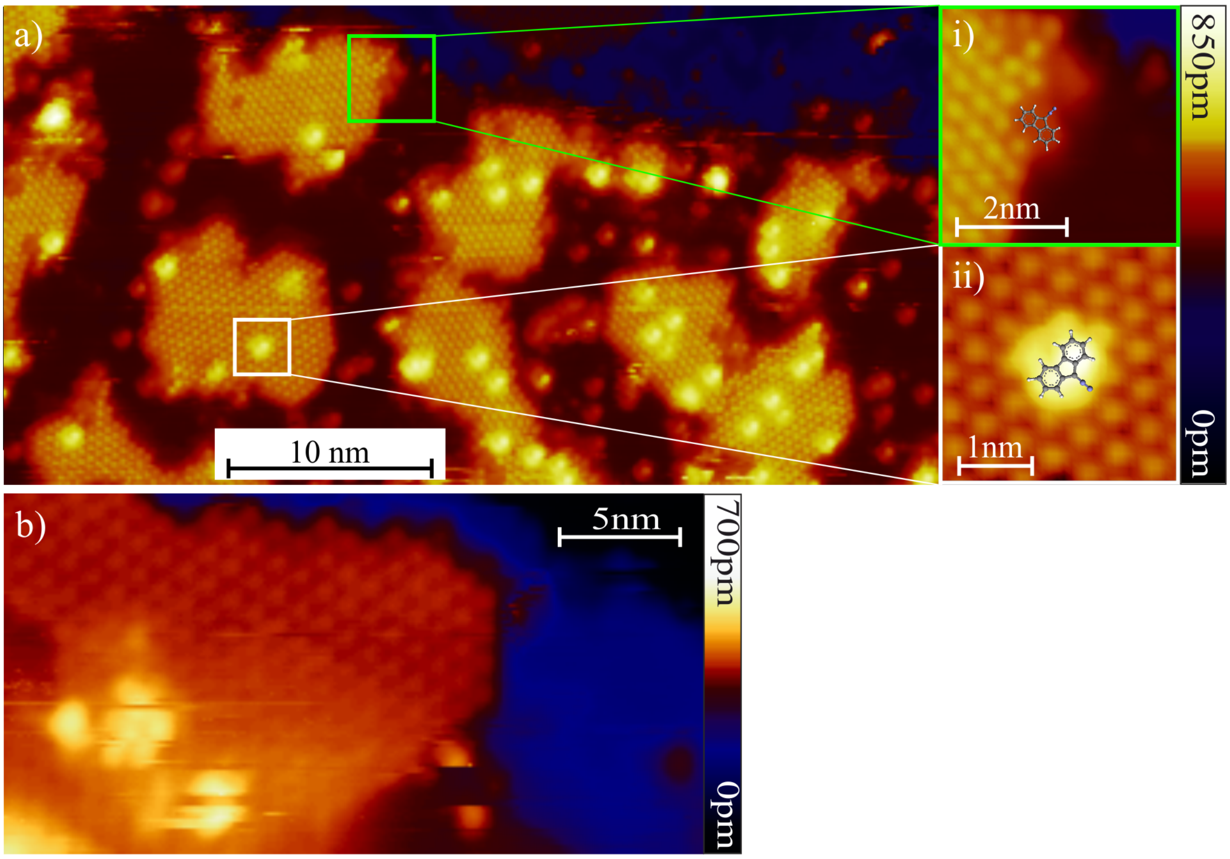

Figure 26: STM image of Xe islands in atomic resolution after DAF-deposition close to step edges on Ag(100), tunneling parameters: (a) $I_\mathrm{t} = 61\,\mathrm{pA}$, $V_\mathrm{t} = 516\,\mathrm{mV}$; (b) $I_\mathrm{t} = 61\,\mathrm{pA}$, $V_\mathrm{t} = 816\,\mathrm{mV}$; a) same sample region as *Fig.* 23 a) with encapsulated DAF framed by green box, top protrusion on Xe marked by white box, magnification of both boxes with DAF DFT model superimpositions aside; b) Xe island with on top agglomerate adsorbate, located next to step edge (terrace in blue)

Multiple additional protrusions are found on top of the hexagonal islands and are observed in several images taken from the same area as well as in different sample regions in close vicinity. However, in the majority of the images these protrusions are subject to a double tip effect (other than those seen in *Fig.* 24a)). Thus, the shape of the imaged protrusions presumably resembles the tip shape, but explicitly not the true shape of the adsorbates. The actual number of protrusions is also regarded to be overestimated due to replica multiples of imaged particles. Due to the tip effect, also the protrusions in *Fig.* 26 on the bare metal surface cannot be identified by shape. *Fig.* 26a-i), however, shows some island encapsulations of about elliptical shape, which resemble the DAF molecules discussed in *Sec.* 3.6.1 and fit to the dimensions of the superimposed DFT model. The presence of DAF on that image suggests that these protrusions on top of the layer are also DAF. For a rough size comparison, such a protrusion, indicated by the white box in *Fig.* 26a), is magnified and superimposed with the DAF model in the same scaling in *Fig.* 26a-ii). Thus, it is shown that the protrusion is of the same order of magnitude as a single molecule. However, since neither the real shape is imaged in this work nor the ideal STM image of DAF on Xe is known, no specific and reliable statement can be given whether this protrusion matches the molecular image on Xe at all.

Due to the close proximity to *Fig.* 24a), an impact of comparable DAF molecule density during the molecular deposition is assumed.

In course of the consecutive preparation procedure, DAF deposition follows Xe deposition. Therefore, it is reasonable to assume that DAF is deposited on top of the island as well as on the inter-island spaces resulting in two different adsorption cases for DAF. Under this assumption it may be concluded that the adsorbates on the islands are the same species as those next to the islands and, hence, DAF. *Fig.* 26b) shows an image taken from a step edge region. Likewise, additional protrusions are seen on top of the Xe, which cannot be resolved clearly due to image disturbances. In this case an agglomerate of top particles is observed.

Another conceivable candidate species to cause these protrusions may be displaced Xe atoms from the islands. Xe atoms can be displaced induced by the tip as discussed in *Sec.* 3.7.1 and in the context of *Fig.* 29.

The asymmetric assembly of protrusions suggests, however, an agglomerate of adsorbates, which resembles the adsorption behavior of DAF on Ag as discussed in *Sec.* 3.4.2, though no reliable conclusion can be drawn based on the image quality.

The presented images are, hence, considered a reasonable but still arguable indication for a successful DAF deposition on top of a Xe-layer.

3.7 Discussion

The present work is subject to two main methodological points of criticism. The first one is the number of measurement repetitions which is insufficient for statistical analysis for many of the imaged characteristics. Image repetitions are often recorded with different tunneling parameters leading to insufficient comparability among the images. As a result, properties observed in only one area, such as the different DAF adsorption structures, could not be reproduced on multiple locations in order to statistically validate them. The second point of criticism is the application of invasive tunneling parameters, particularly the application of very low tunneling resistances. In the following, proofs for local adsorbate displacement are presented and discussed in order to analyze the possibility of systematic tip-induced sample alterations as well as optimization strategies for a future experimental approach.

Both points of criticism, the low number of repeated and clearly resolved images as well as the choice of extreme tunneling parameters are ascribed to major difficulties in recording STM-images on the present sample. Within the scope of this work, it was screened extensively for tunneling parameters in order to circumvent arising disturbances.

These disturbances are mainly attributed to Xe motion, since the Xe mobility on Ag(100) is regarded to be very high. A low interaction of the Xe layer to the substrate is indicated by the rotational pinning as well as by its incommensurate fcc(111) superstructure. The substrate plays a subordinate role in dictating the ad-layer geometry and orientation.

This particularly low interaction results in high mobility and poses a distinctive difficulty in the STM-measurement of Xe on Ag(100). Several commonly reoccurring disturbances, which impede the recording of clearly resolved images at common parameters, are characterized and discussed below.

3.7.1 Common Imaging Disturbances and Measurement Interference Identifications

Fig. 27 summarizes the most prominent disturbance effects on the imaging process after Xe deposition. These common effects are referred to as horizontal smearing lines, artificial smoothing and observation of cloud-like shapes and are discussed separately in the following.

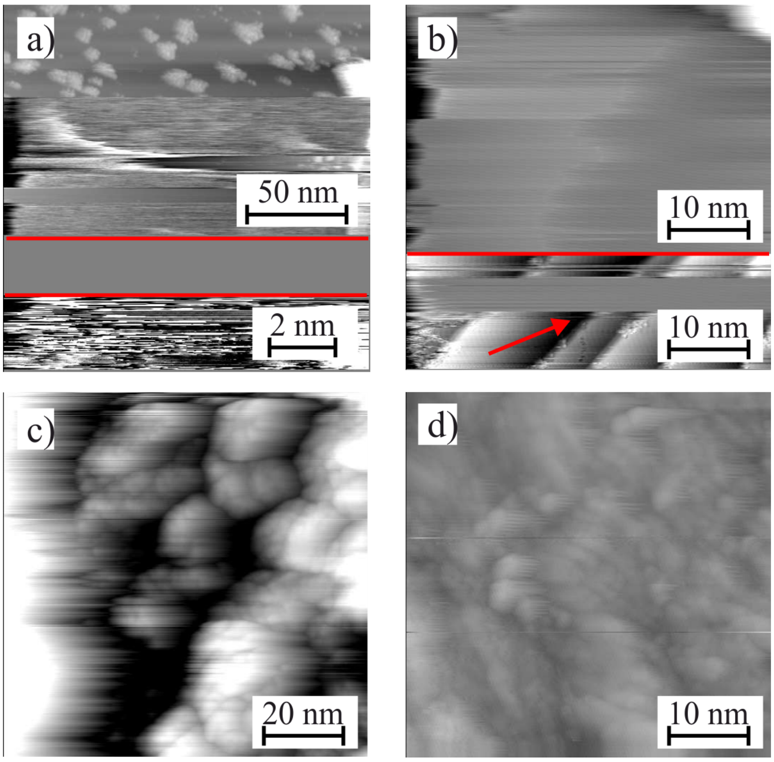

Figure 27: STM images of Xe adsorbed on Ag(100) with common image disturbances, red lines separate different images showing the same effect; a) Horizontal smearing lines covering Xe islands, top: I_t = 11 pA, V_t =459 mV, bottom: I_t = 4.0 pA, V_t =4 mV; b) artificial smoothing evens out steps (as indicated by the red arrow, top: I_t = 12 pA, V_t =4 mV; bottom: I_t = 9.3 pA, V_t =4 mV; c) Cloud-like shapes of extreme apparent height difference up to 10 nm, I_t = 5.2 pA, V_t =122 mV; d) More even cloud-like shapes, I_t = 13 pA, V_t =1955 mV

Horizontal smearing strictly follow the scanning direction as depicted *Fig.* 27a). Since the horizontal lines run clearly and exclusively along the scan direction they give an indication of tip induced displacement. It can be concluded that material is collected by the tip and dragged horizontally. For a rough classification of this effects its intensity is subjectively categorized as one of two exclusive classes: occasional (occ.) and extensive (ext.).

A high density of horizontal smearing lines might lead to an artificially smooth representation of the surface. Exemplary, *Fig.* 27b) depicts surface smoothing over a region of several terraces. These edged are displayed as a smooth area in the image section at the top of the red arrow.

The appearance of cloud-like structures on images impedes a clear resolution of the surface. Often, these cloud-like structures are marked by an unreasonably high difference in their apparent height Δh as classified in the following. In order to evaluate trends in the intensity of this effect three classes are defined:

- small (s): $\Delta h < 1\,\mathrm{nm}$
- medium (m): $\Delta h = 1\,\mathrm{nm} - 4\,\mathrm{nm}$
- large (l): $\Delta h = 4\,\mathrm{nm} - 10\,\mathrm{nm}$

Fig. 27c) shows large cloud-like structures, whereas *Fig.* 27d) shows small cloud-like structures and the recorded surface appears more even. It is concluded that all disturbances reported can be attributed to interactions with the Xe. In order to characterize the exact origin of these disturbances, the applied tunneling parameters are examined for effect classification in relation to literature.

STM offers three ways of surface modifications dependent on the experimental parameters. These surface modifications can be driven by mechanical force between the tip and the surface (parameters: $V_\mathrm{t} \rightarrow 0\,\mathrm{V}$, $I_\mathrm{t} \rightarrow 0\,\mathrm{A}$), by electric fields (parameters: ($P \approx 10^7$ V/cm – 10^8 V/cm) or electric current ($I_\mathrm{t} = 10\,\mathrm{pA}$ – $100\,\mathrm{nA}$) [14,39–46].

These manipulations can be furthermore divided into lateral and vertical manipulation. During lateral manipulation, a particle is in contact with the tip and the surface while it is moved by tip-particle forces. During vertical manipulation a particle keeps in contact with the tip but loses contact to the surface.

The tunneling resistance was reported to be the main factor controlling lateral force based manipulation by Hla et al. [47]. Accordingly, small tunneling resistances which fall below a system-specific resistance threshold enable force-induced manipulation (usually several hundred kΩ [14]).

In the present studies, the tunneling parameters were varied over a huge current and voltage range in order to identify the most sophisticated tunneling parameters for undisturbed adsorbate imaging. The corresponding tunneling resistances for this images are calculated as follows:

$$R_T = \frac{V_\mathrm{t}}{I_\mathrm{t}}. \tag{4}$$

The relative frequency of the different types of disturbances as a function of the associated tunnel resistances is shown in *Fig.* 28. Negative resistances correspond to the inverted sign of the applied bias. Adsorbate imaging implies DAF molecules as well as the mapping of Xe islands as presented in *Sec.* 3.3, which are also identified as subject to tip interactions in the later section *Sec.* 3.7.4.

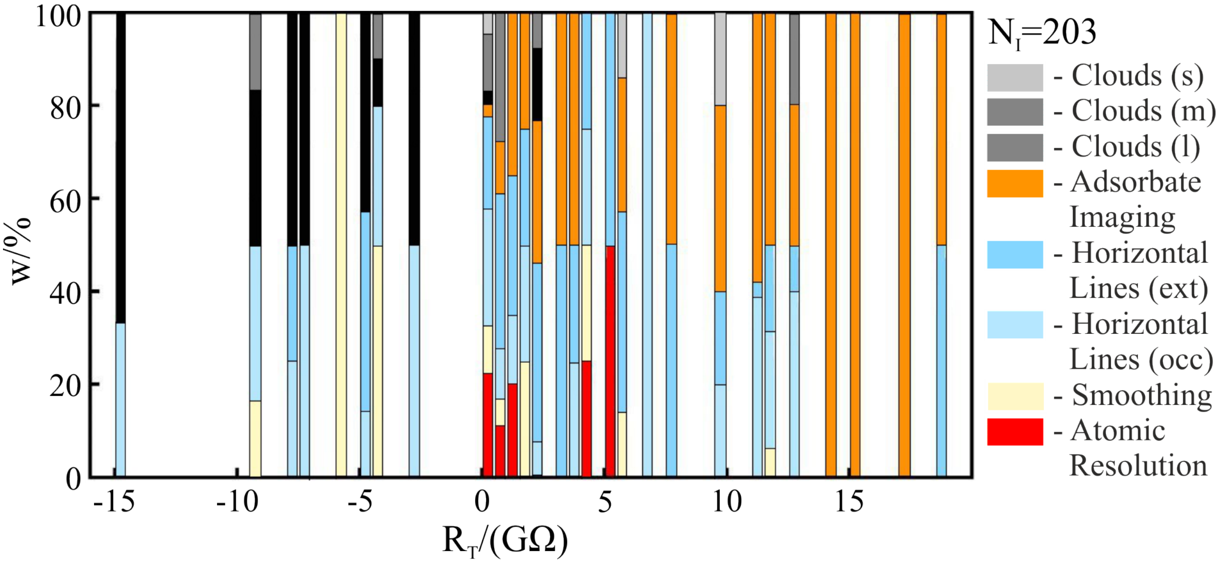

Figure 28: relative frequency $w\%$ diagram of types of disturbances in dependence of the tunneling resistance R_T for N_I analyzed images

Smearing lines are observed for a wide resistance range, thereby exceeding the theoretically expected range for force-induced lateral manipulation (0 Ω to several hundred kΩ [14]). From this it is concluded that several manipulation mechanisms are involved at the same time for the measurements presented in this work. *Fig.* 29 represents a voltage series over a Xe-island in which the bias is gradually reduced from 766 mV to 566 mV. The tunneling current is kept constant at 61 pA. The images show smearing disturbances resulting in a decrease of the island size and a change in the shape of its edges. For decreasing voltage i.e. tunneling resistance the manipulation intensity also decreases. A stable image is subsequently obtained after reaching an tunneling bias of 516 mV. The island edges, which are altered most in course of the series are marked with blue lines for better visualization. The red arrows in the top row point at an island vanishing between the recording of image a) and b). In the bottom row, the arrow points out an island group which appears in image d) and is partially ablated in e).

A reduction of the displacement with decreasing voltage rather indicates a potential induced but not force induced displacement mechanism. Full Xe coverage is observed for step regions several times. Contradictory, completely uncovered steps are also observed in the close proximity to this region or after multiple scans. Consequently an extensive Xe ablation becomes evident in such regions.

In addition to this presumed potential induced mechanism, material displacement also becomes apparent at very low tunneling voltages. Two different examples of low voltage displacements are shown that fit the tunneling resistance regime of force induced displacements.

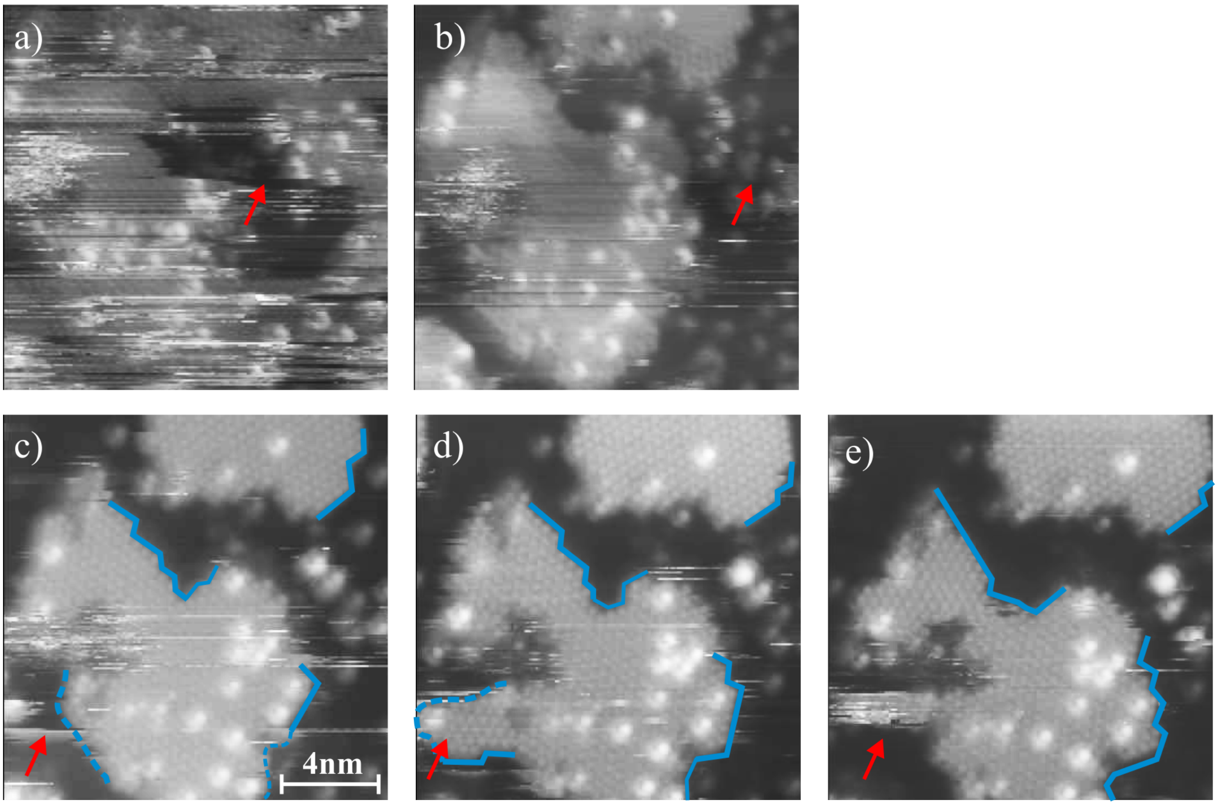

Figure 29: Voltage series for the same sample region, red arrow: moving island fragments, blue lines: changing island boundary lines, tunneling parameters: I_t = const. = 61 pA, a) V_t = 766 mV, b) V_t = 716 mV, c) V_t = 666 mV, d) V_t = 616 mV, e) V_t = 566 mV

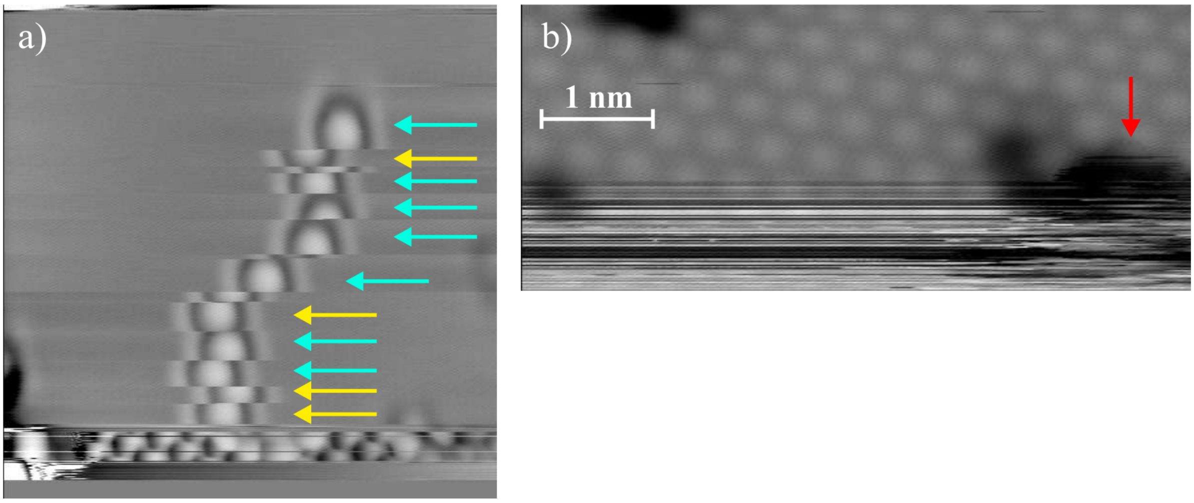

Figure 30: STM images; a) Apparent image during lateral pulling/pushing mode manipulation: I_t = 7.9 pA, V_t = 2 mV; b) Atomic resolution of Xe layer with vacancies on Ag(100); onset of horizontal smearing disturbance at position indicated by the red arrow; tunneling parameters: I_t = 12 pA, V_t = 4 mV

Fig. 30a) shows the apparent image trace of a particle moving along the slow scanning direction of the scan. The semispheres along the trace represent the particle temporary occupying an adsorption site. Depending on the orientation of this semispheres, the displacement mechanism can be attributed to several tip-adsorbate force induced lateral manipulation mechanisms, i.a. pulling and pushing. Pulling corresponds to a particle following the motion of the tip due to attractive interactions and results in a sudden jump movement of a particle below the tip center as the tip moves away from the particle. This movement results in an image of the semicircle of the descending flank of the particle along the motion direction. Pushing corresponds to the escape of the particle from the tip due to repulsive interactions. A sudden jump movement of the particle away from the tip is caused as the tip approaches the particle peak. This movement results in an image of a semicircle of the ascending flank of the particle. The pattern recorded in *Fig.* 30a) displays a row of semicircles of which some seem to obey the pulling (marked by blue arrow) and some of them seem to obey the pushing (marked by yellow arrow) motion. This reveals a very unstable tip-particle interaction. At the bottom part of the scan area, the image of the particle disappears and the substrate is resolved atomically. This effect can be attributed to vertical displacement of this particle. Thus, a variety of uncontrolled and non-uniform forces interacting with the adsorbate at corresponding tunneling parameters become evident.

Uncontrolled vertical displacements may explain the enhanced resolution of images measured at low tunneling resistances as well as the missing image stability. The image improving effect of vertical manipulation is explained by the uptake of that particle by the tip which alters the tip's chemical and physical properties due to bond formation. This may lead to the sharpening of the tip apex and cause a better resolution [14]. Neu et al. present a clear improvement in the resolution between the selective uptake and deposition of an Xe atom on Cu(211) [48].

In this work, tip modifications of that kind lead to the outstandingly sharp images of the atomic resolution of the Xe-layer recorded at low voltages, but it becomes equally apparent that these measurement parameters cause strong uncontrolled interactions with the sample and may alter it.

The tip-induced uptake of a single Xe atom from the layer becomes more evident in *Fig.* 30b), which shows a Xe layer with vacancies on Ag(100) in atomic resolution. The onset of the horizontal smearing disturbance is noticed at the top of a vacancy as indicated by the red arrow. A possible explanation is that vacant atoms in the hole are taken up by the tip and cause disturbances due to unstable movements following the tip.

Weiss et al. reported about tip-induced island dislocation of small Xe islands of several atoms on Pt(111) [49]. Therefore, the STM tip was placed over the island edge and the feedback loop was turned off, followed by subsequently approaching the surface up to 260 pm. The applied bias was changed from its onset value between -2 mV to -10 pm up to 10 mV and back after returning the tip to its initial height. The described procedure reveals a striking analogy to the critical parameters of the present measurement and resembles the used tunneling bias. The exclusive Xe measurements in *Sec.* 3.2.1 are recorded with critically low sensitivity of the feedback loop (DSP integrator of $-9.4[1/\mathrm{T}]$). This suggests that for the chosen measurement parameters the explained displacements affect the sample.

A plausible explanation for cloudlike structures may be a scan with tip penetration below the surface of the layer. In that case highly fluctuating and multilateral interactions would arise, as the matter below the tip and the tip atom itself would contribute to imaging. Hence, for future experiments a higher DSP sensitivity (integrator > -90 [1/T]) should be selected in order to avoid layer penetration.

A large number of the manipulation types already discussed imply that the tip collects a huge number of Xe atoms. This idea is further supported by the potential observation of single Xe atoms on Ag(100) as discussed in *Sec.* 3.7.2. Therefore, it is concluded that the tip is occupied with a large amount of Xe for most measured images causing the observed image instability.

Furthermore, for most measurements, the tunneling current is chosen larger than 10 pA and thus enables local sample heating that increases the mobility of the adsorbates. Especially in the case of Xe, which is known for its outstanding mobility on metal surfaces, this effect is expected to be prominent. Current-induced mobility changes of the Xe may not only concern the sample but also the material previously collected on the tip which presumably explains the unusually wide parameter range of observed disturbances. This range may expanded by a persistent change in the chemical and physical properties of the tip and thus the STM image.

For future experiments, the tunneling currents used should initially be kept below 10 pA in order to exclude current-induced mobility increases. The tunneling bias should be decreased systematically and carefully in order to examine the bias range of reduced potential induced displacement but under avoidance of close tip-sample distances which may allow Xe accumulation on the tip. The Integrator of the feedback loop is to be chosen particularly sensitive.

One more potential factor of image disturbance, not related to the Xe, is the evident insufficient fixation of the sample on the sample holder, as identified by the rotation of the single crystal in *Sec.* 3.4.1. Sample vibration may further explain vast problems in stable image recording and must be excluded in the future.

3.7.2 Discussion of Further Adsorbate Structures

A round protrusion type is repeatedly imaged alongside with the DAF and its cleavage product (c.f. *Fig.* 19a)). *Fig.* 31a) shows two images of DAF (marked by black arrows) alongside with these round protrusions.

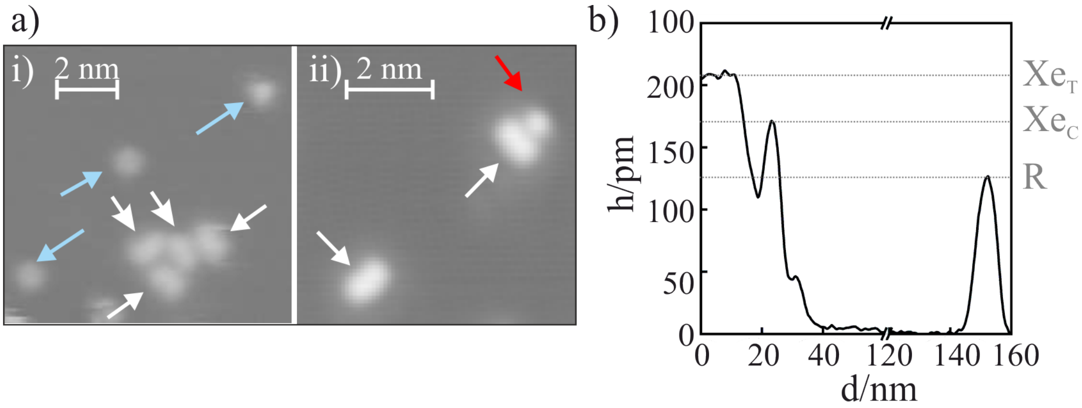

Figure 31: Round protrusions; a) STM images of commonly appearing round protrusions in i) the neighborhood (marked by blue arrows) and ii) next to (marked by red arrow) DAF (marked by white arrows), tunneling parameters: (i) $I_t = 8.1\,\mathrm{pA}$, $V_t = -1\,\mathrm{mV}$; (ii) $I_t = 61\,\mathrm{pA}$, $V_t = 516\,\mathrm{mV}$; c) height profile analog to *Fig.* 24d) over same island but continued onto a round protrusion, outline of species corresponding to the line scan section according to label: top of Xe layer ($\mathrm{Xe_T}$), atomic Xe chain (tentacle, $\mathrm{Xe_C}$), round protrusion level (R)

In the first image the round protrusions are found on the substrate in larger distance (<3 nm) from the DAF (marked by white arrows). In the second image, a round protrusion is found next to a DAF molecule (indicated by red arrow). This round protrusions are distinguishable from the DAF since they are of lower apparent height. These species are assumed to be single Xe atoms. This assumption is based on their spherical appearance and on the comparison of their height profiles with the Xe islands discussed in *Sec.* 3.6. *Fig.* 19b) shows the height profile along the Xe island of *Fig.* 24b-ii) through the discussed island extension of a tentacle-like atomic Xe chain to one of this round protrusions. From the height profile it can be seen that the island top (labeled $Xe_{[}T$) is of larger apparent height than its extension of the atomic chain (labeled Xe_{C}). The discussed round protrusion (labeled Xe_{T}) has a lower height than the chain. The round species fits well into the trend of decreasing apparent heights with reduced number of neighboring atoms. The larger apparent height of the Xe island compared to the chain can be explained by the larger confinement of the electron density of the neighboring atoms present in both spatial directions. Due to the reduced number of neighbor atoms in the case of the chain, the electron cloud can disperse, which leads to a decrease of the apparent height. For single atoms, an even more reduced apparent height can be expected compared to dense islands or chains. Due to a tip convolution effect a single atom is furthermore depicted broader than in a crystal. The full width at half maximum (FWHM) of the round protrusion measured in *Fig.* 24b) is (750 ± 2) pm which is larger than the compared FWHM obtained for single Xe atoms on Ni(110) according to *Fig.*3 in [50] of about 500 pm. A broader appearance of Xe on Ag(100) is not excluded.

Thus, the occurrence of single Xe is evident, but can not be explicitly proven. Conceivable system interactions of the measurement which may be indicated by the observation of single Xe atoms are discussed further. The observation of single atoms contradicts harshly the reported high mobility of Xe allowing crystallization on steps or other nucleation cores. Consequently, single atoms may have been placed under different conditions than those species of ordered growth. It can be assumed that the atoms have been picked up by the tip due to effects described in *Sec.* 3.7.1 and dropped off onto the Ag substrate or at molecule edges in the course of the scanning process. In case of *Fig.* 19a) (tip forming region) it is very likely that Xe was scattered by the tip forming pulse.

This is regarded a further indication for vertical Xe displacement. Thus, it cannot be excluded that the protrusions on top of the Xe islands, discussed in *Sec.* 3.6.2, are equally displaced Xe atoms.

3.7.3 Discussion of the Adsorption Geometry of Pure Xe

A hexagonal Xe lattice is observed on Ag(100). On terraces which are not in the proximity of any steps, this lattice shows identical orientation of the closed packed direction vectors on two different sample regions. The examination of these two images suggests an incommensurate superstructure which is aligned to the substrate. However, the number of measurements is regarded as insufficient for reliable statistical evaluations.

The alignment of the superstructure to the substrate is studied by two approaches: the superposition in terms of a polar diagram of the averaged lattice orientation of the substrate and the superstructure from different images as well as by reverse FT based grid extrapolation of an image of partial atomic resolution of both species at the same time. The alignment to the substrate is strongly suggested by the FT approach, which is considered the more credible one. The high credibility is given for reasons of an unadulterated representation of the relative orientations between the Ag substrate and Xe rows. Assuming an intrinsic STM angle error of 5%, the superposition method agrees with this result. The average lattice parameter of the Xe superstructure on Ag(100) of (473 ± 5) pm is calculated over all closed packed directions under the assumption of an ideal hexagonal system. The determined average lattice parameter along different closed packed directions, however, differs by up to 5.4%. Based on the low number of images, no clear distinction can be made between a distorted image of an ideal hexagonal structure and a real distorted pseudohexagonal structure. Under the assumption of an ideal hexagonal geometry, taking the mean over the different closed packed directions reduces the distortion impact as it gets averaged out along the different directions.

In this work, an adjustment of the piezo constants is omitted, since present reference images of the Ag surface show unstable and partially implausible lattice constants which do not provide an reliable basis for a calibration. Accordingly, it is further possible that the Xe distances determined here are overestimated similar to those of the Ag(100).

It is not assumed that the lattice properties determined here are influenced by the previously discussed displacement. The lattice constants and orientations are determined from regions of continuous periodicity. As conceivably only few atoms may be moved by the tip simultaneously [49], the hexagonal structured Xe lattices can be regarded as unaltered. In particular, the orientation of the Xe lattice to the Ag substrate remains unchanged by tip displacement and a systematic restructuring of the actual Xe lattice geometry can be ruled out.

However, the alignment of the superstructure to the substrate as well as Xe lattice constant are longrange order properties. The applied technique STM allows local and short range studies. The discussed properties can be studied much more conveniently considering techniques evaluating a system's longrange order. A possible measurement technique for longrange order evaluation would be a LEED or IV-LEED experiment. Differently aligned superstructures can be distinguished from these experiments as they result in different diffraction patterns. Therefore, the reflex numbers and intensities are directly related to the number of distinguishable adsorption structures or their relative distributions. The geometric characterization of a superstructure can hence be evaluated more precisely with LEED studies. However, this method is not applicable for the determination of local characteristics. Regions of distinguishable diffraction patterns cannot be characterized in terms of their location on the sample (steps vs. terraces) and their size by LEED. Hence, STM studies, like this work, depict an excellent combination with diffraction experiments. For further insight to the adsorption behavior Xe on Ag(100) a LEED analysis would be the favourable follow-up experiment.

3.7.4 Discussion of Island Morphology

Xe islands recorded with comparably low tunneling resistances ($I_\mathrm{t} = 11\,\mathrm{pA} - 36\,\mathrm{pA}$; $V_\mathrm{t} = 153\,\mathrm{mV} - 507\,\mathrm{mV}$) are of irregular shape, as shown in *Sec.* 3.3. Xe islands are observed in a wide size range from $<3\,\mathrm{nm}^2$ to $275\,\mathrm{nm}^2$. All islands of a size larger than approximately $10\,\mathrm{nm}^2$ show consistent fractal dimensions of an average of $D_\mathrm{F} = 1.761 \pm 0.03$. The uniformity of the fractal dimension of the more extensive islands indicates that their formation follows the same mechanism.

The irregularity of the island shapes contrasts the frequently observed tendency that the preferred island shape resembles the basic geometric characteristics of the substance's crystal lattice. For hexagonal islands this tendency is observed for Xe island formation on Pt(111) at 17 K after annealing to 29 K as depicted in *Fig.* 1 of [51] and Pt growth on Pt(111) [52]. However, no hexagonal shaped islands mirroring the hexagonal lattice symmetry are found in course of this studies.

The temperature dependence of the morphology of Xe submonolayer islands on Pt(111) was reported in [38]. In these studies a morphology transition towards larger and more complex shaped islands was observed starting at an onset temperature of 20 K up to 50 K. So-called "curly" or ragged rim island structures of irregular shape were observed, with a structural complexity of the islands deposited at 30 K approximately resembling the complexity determined in this study.

Nevertheless, since adsorbate displacement becomes obvious throughout the studies, it is believed that this islands are formed due to the interaction with the scan. This is indicated by horizontal displacement lines and occasionally observed bare substrate areas on commonly fully covered step edges, as well as the non-consistent island height distribution. The height distribution indicates amorphous islands. Local heights larger than a mono layer are observed. These observations contradict the ordered Xe lattices as seen in all images of atomic resolution as well as the general expectation of a layer by layer growth for rare gas adsorption on metals [22, 53]. The amorphous Xe cluster in the top left image corner of *Fig.* 8a) is attributed to be caused by tip induced piling for example. It is concluded that the amorphous islands are composed of displaced Xe atoms from torn open and piled Xe(111) layers.

The smaller fractal dimensions of the smaller islands are mainly an effect of their lower area fraction per pixel ratio. A low number of binary selected pixels by the "flooding" function can lead to structures that have more fractal properties than the extensive islands. Besides, images of different area sizes and different tunnel parameters are considered here. A difference in the image sizes results in a different number of pixels per island for islands of the same area (i.e. a different degree of shape adulteration by the intrinsic pixel shape). The choice of different tunneling parameters affects the apparent height of an island. This influences the allocations of pixels to the islands in the outer boundary regions near the height threshold. Islands measured with higher tunnel parameters are thus assigned to a slightly larger area with more pixels. On small islands, this effect has a very strong influence on the determined shape, since single pixels constitute a high percentage of the total area. This explains the scattering distribution of fractal dimensions for small islands. Furthermore, since the small islands commonly show an elongated maximum height region aligned to the scan direction, Xe displacement is indicated at the same time. Partially, the

unstable properties of small islands may also be attributed to displacement movement, since smaller islands are expected to be less well-anchored than more extensive ones.
The island borders on images with atomic resolution likewise provide various proofs for the occurrence of measurement related displacements, such as seen in *Fig.* 29. It is concluded that the island shapes presented on different images in here are unauthentic over the full range of tunneling parameters applied.

The islands considered in the morphology analysis of *Sec.* 3.3 are assumed to be composed out of pure Xe. This is concluded because an attempted DAF coadsorption and DAF measurement is considered to be failed for the corresponding preparation: no DAF molecules are found in the island interspaces and no reaction is observed for a subsequent laser irradiation of the sample ($\lambda = 365\,\text{nm}$). No surface bound carbenes are observed in tip forming areas. Contrary to the preparation of the same DAF deposition temperature, as presented in *Fig.* 26, the islands show no subdivision in areas of distinguishable homogeneous heights. Besides, the islands studied here in larger scope resemble the ones observed during a preliminary examination before the DAF deposition attempt in terms of size and shape. Presumably, the miscarried DAF deposition is the result of an closed evaporator shutter. The presence of DAF can, however, not be excluded for certain for this analysis series.

3.7.5 Discussion of DAF Adsorption Structures

DAF monomers as well as their tip induced cleavage products are found in a uniform alignment to the Ag[1 1 0] and Ag[$1\,\bar{1}\,0$] directions exclusively. The determined alignment to the substrate was studied in terms of symmetry evaluations of molecular orientations of the respective polar diagrams in reference to the substrate geometry. The alignment and accessible adsorption sites were furthermore studied by FT analysis of a sliding pattern caused by molecular displacement and compared to the orientation and distance measurement of a pushing trace of molecular displacement. All methods agree that DAF adsorbs aligned to the Ag[1 1 0] and Ag[$1\,\bar{1}\,0$] directions with an adsorption site periodicity of d_{Ag}. The molecular orientation is furthermore congruent to a pseudo atomic image of the metal surface. Thus, the studies of the monomer species adsorption structure is regarded as highly credible.
For a statistically evaluable and comparable analysis of the spatial molecular measures, a larger number of images recorded at constant tunnel parameters is needed. This could not be realized in the context of the work due to unstable measurements, which required a frequent change of the tunnel parameters for image optimization. In order to allow a proper comparison to the observations of DAF on Ag(111) it is necessary to repeat the

measurements using identical parameters. However, the measures presented here give a rough comparison of sizes that allow an outlook on upcoming studies. It is recommended to investigate the adsorption structure of DAF at 53 K once more in the absence of Xe in order to clarify the origin of the dimers.

The occurrence of dimers and monomers on different sample regions at the same time are strongly differing observations. These observations must be attributed to vastly differing local conditions acting on the molecules. Changed substrate interaction in the dimer case, due to an underlying Xe layer is a plausible hypothesis with regard to the disappearances of an alignment to a quadratic base pattern. However, this assumption is regarded critically, since images with dimers alongside to rectangular vertical displacement traces are recorded. These traces are oriented in the same way as in the case of the agglomerates/monomers. Accordingly, the molecular trace indicates a movement along the Ag primitive unit vector directions.

Another possible explanation for dimer formation would be a local energy supply delivering temporary greater kinetic mobility, which allows the elsewhere hindered dimerisation. Though, in the monomer case, the interaction to the substrate is dominating the adsorption structure. DAF movement is evident at the deposition temperatures, due to cluster formation, while no preferred dimer formation is indicated. The close proximity of different molecules does not change the DAF orientation and dimerisation seems not to be favored at all.

The observation of dimers, however, suggests that a dimer pairing represents a thermodynamically favorable product. A causal linkage of dimer formation may be drawn to a high field emission (each +100 V & −100 V), which was performed prior to the dimer observations. A high field emission may result in two possible effects: the tip may be improved in such a way that subsequent images structures are recorded which previously could not be measured. A vast change in measurement quality may suddenly allow DAF recordings in the more complicated measurement situation on top of the conceivable Xe layer. Another possible effect of the high field emission, however, can be that the DAF dimers originate from a sample region that has received a large energy supply from the high field emission which induced the dimerisation. Hydrogen bond formation as well as the closing of chemical bonds are a conceivable effect depending on the local energy supply by the strong voltage pluse, depending on the distance to the pulse center. However, the conceivable effect of the high field emission to the dimer region is regarded as low, since the measurement position on the sample was chosen purposefully far away from the location of the high field emission. Furthermore, monomers and agglomerates were observed subsequent to the dimers, which contradicts an extensive influence of the high field emission on DAF dimerization. The origin of the dimers cannot be totally clarified

here. A structure changing influence of the tunnel parameters is excluded, since both species can be found on different images measured with identical parameters.
The observation that dimers can be imaged at tunneling voltages of 260 mV (i.e. energies of 0.3 eV) while applying tunneling currents up to 150 pA may indicate that the subdivisions of this double protrusions are bound by chemical bonds rather than by H-bonds. However, the dimerization under bond formation between two DAF molecules leads to 9,9'-bifluorene, which is not planar, since the two C9 atoms are sp^3-hybridized. The expected STM image of this species has two protrusions of different heights [5]. Furthermore the symmetry axis of 9,9'-bifluorene along the C9-C9 bond does not fit the observed lateral offset of the ellipses. A chemical bond between the DAF molecules in the reported dimers is excluded here.

3.7.6 Discussion of DAF Adsorption on top of the Xe Layer

A total of 18 images is recorded from neighboring sample regions which show further protrusions on the Xe layer. This protrusions are an evidence for DAF adsorption on top of the Xe islands since adsorbates adjacent to theses islands are unmistakably identified DAF deposited consecutively after the Xe. Accordingly, a reasonable indication for the possibility of DAF adsorption on top of Xe islands is presented. Though the protrusions cannot be resolved well enough for identification of the adsorbed species and the reproducibility is low. Therefore, the experiment of DAF deposition at 53 K on Xe should be repeated in future experiments for a more detailed analysis. It is equally conceivable that the protrusions are displaced Xe atoms dropped by the STM tip. The voltage series presented in *Fig.* 29, which reveals massive Xe displacement is recorded directly before these measurements. It may hence be assumed that a fraction of the displaced Xe is accumulated on the tip during the measurements of these protrusions. *Fig.* 24a), which shows several protrusions on Xe islands, shows round protrusions on the Ag sample at the same time. These round protrusions are regarded as potential single Xe atoms according to *Sec.* 3.7.2. Under the adsorbate assignment to Xe atoms it must be assumed that the tip loses single Xe atoms during the scan which might result in further protrusions on the metal surface as well as on the islands. The chosen tunneling voltages for the invasive voltage series ($V_\mathrm{t} = 866\,\mathrm{mV}$) as well as for the imaging of the protrusions on the Xe ($V_\mathrm{t} = 516\,\mathrm{mV}$) should correspond to rather large tunneling distances and hence comparably low physical interaction. The imaged displacement in course of the voltage series may rather be attributed to electric field interaction than physical interactions but conceivable vertical displacement cannot be excluded here, since the tunneling current of $I_\mathrm{t} = 61\,\mathrm{pA}$ is chosen arguably high. All images of protrusions on Xe islands show the presence of tip effects (such as horizontal smearing or double tip multiples of protrusions or shadowed island edges) of differing extent.

The observation of island ablation but not top particle ablation in *Fig.* 29 suggests a distinction of two species of different mobilities. Since the DAF mobility is ranked lower than the Xe mobility the conceivable protrusion assignment seems reasonable.

4 Conclusion and Outlook

In this work, Xe and DAF are adsorbed on Ag(100). The adsorption structures of both species are characterized separately as well as in their contact areas.

Xe deposited on Ag(100) at 70 K-75 K is observed as incommensurate fcc(111) superstructure. The surface lattice parameter of this superstructure is determined to be (473 ± 5) pm. This implies a stretch of the surface lattice constant of 7% compared to pristine bulk Xe. On terraces, an alignment of the closed packed Xe rows to the conventional unit vector directions of Ag(100) is evident. On small terraces close to step edges, full Xe coverage is observed, indicating Xe growth to be initialized next to step edges. In these regions, domains of Xe(111) without substrate alignment are observed. This phenomenon is attributed to impurities collected at the steps causing Xe domain pinning in different rotational geometries as observed for Xe on Ag(111) [32].
The Xe layer is characterized as a sub-monolayer film of an average coverage of $\theta = (20 \pm 4)\,\%$. Islands are observed in a size range from $<3\,\mathrm{nm}^2$ to $275\,\mathrm{nm}^2$ and show consistent fractal dimensions of $D_\mathrm{F} = (1.761 \pm 0.03)$ for islands larger than $10\,\mathrm{nm}^2$. The height distribution of these islands indicate amorphous structures and they are regarded to be artificially created by tip induced Xe displacement.
These studies should be extended to LEED analysis in order to determine the longrange order characteristics with higher precision. Diffraction studies also allow to circumvent measurement interferences such as reported for the STM scan. Measurement techniques with reduced interaction can be used in order to determine the origin of amorphous island structures, in order to distinguish whether these islands are formed by natural growth or during the STM measurement.

DAF is consecutively deposited after Xe at deposition temperatures of $T_\mathrm{dep} = 63\,\mathrm{K}$ and $T_\mathrm{dep} = 53\,\mathrm{K}$. For the 63 K deposition, amorphous clusters are formed revealing mobility of both species. For the DAF deposition at 53 K, DAF molecules are observed on bare Ag(100) surface regions as well as in contact with Xe islands. Furthermore, indications of DAF adsorbed on top the Xe islands are found. On bare Ag(100) regions, DAF is identified as monomers of uniform alignment to the closed packed directions of the substrate. Agglomerates are found among which $(55 \pm 5)\,\%$ of the molecules show the same alignment to the substrate as the monomers. In contrast to previous studies of DAF on Ag(111), it is concluded that on Ag(100) the occupation of preferred adsorption sites is energetically favored over H-bond formation. This effect is attributed to the comparably high substrate corrugation.
The periodicity of DAF adsorption sites corresponds to the surface lattice constant of

Ag(100). The tip induced cleavage product of DAF is observed as surface bound carbene. It is exclusively recorded aligned to the closed packed rows of the substrate and in monomer configuration.

In contrast to the carbene species on Ag(111), the carbene on Ag(100) is imaged as centrosymmetric double-dumbbell with a central depression. The depression is attributed to the metal bond. This may indicate a change of the bond angle dependent on the substrate and provides an outlook on comparative follow up studies for targeted laser-induced studies of DAF cleavage on Ag(100).

Neighboring carbenes exhibit no reactivity among themselves. DAF dimers of non-uniform alignment are observed on one distinct sample region. The origin of the different adsorption structures cannot clearly be identified. DAF adsorption on top of a local Xe layer is a conceivable interpretation as well as the occurrence of technical sample adulterations. Additional protrusions recorded on top of Xe islands are regarded as evidence for DAF adsorption on the Xe layer but require further examination in future experiments.

The coadsorption of DAF to Xe leads to a broader scattering of the rotational orientation of Xe domains on terraces next to steps. This is attributed to a larger mobility window of Xe compared to DAF down to low temperates. Both species are cooled down after the annealing which is associated to DAF deposition at $T_{\mathrm{dep}} = 53\,\mathrm{K}$. It is concluded that Xe nucleates during the cooling process at DAF molecules, which immobilize first.

Atomic resolution images reveal that the Xe lattice orientation fits to openings in the course of the contact line to the unaffectedly mainly orthogonally arranged DAF molecules within agglomerates. These openings among DAF molecules seem to serve as nucleation pockets. Their shapes and orientations differ depending on the exact molecular arrangement, which explains the stronger scattering orientation distribution of the Xe domains.

Thus, the apparent larger temperature window of mobility of Xe than of DAF at low temperatures poses new challenges for future studies in order to realize carbene decoupling by a Xe layer. Furthermore, a tremendous impact of measurement interferences becomes apparent in terms of Xe displacement, which pose major difficulties in the investigation of this system.

A stronger fixation of the Xe layer to the metal substrate represents a future objective in Xe mobility reduction. A stronger immobilized layer may enhance the on top deposition of coadsorbates as well as reduce the amount of scan induced displacements. Weiss et al. [49] report of a vast scatter mobility restriction of Xe adsorbed at 4 K on Ni(110) compared to Pt(111).

Possibly, the choice of a substrate with higher corrugation, commensurability, and stronger binding ability to Xe can increase the layer stability up to suitable temperatures. On top protrusions, giving evidence of DAF adsorption on the Xe layer, are explicitly recorded on islands pinned by DAF. Therefore, a targeted Xe anchoring may be accomplished by minor deposition of preadsorbates (DAF) even before Xe deposition. Another objective in order to increase Xe layer stability is to increase the coverage to a continuous monolayer.

Further examination of the additional protrusions on top of the Xe layer require optimized experimental conditions in order to counter image perturbations caused by the high mobility of Xe. It is recommendable to conduct a separate experiment for DAF deposition on Ag(100), allowing a comparison to the adsorption properties of DAF and its cleavage product on Ag(111). This may further support the comprehension of the origin of the regionally separated monomers and dimers. For controlled carbene generation, systematic DAF cleavage should be further induced by laser irradiation.
Then, after careful optimization of the tunneling parameters, it might be possible to apply the gained knowledge to a system with both Xe and DAF. With optimized tunneling parameters and further insight in the behavior of DAF the required number of repetitions for statistical evaluation and validation might be achievable, finally revealing the origin of the on-top protrusions.

Declaration of authorship

I, Inga Christina Langguth, matriculation number 108013210384, born on 1993/11/27, hereby declare that the thesis submitted is my own unaided work. All direct or indirect sources used are acknowledged as references.

Bochum, August 5, 2019

Acknowledgements

Ich möchte mich hiermit ganz herzlich bei all denjenigen bedanken, die auf unterschiedlichen Wegen zur Realisierung dieser Arbeit beigetragen haben. Insbesondere möchte ich daher Frau Prof. Dr. Karina Morgenstern für das Vertrauen zur Unterstützung meiner Projekte auch bis ins Ausland danken sowie für die Zeit als wissenschaftliche Hilfskraft am Lehrstuhl, die meine Studienzeit maßgeblich und sehr positiv geprägt hat. Marvin Quack und Christina Pentzek danke ich für die umfangreiche Einführung in den praktischen Teil der Messungen sowie die große Einsatzbereitschaft für praktische Hilfestellungen. Ich danke Kastur Meyer auf der Heide für das Teilen seiner Expertise im Bereich der Xenon-Deposition und Karsten Lucht für die Möglichkeit zur Weiterführung der spannenden Carben-Thematik und damit verbundenen umfangreichen Diskussionen. Vielen Dank an Iris Trosien für die Herstellung des DAF.

Leonie, Lucie und Ines Plaga sowie Heinrich Haller möchte ich für das Einnehmen der Familienrolle danken, die eine klare Grundvoraussetzung für das Bestreiten eines Chemiestudiums war und mir vieles erst ermöglicht hat. Ebenso möchte ich Werner Döring für die fortwährende Begleitung und Unterstützung während des gesamten Studiums danken. Zuguterletzt ein herzliches Dankeschön an Gottfried Herold. Es freut mich, dass Sie sich ebenfalls für diese Thematik interessieren.

References

[1] McNaught, A. D., Wilkinson, A., and Chalk, S. J., “IUPAC. Compendium of Chemical Terminology”, (Blackwell Scientific Publications, 1997).

[2] Dorta, R., Stevens, E. D., Hoff, C. D., and Nolan, S. P., Journal of the American Chemical Society **125**, 10490 - 10491 (2003).

[3] Izquierdo, J., Hutson, G. E., Cohen, D. T., and Scheidt, K. A., Angewandte Chemie International Edition **51**, 11686 - 11698 (2012).

[4] Costa, P., Trosien, I., Fernandez-Oliva, M., Sanchez-Garcia, E., and Sander, W., Angewandte Chemie International Edition **54**, 2656 - 2660 (2015).

[5] Lucht, K., Über die Abbildung von Solvat-Solvens Wechselwirkungen zwischen funktionalisierten organischen Molekülen und Wasser auf molekularer Ebene, Dissertation, Ruhr-Universität Bochum, (2018).

[6] Jose, B. and Prathapan, S., Journal of Chemical Research **2000**, 478 - 478 (2000).

[7] Dyblenko, T., Chtchemelinine, A., Reiter, R., Chowdhury, R. Q., Enaya, A., Afifi, H., Fournier, R., Mladenova, G., Lever, A. B. P., and Lee-Ruff, E., Photochemistry and Photobiology **90**, 470 - 475 (2014).

[8] Binnig, G., Rohrer, H., Gerber, C., and Weibel, E., Phys. Rev. Lett. **49**, 57 - 61 (1982).

[9] Binnig, G., Rohrer, H., Gerber, C., and Weibel, E., Applied Physics Letters **40**, 178 - 180 (1982).

[10] Binnig, G. and Rohrer, H., Rev. Mod. Phys. **59**, 615 - 625 (1987).

[11] Repp, J., Meyer, G., Stojković, S. M., Gourdon, A., and Joachim, C., Phys. Rev. Lett. **94**, 026803 (2005).

[12] Villagomez, C. J., Zambelli, T., Gauthier, S., Gourdon, A., Barthes, C., Stojkovic, S., and Joachim, C., Chemical Physics Letters **450**, 107 - 111 (2007).

[13] Safiei, A., Henzl, J., and Morgenstern, K., Phys. Rev. Lett. **104**, 216102 (2010).

[14] Morgenstern, K., Lorente, N., and Rieder, K.-H., physica status solidi (b) **250**, 1671 - 1751 (2013).

[15] Gunia, M., Spektroskopische Untersuchungen an Diazoverbindungen und Carbenen auf Metalloberflächen , Dissertation, Ruhr-Universität Bochum, (2003).

[16] Olah, G. A., Prakash, G. S., Liang, G., Westerman, P. W., Kunde, K., Chandrasekhar, J., and Schleyer, P. V., Journal of the American Chemical Society **102**, 4485 - 4492 (1980).

[17] Huang, L., Chey, S. J., and Weaver, J. H., Phys. Rev. Lett. **80**, 4095 - 4098 (1998).

[18] Suh, I.-K., Ohta, H., and Waseda, Y., Journal of Materials Science **23**, 757 - 760 (1988).

[19] Jephcoat, A. P., Mao, H. K., Finger, L. W., Cox, D. E., Hemley, R. J., and Zha, C. S., Phys. Rev. Lett. **59**, 2670 - 2673 (1987).

[20] Sears, D. R. and Klug, H. P., The Journal of Chemical Physics **37**, 3002 - 3006 (1962).

[21] Chesters, M. A., Hussain, M., and Pritchard, J., Surface Science **35**, 161 - 171 (1973).

[22] Igarashi, S., Tosaka, A., Hirayama, T., and Arakawa, I., Langmuir **19**, 4627 - 4632 (2003).

[23] Cohen, P. I., Unguris, J., and Webb, M. B., Surface Science **58**, 429 - 456 (1976).

[24] Diehl, R. D., Seyller, T., Caragiu, M., Leatherman, G. S., Ferralis, N., Pussi, K., Kaukasoina, P., and Lindroos, M., Journal of Physics: Condensed Matter **16**, 2839 - 2862 (2004).

[25] Diehl, R. D., Seyller, T., Caragiu, M., Leatherman, G. S., Ferralis, N., Pussi, K., Kaukasoina, P., and Lindroos, M., Journal of Physics: Condensed Matter **16**, 2839 - 2862 (2004).

[26] Lucht, K., Charakterisierung von amorphem und kristallinem Eis auf Ag(111) mittels Rastertunnelmikroskopie, Master Thesis, Ruhr-Universität Bochum, (2013).

[27] Gibson, K. D. and Sibener, S. J., The Journal of Chemical Physics **88**, 7893 - 7910 (1988).

[28] Horcas, I., Fernández, R., Gómez-Rodríguez, J. M., Colchero, J., Gómez-Herrero, J., and Baro, A. M., Review of Scientific Instruments **78**, 013705 (2007).

[29] Palmberg, P. W., Surface Science **25**, 598 - 608 (1971).

[30] Chesters, M. and Pritchard, J., Surface Science **28**, 460 - 468 (1971).

[31] Dickey, J. M., Farrell, H. H., and Strongin, M., Surface Science **23**, 448 - 452 (1970).

[32] Leatherman, G., Diehl, R., Karimi, M., and Vidali, G., Physical Review B **56**, 6970 (1997).

[33] Falconer, K., "Fractal geometry: mathematical foundations and applications", (John Wiley & Sons, 2003).

[34] Schneider, C., Rasband, W., and Eliceiri, K., Nat Methods **7**, 671 - 675 (2012).

[35] Zhang, Y., Li, Q., Chu, W., Wang, C., and Bai, C., Science in China Series A: Mathematics **42**, 965 (1999).

[36] Koslowski, B., Tschetschetkin, A., Maurer, N., Mena-Osteritz, E., Bäuerle, P., and Ziemann, P., Beilstein journal of nanotechnology **2**, 561 - 568 (2011).

[37] Hansen, K. H., Worren, T., Lægsgaard, E., Besenbacher, F., and Stensgaard, I., Surface Science **475**, 96 - 102 (2001).

[38] Horch, S., Zeppenfeld, P., and Comsa, G., Surface Science **331-333**, 908 - 912 (1995).

[39] Eigler, D. M. and Schweizer, E. K., Nature **344**, 524 (1990).

[40] Stroscio, J. A. and Eigler, D., Science **254**, 1319 - 1326 (1991).

[41] Meyer, G., Neu, B., and Rieder, K.-H., Applied Physics A **60**, 343 - 345 (1995).

[42] Bartels, L., Meyer, G., and Rieder, K.-H., Physical Review Letters **79**, 697 (1997).

[43] Avouris, P., Accounts of chemical research **28**, 95 - 102 (1995).

[44] Nyffenegger, R. and Penner, R., Chemical reviews **97**, 1195 - 1230 (1997).

[45] Tseng, A. A. and Li, Z., Journal of nanoscience and nanotechnology **7**, 2582 - 2595 (2007).

[46] Baski, A., Academic Press **3**, 189 - 214 (2002).

[47] Hla, S.-W., Braun, K.-F., and Rieder, K.-H., Phys. Rev. B **67**, 201402 (2003).

[48] Neu, B., Meyer, G., and Rieder, K.-H., Modern Physics Letters B **09**, 963 - 969 (1995).

[49] Weiss, P. S. and Eigler, D. M., Phys. Rev. Lett. **69**, 2240 - 2243 (1992).

[50] Eigler, D., Weiss, P., Schweizer, E., and Lang, N., Physical Review Letters **66**, 1189 (1991).

[51] Zeppenfeld, P., Horch, S., and Comsa, G., Phys. Rev. Lett. **73**, 1259 - 1262 (1994).

[52] Michely, T. and Comsa, G., Surface Science **256**, 217 - 226 (1991).

[53] Schlichting, H. and Menzel, D., Surface Science **272**, 27 - 33 (1992).